COPY

physical dynamics, inc.

PD-B-76-118

CONCEPTUAL DESIGN OF AN AIRBORNE LASER DOPPLER VELOCIMETER SYSTEM FOR STUDYING WIND FIELDS ASSOCIATED WITH SEVERE LOCAL STORMS

by

J. Alex Thomson

Alan R. Davies

Klaus G. P. Sulzmann

May 1976

Final Report on

Contract No. NAS8-31724

Submitted by

Physical Dynamics, Inc.

Berkeley, California

(NASA-CR-149933) CONCEPTUAL DESIGN OF AN AIRBORNE LASER DOPPLER VELOCIMETER SYSTEM FOR STUDYING WIND FIELDS ASSOCIATED WITH SEVERE LOCAL STORMS Final Report (Physical Dynamics, Inc., Berkeley, Calif.) 157 p HC G3/47

N76-27787
HC $6.75
Unclas
45994

Abstract

The concept of using an airborne laser doppler velocimeter is evaluated for diagnostics of the wind field associated with an isolated severe thunderstorm.

Two scanning configurations have been identified, one a long-range (out to 10-20 km) roughly horizontal plane mode intended to allow probing of the velocity field around the storm at the higher altitudes (4-10 km). The other is a shorter range (out to 1-3 km) mode in which a vertical or horizontal plane is scanned for velocity (and possibly turbulence), and is intended for diagnostics of the lower altitude region below the storm and in the out-flow region.

The essential conclusion of the study is that aircraft flight velocities are high enough and severe storm lifetimes are long enough that it is possible for a single airborne Doppler system, operating at a range of less than about 20 km, to view the storm area from two or more substantially different aspects before the storm characteristics change appreciably. This permits resolution of the spatial distribution of the velocity vector by a single coaxial system operating in a fly-by mode.

In addition, it is concluded that when either or both peak power rather than mean power and/or peak data handling rate rather than mean rate are limiting factors, the optimum signal-to-noise as well as optimum velocity resolution are to be obtained by using pulse lengths comparable to the overall dimensions of the viewed region and, as well, by operating in a continuous azimuthal scan mode. Range resolution is to be recovered in this mode by post-flight image reconstruction analysis.

TABLE OF CONTENTS

III. Scanning Laser System Concepts

LIST OF FIGURES

List of Figures (Con't)

List of Figures (Con't)

APPENDIX I

APPENDIX II

List of Figures (Con't)

List of Tables

APPENDIX II

CONCEPTUAL DESIGN OF AN AIRBORNE LASER DOPPLER VELOCIMETER SYSTEM FOR STUDYING WIND FIELDS ASSOCIATED WITH SEVERE LOCAL STORMS

I. Introduction

The purpose of this study is to develop design concepts for an airborne laser doppler velocimeter system for sensing the vector wind fields associated with severe local storms. Presently available remote techniques are limited to microwave Doppler radar and give information primarily about regions of substantial radar reflectivity, i.e., essentially, where there is precipitation. The prime potential for a laser system is to regions of weak echo or no echo return for conventional radars. In general, this comprises three spatial volumes: the low level boundary layer below the cloud structure, the internal updraft region (commonly is a weak echo region) and the external velocity field surrounding the storm cloud, particularly in conditions of strong vertical wind shear and/or for rotating storms. Convergence rates and shear or vorticity are of particular interest in the regions external to the cloud, whereas velocity and turbulence levels or mixing rates are relatively more important in the internal regions.

A complete sequence of measurements must be made within the overall lifetime of the storm, typically 30 minutes, with sufficient time resolution to follow changes in the structure of the storm ($\Delta t \sim 2$ to 5 minutes). The coverage area and spatial resolution vary somewhat depending on which part of the storm is being diagnosed. The main body of the storm can be adequately diagnosed with a square coverage area of 10 to 20 km on a side. Spatial resolution of 200 to 500 meters is necessary to resolve the basic storm structure. Better resolution ($\leq$ 100 m) may be required for the more sophisticated measurements where convergence rates and vorticity are the desired quantities. A velocity resolution of the order of 1 m/sec is adequate to specify the internal wind fields and the low altitude gust regions. In the region external to the storm poorer spatial resolution may be permissible (perhaps up to 1 km) but better velocity and velocity gradient sensitivity is required to be able to measure the convergence and vorticity fields. High spatial resolution is also required to discriminate regions of turbulence from non-turbulent but strongly sheared regions.

This report is divided into three sections. Section II (and Appendix II) describe the basic characteristics of severe storms and establish design criteria in terms of space-time-velocity resolution and coverage requirements. In Section III various scanning configurations are discussed and two of these are selected as candidates for further discussion in Sections IV and V.

The unique capability of the aircraft to view the storm area from several different aspect angles before substantial changes in the storm configuration take place allow deduction of the velocity vector as well as permitting substantial improvement in the spatial resolution-velocity resolution tradeoff by post-flight processing. A detailed analysis and simulation of this effect is undertaken in Section IV and design tradeoff factors established relating the manner in which instrumental range resolution and number of views can be exchanged to keep the same final spatial resolution. Finally, in Section V, the results are summarized and specific recommendations made for instrument design.

II. Dimensional Characteristics of Severe Local Storms - Summary

The basic morphology of a typical severe local thunderstorm is shown in Figure 1. Features of particular interest to the designer of a measurement system include the magnitude and scale of the mean and fluctuating wind fields, the time scale for their change and the overall extent of the phenomena. In Appendix II we have attempted to summarize and classify these basic features for a variety of severe storm types. Included are single and super cell thunderstorms, tornadoes and funnel clouds as well as a variety of peripherally related phenomena; dust devils, gravity currents, etc.

We can identify three main geometrically distinct regions associated with a typical storm. First, the main body of the storm, extending from 2 or 3 km altitude up to near the tropopause, is the primary visible object (clouds) and contains the regions strong up and downdrafts. It is generally opaque to optical sensors and laser velocity measurements will be limited to the near surface regions. The second region is close to the ground (up to 3 km) for a mature thunderstorm and is a horizontally extended region of cold air beneath (and ahead) of the main body of the storm. This region results from cold air in the storm sinking and spreading horizontally. Especially near the leading edge of this outflow region, strong gusts may be

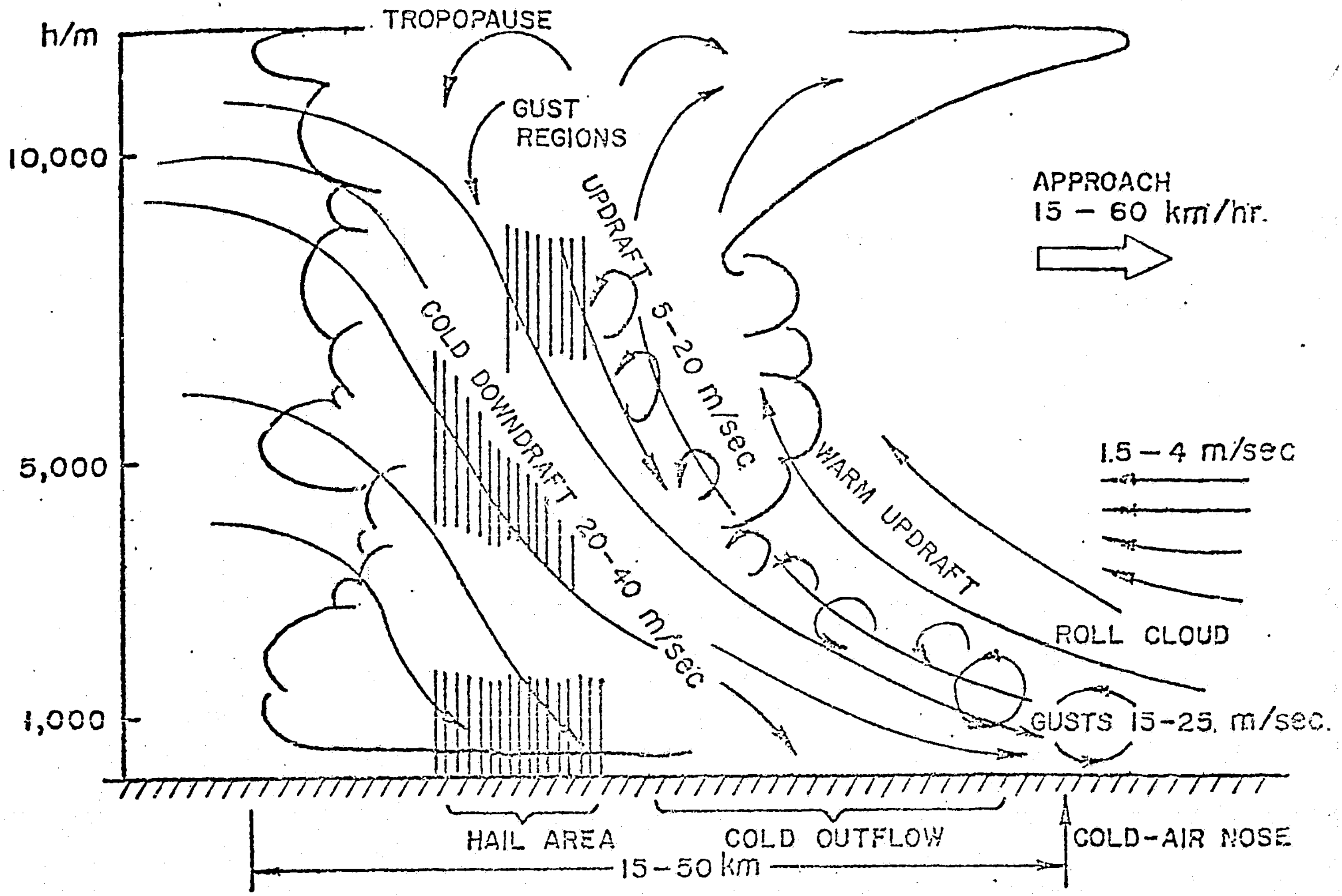

Figure 1(a): Typical Thunderstorm Cell Moving from Left to Right (side view).

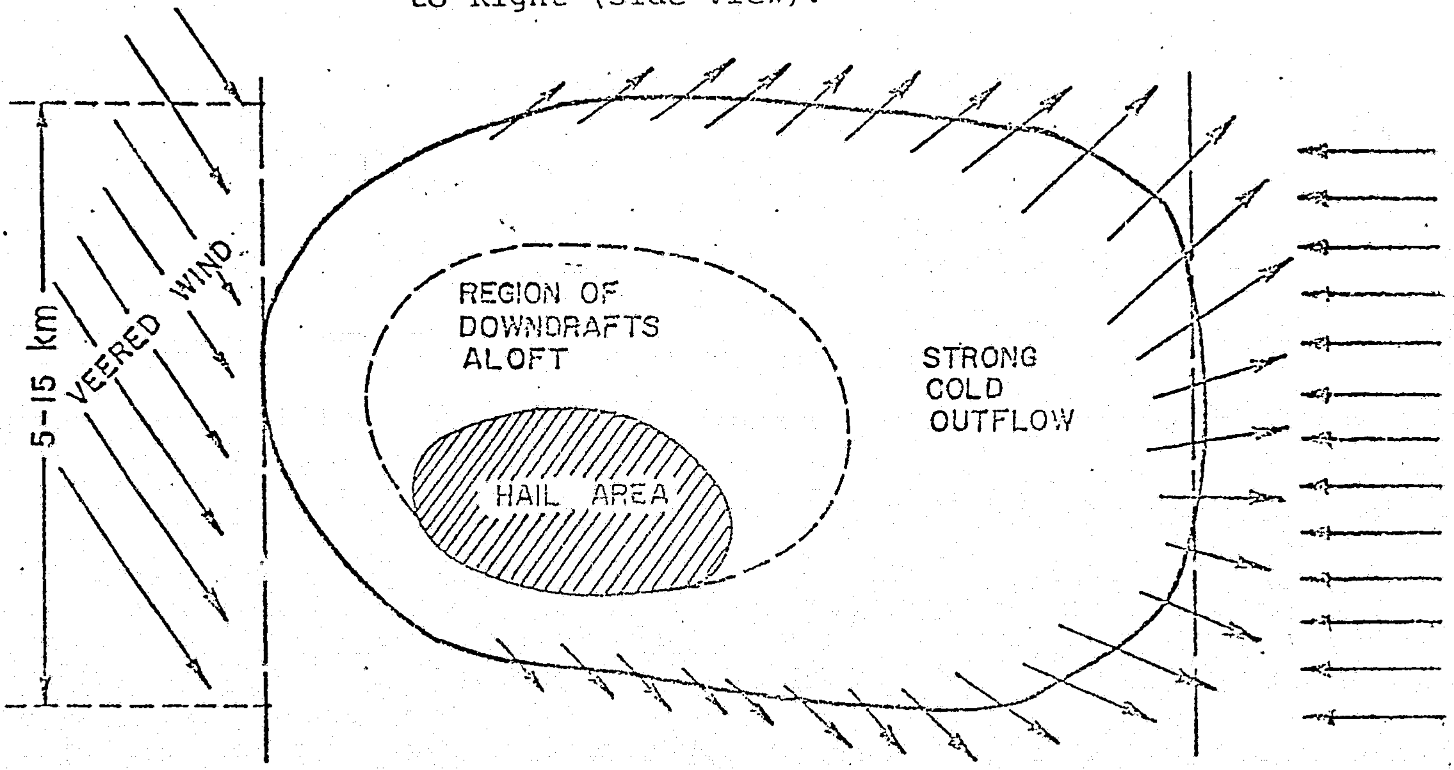

Figure 1(b): Typical Thunderstorm Cell Moving from left to Right (top view near ground).

encountered. The lower portion of this region is typically clear air. Water droplet clouds or dust clouds may be present on occasion and occupy part of this region.

The third region characteristic of the storm is the inflow or outflow region surrounding the body of the storm at altitudes above the low altitude outflow region. The horizontal flow convergence and vertical shear of the wind field in this region describe characteristics of the energy and vorticity input to storm distinct from the vertical convection inputs. These may be particularly important in determining the tornado-producing potential of the storm.

In Figure 2 we have summarized the essential velocity-size characteristics of severe storms. Four essentially different phenomenology regions are identified. First, the storm cell region itself comprises the main body of the updraft/downdraft region and is the primary visible feature of the storm. Because it is generally impenetrable optically, laser diagnostics are confined to measurements of the near surface velocity fields.

Surrounding the storm is the external flow region. For single cell storms this is a generally clear air region of much lower velocity shear than the interior. Velocity measurements in this region look for the general

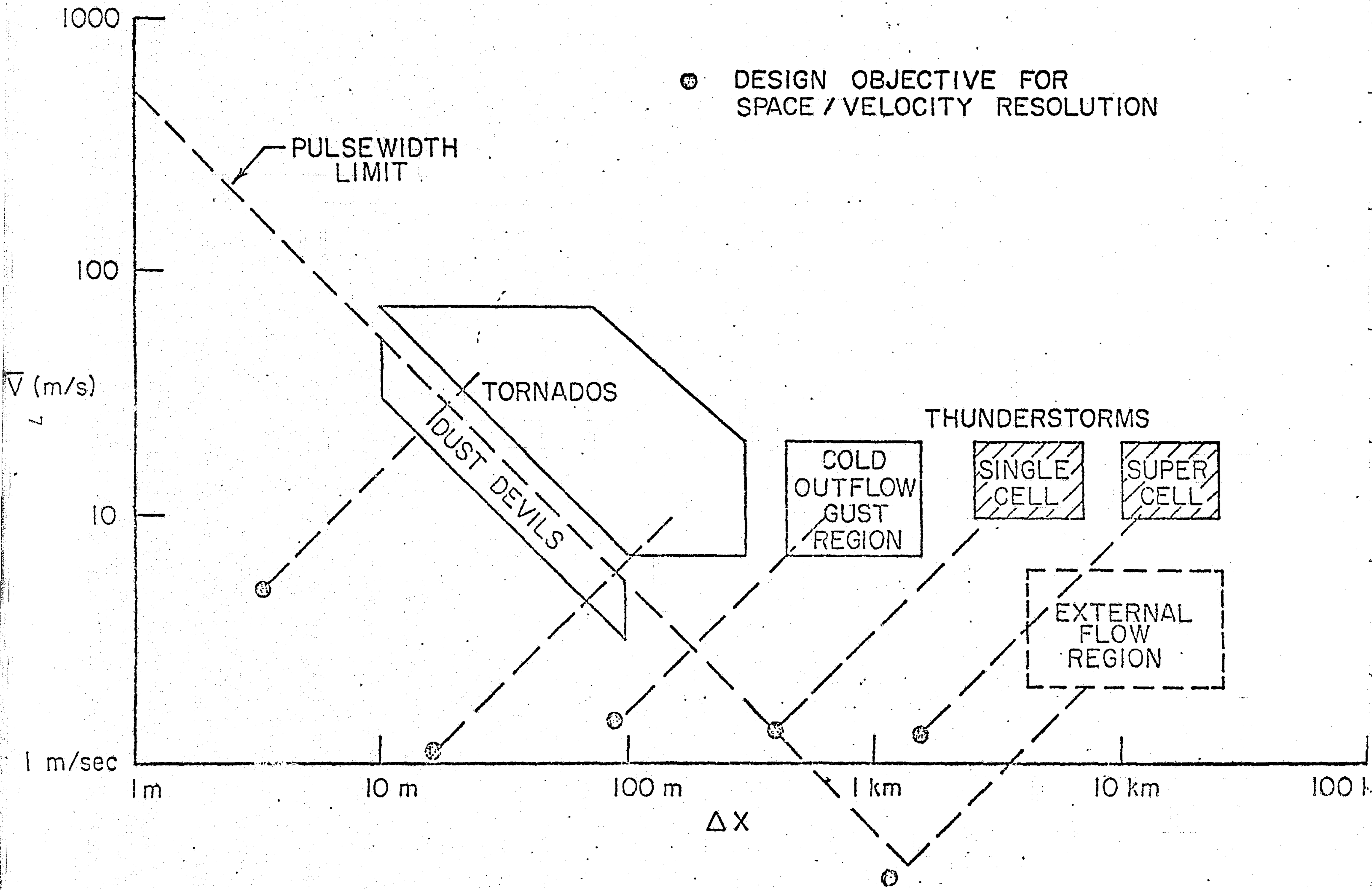

Figure 2. Velocity Size Characteristics for Various Storm Features.

fluid dynamic structure of the storm environment: the vertical shear, the vertical vorticity, and the convergence or divergence of the horizontal velocity. Three altitude intervals are of interest: 0 to 2 km (the cold outflow region), 2 to 8 km (the main vertical extent of the storm) and 8 - 12 km, the region of high altitude outflow in the mature stage.

Coverage dimensions are of the order of twice the storm crossection dimension in the 2 - 8 km interval (i.e. 5 to 10 km) up to several times these values in the low (and high) altitude intervals (i.e. from 10 to 50 km).

The low altitude boundary layer region beneath and around the storm we define as the third distinct measurement region. This is the region of strong cold outflow and may extend horizontally many times the storm cell dimension (10 - 50 km) although the vertical height remains limited ($<$ 1 to 3 km).

The fourth phenomenology region includes the small scale and localized features such as tornadoes, water spouts, and funnel clouds.

In Figure 2 we have also indicated suggested spatial and velocity resolution design goals for these regions. These were established essentially as 10% of the characteristic dimension and characteristic velocity respectively.

For the purpose of defining a laser measurement system we have grouped the various phenomena into the first three general categories just discussed (excluding tornadoes) and their basic characteristics are presented in Table 1. As indicated in this table we have used these characteristics to define two distinct measurement regimes, one appropriate to the low altitude outflow region and the other to the higher altitude region exterior to the central body of the storm. These are essentially the second and third regimes discussed above. The central body of the storm (the first regime) is judged to be too opaque for laser diagnostics except for cloud surface measurements. These latter we include as part of the exterior region. Measurement system candidates are discussed in Section III.

Characteristic Features	Storm Interior I	Low Altitude Outflow Region II	External Region III
Overall Horizontal Scale	3 - 6 km	6 - 30 km	3 - 10 km
Vertical Scale	2 - 10 km	1 - 2 km	2 - 10 km
Spatial Resolution Required	100 - 300 m	100 - 300 m	300 - 600 m
Time Scale (lifetime)	10 - 30 min	10 - 30 min	10 - 30 min
Time Resolution Required	2 - 4 min	2 - 4 min	4 - 8 min
Typical Horizontal Velocity	10 - 20 m/s	5 - 40 m/s	0.5 - 4 m/s
Typical Vertical Velocity	5 - 10 m/s	up to 10 m/s	0.1 - 1 m/s
Useful Measured Quantity	$\overline{\delta u_{\parallel}^2}$, w , u,v	u, v, $\overline{\delta u_{\parallel}^2}$	$\nabla_h \cdot \vec{u}$, $\nabla_h \times \vec{u}$, u,v
Opacity to Optical System	high, opaque except for surface	Partially clear, range limited by atmospheric absorption	Clear for single cell storms, range limited by signal strength.
Laser Measurement Concept	No	Yes	Yes

Table 1. Characteristic Parameters for Three Storm Regions

III. Scanning Laser System Concepts

III.1 Introduction

Two quantities are of basic interest: the wind velocity vector $\vec{u}$ and, in regions of strong gradient, the turbulence levels (and, associated with these, the mixing rates). In general the wind field has three vector components which vary from point to point. A single laser radar system operating in Doppler mode senses only one component and cannot by itself provide a direct general measurement of the instantaneous vector velocity of a wind field which is varying in an essentially random manner in space and time. Fortunately there are a number of good approximations that are often valid that will allow meaningful measurements to be obtained even for a measurement system that cannot measure the general vector field. We group these into three categories: first, those that happen to be valid for the normal physical state of the atmosphere, second, those that depend upon some spatial uniformity of the wind field and, third, those that depend on a temporal uniformity.

The dual Doppler diagnostic technique is an example of the first category. Here two remotely located Doppler radars measure simultaneously two of the three velocity components as a function of position throughout the measurement volume. The fact that wind velocities are always small compared to the sound speed implies that the atmosphere is essentially incompressible and this condition can be used to generate the third velocity component by integration of the continuity equation. The technique does require that the two-component velocity field be measured throughout the spatial volume and that a suitable boundary condition can be established (typically that the vertical velocity vanishes at the ground surface).

In the second category we include the well-known VAD technique (velocity-azimuth display) for measuring vertical wind shear. Here the vertical velocity as well as the horizontal gradients in the wind vector are assumed negligibly small so that measurements of the Doppler component at the same altitude but at different horizontal locations can be combined to yield the horizontal wind vector.

Temporal homogeneity (third category) is used in the 'drift' type correlation measurements to deduce velocity vector components not directly detected by a Doppler system. Here inhomogeneities drifting across the line of sight are detected in some fashion (time correlation between signals from adjacent parallel lines of sight, or time spectral analysis of the response of a broad beam sensor whose aperture can be controlled so as to be selective for certain spatial scales.)

Almost by definition it is not easy to apply these techniques to a localized storm. The strong three dimensional spatial gradients of the overall storm wind field essentially preclude VAD concepts except perhaps on rather short and uninteresting length scales. Drift measurements require statistical homogeneity on a time scale many times the transit time associated with the correlation length scale. This type of technique is potentially applicable to a ground based storm monitoring system in which the optical sensor utilizes its very high azimuthal resolution to sense small scale inhomogeneities at each point in space. It requires a very high data aquisition load in its simplest version since the spatial scale sensed must be much smaller than the basic resolution required. This requirement can possibly be mitigated by appropriate spatial filtering techniques which allow the density of small scale irregularities to be sensed without having to record their structure point by point. Even in this latter case, however, it is necessary to record and analyze the data on a time scale very much shorter than the basic time scale associated with the overall wind field.

It appears probable that this type of measurement will be most useful in an environment where properties are uniform in at least one direction so that the data recording rate is reduced to a reasonable level.

Airborne systems have difficulty in utilizing any type of measurement technique, such as this one, that require extended periods of time for each velocity measurement. The dwell time or time period allowed for the total volume measurement varies in proportion to the range in a fly-by mode and can only be made long at the expense of reduced signal strength and loss of spatial resolution associated with long range operation.

The prime advantage of aircraft operation (in addition to the crucial one of mobility) is that, since the observation platform moves at a speed very much higher than the mean speed of the storm, a single aircraft can obtain near simultaneous views of the storm area from several different aspect angles. Thus it potentially can simulate the capability of several remote fixed location platforms. As will be shown, this capability can be converted into a capability for high spatial resolution in three dimensions.

III.2 Design Criteria

We consider that the following problem areas must be addressed in the design analysis:

1. Ability to measure a) velocity vector
   and/or b) turbulence level
2. Spatial Resolution
3. Temporal Resolution and Dwell Times
4. Propagation losses and signal-to-noise

5. Data Handling and Processing

Each of these areas will be discussed in the following sections.

III.2.1. Measurement of the Vector Wind Field and Turbulence Field

A Doppler measurement at a single space-time point can be made in a time a few multiples of the reciprocal of the Doppler shift ($\Delta t \sim \lambda/2V \sim \frac{5.0}{v(\mathrm{m/sec})}$ μsec) whereas a drift or correlation measurement takes a time a few times L/v where L is the inhomogeneity scale. The minimum inhomogeneity scale resolvable is determined by diffraction $L \sim \lambda R/D$. At a range of 1 km with a 0.3 meter aperture, $L = 0.03$ meters and $\Delta t \sim 0.03/v(\mathrm{m/sec})$ seconds. Thus for an area measurement with 30 x 30 grid the net time required (for $V = 1$ m/sec) is 27 seconds for the drift system as compared to 0.004 seconds with the Doppler system. Since times of the order of 100 times these values are required for a single measurement (to get 10% accuracy), Doppler techniques appear to be the only method applicable for a system which must obtain volume data in two or more dimensions in a serial processing mode.

In a parallel processing mode (each space point monitored continuously and simultaneously) drift type measurements are conceptually applicable. Although we feel that it may be possible to develop such a concept in the future, no such scheme has presently been applied in a scanning mode. In any case, because of the small scale of the inhomogeneities sensed, the scene registration problems for an airborne system would be formidable in addition to the fact that observation times are necessarily short. For the present study it was felt that such a concept would require a substantial effort even to be defined, and detailed evaluation could not be undertaken within the present study framework. Thus it was concluded that only a Doppler technique offers promise for early implementation.

In the pure Doppler mode it is mandatory to have at least two different aspect angles to obtain the velocity vector. At a range of 10 km and a flight velocity of 150 meters per second the viewing aspect angle changes at the rate of about one radian per minute. Since the major characteristics of the wind field change over substantially longer time periods (see Table 1), a single airborne moving platform can, in principle, be used to measure the velocity vector. The error in one component due to the fact that the components are measured at different times is of order

$\Delta V \sim \frac{V_s}{V_a} \frac{R}{T_s}$ where V_s is a typical storm velocity, V_a the aircraft speed, R the range and T_s the characteristic time associated with the development of the storm wind field. For R = 10 km, T_s = 10 minutes, and V_a = 150 m/sec,

$$\frac{\Delta V}{V_s} \approx 0.1$$

Of course, this error can be substantially further reduced by averaging one set of measurements with a second set taken during an immediately following fly-by on the same course but in the reverse direction. Here the errors to first order have opposite signs.

The turbulence field can be measured in two ways: a) from the width of the Doppler spectrum and b) from the fine scale structure of the measured vector velocity field. In principle both can be measured as scalar quantities from only one aspect angle. However, the width measurement will be contaminated with spectral broadening effects associated with wind shear. The spectral broadening (in velocity units) due to wind shear along the line of sight is

$$\Delta V_{\parallel} = \frac{\partial V_{\parallel}}{\partial S} \Delta S$$

where ΔS is the longitudinal resolution. In a simple shear layer, the rms width due to turbulence is

$$\Delta V_{rms} = \frac{\partial V}{\partial y} \ell$$

where ℓ is the largest eddy scale length (mixing length) contributing to the random turbulent field and $\partial V/\partial y$ is the velocity shear driving the turbulence. Mixing lengths of the order of 10 or 20% of the thickness of the shear layer are expected. Since the requirements of the measurement system necessitate a spatial resolution ΔS also of this order or smaller (i.e. $\Delta S \lesssim 0.1\ L \approx \ell$) the spectral broadening due to turbulence and that due to longtitudinal gradients in the mean wind field may be comparable. Thus we conclude that the spectral width of the Doppler return is not likely to be an unambiguous estimator of turbulence level and it will be necessary to measure directly the local fine scale irregular structure of the velocity field. However since the small scale turbulence is expected to be isotropic, it would be possible to obtain an adequate measurement of the turbulence level from a single viewing aspect. The requirements on range resolution for such a measurement are higher than for the mean velocity field by perhaps a factor of 3 to 6 (i.e. where a range resolution of 300 meters may be adequate for the mean velocity field, 50 to 100 meters would be required for a turbulence measurement.

III.2.2. Spatial Resolution

The required spatial resolutions for various regions are defined in Table 1. Essentially a resolution at least as good as 100 meters is specified for the closer ranges and, at all ranges, for turbulence measurements. At longer ranges the requirements are weaker for the mean velocity field (300 meters).

The CW laser systems obtain range resolution by focusing, and the effective length of the resolved volume increases strongly with range (see Figure 3). Reference to this figure shows that, at least without additional processing, CW systems fail to achieve adequate resolution at ranges greater than about a kilometer (assuming a useful effective aperture of 0.3 meter diameter). The actual useful aperture achievable depends, in addition to any mechanical or cost constraints, on both the range and the ambient turbulence level along the line of sight. Limiting effective apertures can be determined from Figure 4.

Pulsed systems achieve range resolution directly by the finite pulse duration. Associated with the finite pulse length is a finite frequency bandwidth and velocity uncertainty. In Figure 5 we show how the available range resolution-velocity resolution product compares to the

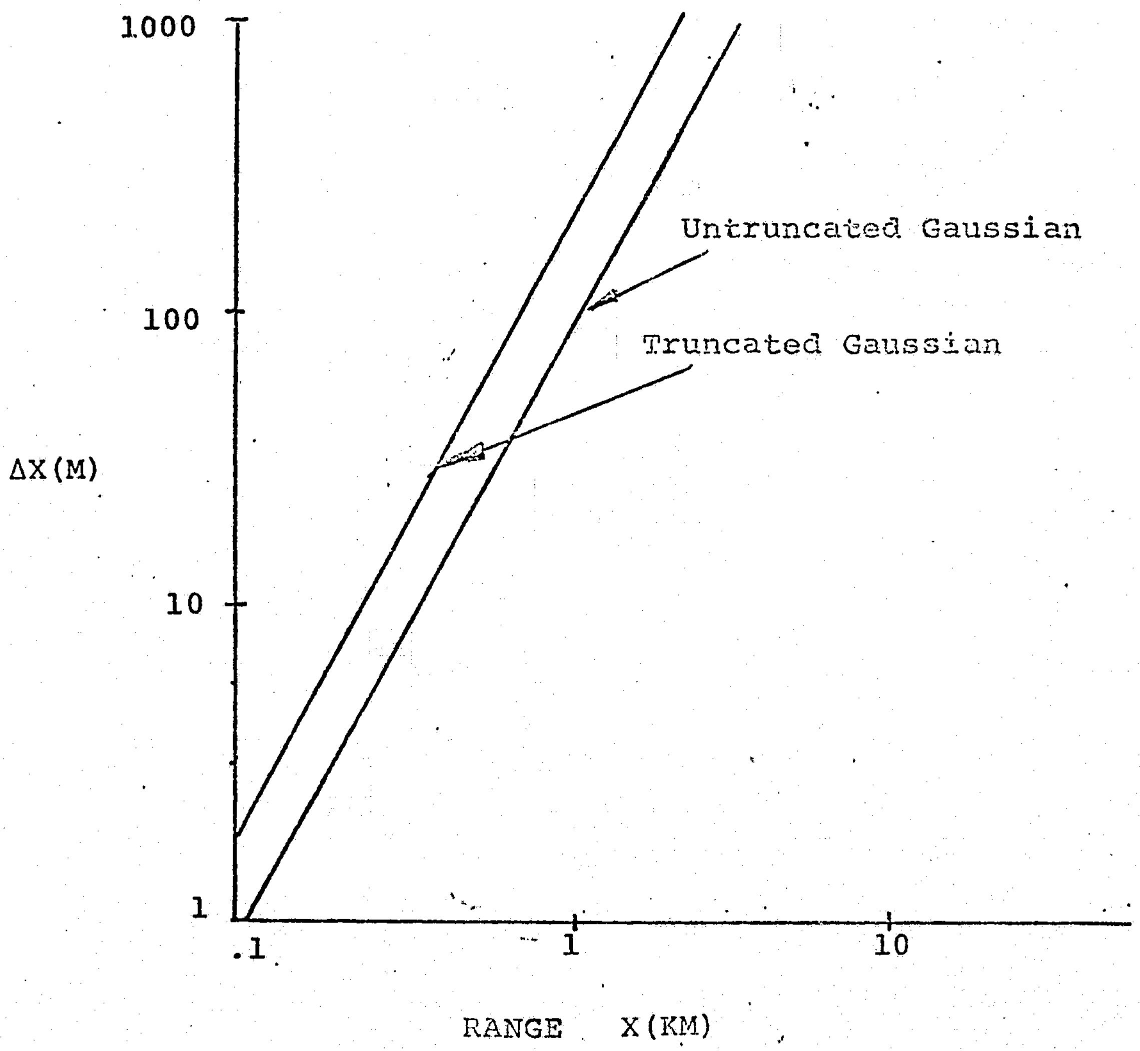

Figure 3 Range resolution obtained by focusing. Coaxial system. (30 cm aperture)

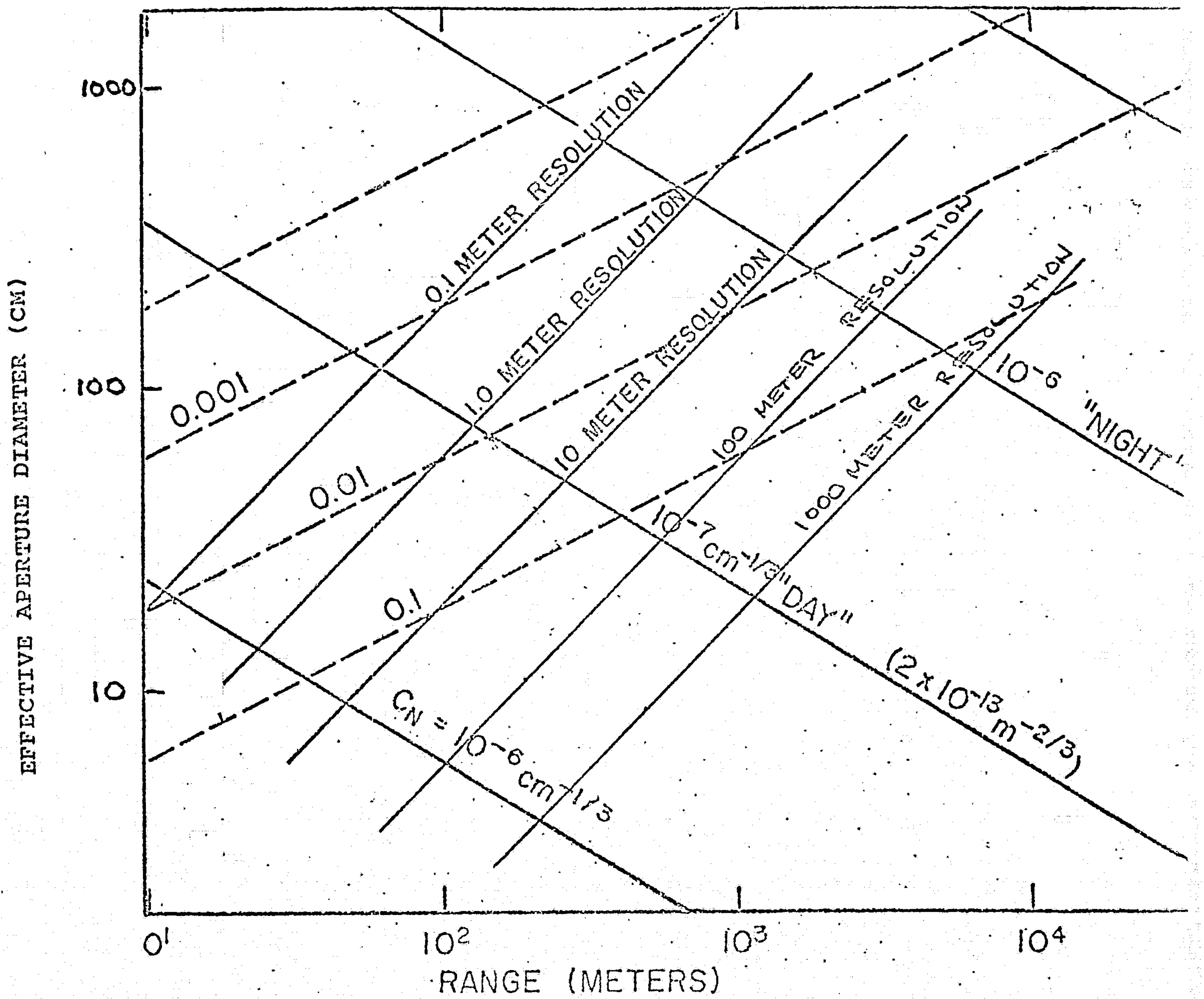

Figure 4

Dependence of Effective Aperture on Range and Turbulence Level

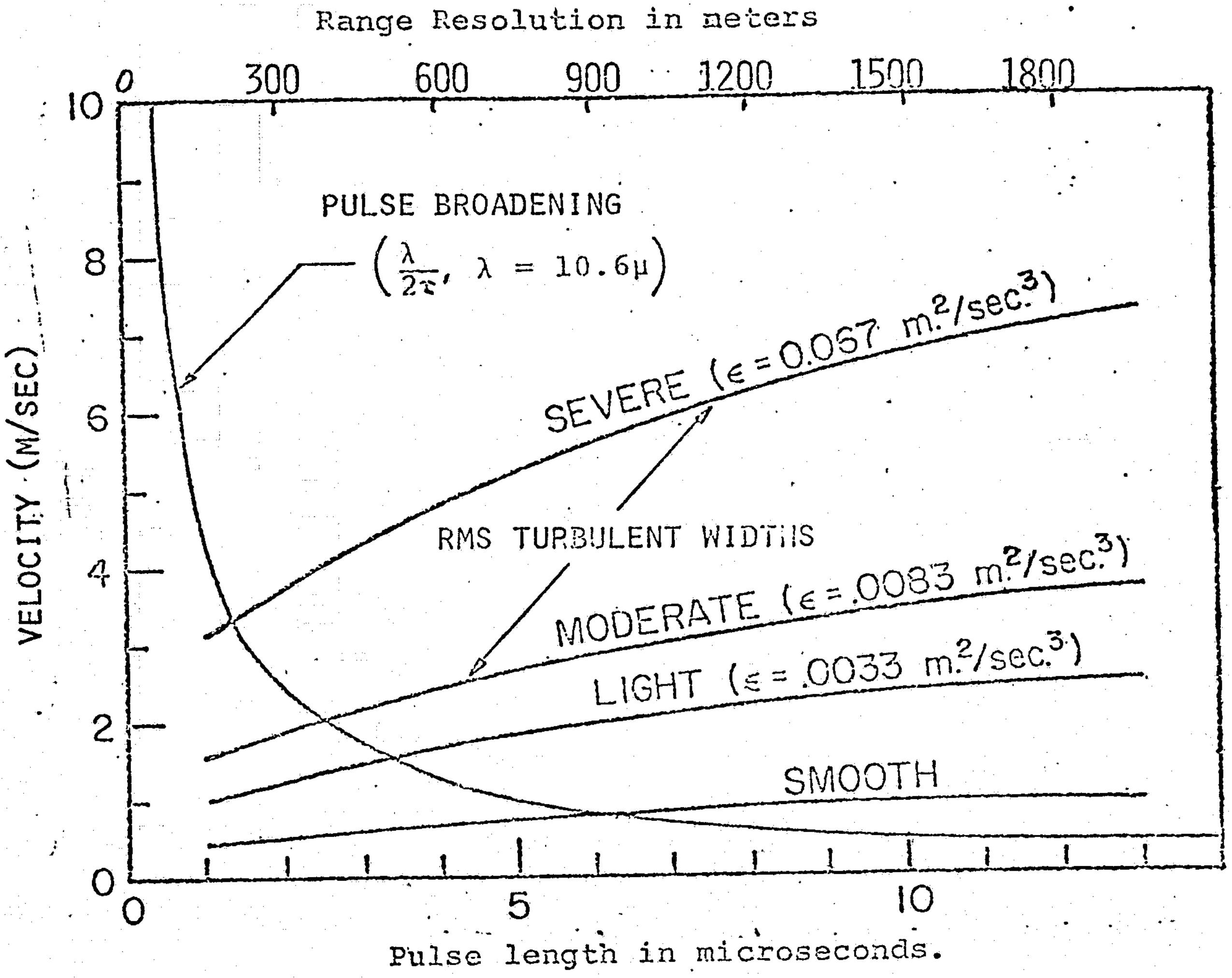

Figure 5 Equivalent Doppler velocity widths.

typical turbulence levels (see also Fig. 2). It is apparent that coarse velocity information about the larger scale features can be obtained directly with a pulsed system without additional processing. Improved range resolution will be needed however for accurate measurements.

There are two methods that potentially can be implemented to improve this resolution: range processing and aspect processing.

Range Processing

When the signal-to-noise ratio is high, data taken as a function of range can be processed so as to improve the effective range resolution. The improvement achievable depends on both shape of the range response function and the signal-to-noise ratio. The optimal method for accomplishing the improvement in the presence of white noise is called matched filtering and is described in detail in Appendix I. Substantial improvement at high values of SNR can be achieved only with range response functions that have sharp cutoffs. Fuzzy or spreadout functions permit only modest improvements.

In Appendix I it is shown that the optimally processed range resolution ΔX^* may be approximately estimated at high SNR from the expression

$$|g(k = 2/\Delta X^*)/g(k = 0)| = 1/\sqrt{\mathrm{SNR}_{\mathrm{power}}}$$

where SNR is the (power) signal-to-noise level and g(k) is the spatial Fourier transform of the range response function. For a CW focused system the range response function at ranges where good depth of field can be achieved is

$$f(x) = \frac{\text{constant}}{(X-X_c)^2 + (\Delta X_{cw}/2)^2}$$

Here ΔX_{cw} is the range resolution between 3 db points. In Fourier space this resolution function is

$$g(k) = \text{constant} \cdot \exp(-|k|\Delta X_{cw}/2)$$

Thus, the 'best' processed range resolution is estimated as

$$\Delta X^* = \Delta X_{cw} \big/ \ln(SNR_{voltage}) = \frac{\Delta X_{cw}}{2} \Big/ \ln(SNR_{power})$$

Power signal-to-noise ratios between 20 and 30 db permit range resolution improvements by a factor between 2 and 4.

The same type of argument applied to the improvement of the range resolution of pulsed systems. For a perfectly square pulse

$$f(X) = 1 \quad \text{for } |X| \le \frac{\Delta X}{2}{}_{pulse}$$

$$= 0 \quad \text{otherwise} \quad .$$

The Fourier transform is

$$g(k) = \frac{\sin((\pi/4)\,k\,\Delta X_{\text{pulse}})}{(\pi/4)\,k\,\Delta X_{\text{pulse}}} .$$

The optimal range resolution is obtained from the relation

$$\left(\frac{\sin(1.57\,\Delta X_{\text{pulse}}/\Delta X^*)}{1.57\,\Delta X_{\text{pulse}}/\Delta X^*}\right)^2 = \frac{1}{\text{SNR}_{\text{power}}}$$

i.e.

$$\Delta X^* \approx \Delta X_{\text{pulse}}\sqrt{2/\text{SNR}_{\text{power}}}$$

(The factor of 2 came from averaging the sin squared term.

This expression indicates that substantial improvement is possible for such pulses at high signal-to-noise ratios (factors of 10 to 20 for $\text{SNR}_{\text{power}}$ values of 20 to 30 db). However, the result at high SNR is totally dependent on the sharpness of the leading and trailing edges of the pulse. Finite rise and fall times of the actual pulse will strongly suppress this dependence.

In summary it appears that, at high signal-to-noise ratios, significant improvement in range resolution can be achieved by processing the data in range for both CW and pulsed systems. The improvement anticipated at an SNR = 30 db varies between a factor of about 3 to an upper limit of about 20. The higher values require very precise shaping of the range resolution function and are undoubtedly difficult and expensive to achieve in practice. Nevertheless some improvement can always be achieved if the SNR is high enough and such processing should be included in the design. The optimal (as well as the most direct) technique is that of matched filtering.

Aspect Processing

All optical systems basically exhibit very high lateral or angular resolution but much poorer range resolution. However, by making observations at various aspects the range resolution may be vastly improved. A hologram is an interesting example of this process. Whereas a normal photograph of a scene essentially records only the lateral variation and has virtually no range resolving power, a hologram is able to record the scene as it appears at a variety of aspect angles. This record can be viewed subsequently using various methods to extract range information (triangulation, parallax, depth of focus).

A technique which might be described as a type of incoherent holography is currently finding extensive application in a variety of fields, particularly in medicine in whole body X-ray scanning. Basically a number of one-dimensional projections of a two-dimensional, (crosssectional) transparent object are formed at a number of equally spaced aspect angles. These projections are then combined together by a computer to yield a picture of the two-dimensional structure. In medical applications the number of views required for useful reconstruction ranges from 20 to 200. An example of such reconstruction applied to X-ray imaging of the cross-section of a human body is shown in Figure 6. A similar technique is potentially applicable to the reconstruction of velocity fields when the scanning measurements can be made at a number of viewing aspect angles. A detailed analysis of the mathematics of this procedure is presented in Section IV. For the discussion here, however, it is sufficient to note that significant image improvement is possible with as few as four views although a much larger number may be desireable to recover the fine scale detail.

An attempt was made in the analysis of this method in Section IV to establish a quantitative relation between the spatial resolution improvement and the number of aspect views. Because a matched filter analysis was used the result depends explicitly on the signal-to-noise ratio. The computer simulation technique used and discussed in Section IV yielded satisfactory results for a scalar field (such as the turbulence level) and roughly exhibited an inverse relationship between number of views and processed spatial resolution (i.e. $\Delta X^* \approx \Delta X_o/N_v$, where ΔX_o is the single sensor resolution

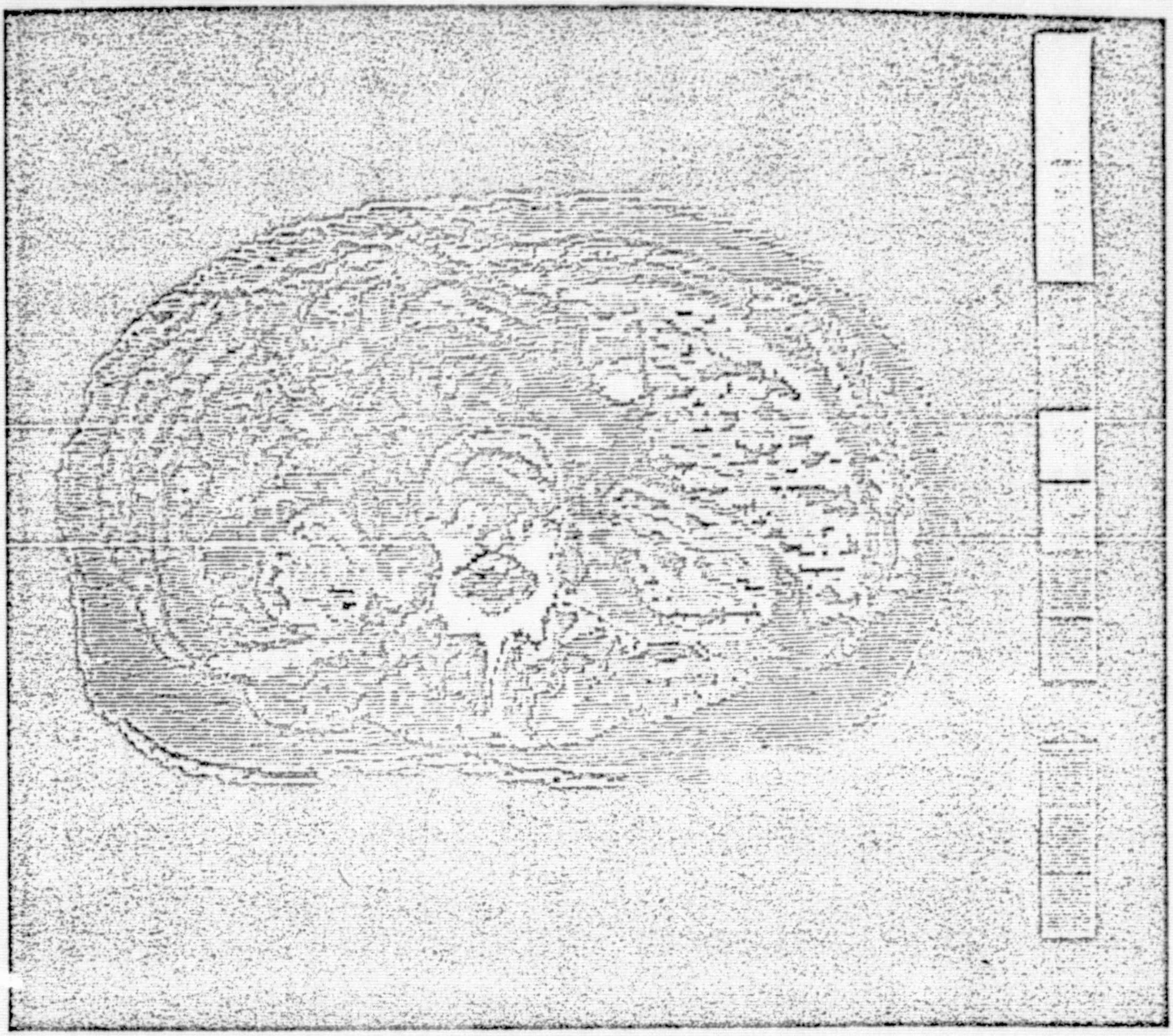

CROSS SECTION OF ABDOMEN of a living human subject appears in this X-ray picture made by reconstruction from projections. This section is seen from the same perspective as the one on the cover of this issue: from above the subject's head. The vertical bar at the right is the key to the X-ray density of the tissues in the section; white represents the greatest density, black the least density and the colors the densities in between. The white areas below the center of the section are the spinal column. The large light-colored area running from upper right to lower right is the liver. The light area near the upper end of the liver is the gall bladder, which here contains an X-ray opaque dye for diagnostic purposes. The two roundish areas to the left and right of the spinal column are the kidneys. The small dark areas extending from the top around to the lower left are sections through loops of intestine. This picture, like the one on the cover, was made by the Delta Scanner built by Ohio-Nuclear in the course of a study by Ralph J. Alfidi, M.D., of the Cleveland Clinic Foundation. The picture required 180 separate X-ray projections, made at one-degree intervals around a half-circle. Total dose of X rays was approximately the same as that needed to make a single conventional X-ray plate.

Figure 6. X-ray imaging of the cross-section of a human body. (Scientific American, Oct. 1975, Page 57)

and N_v the number of views). The corresponding dependence for the vector wind field was less simple, and it is felt that further analysis will be required to establish an optimum processing technique. The tradeoff between number of views and spatial resolution (derived from the present simulations) is shown in Figures 24 to 26.

III.2.3 Temporal Resolution and Dwell Times

The dwell time available to examine each resolution volume may be estimated as follows. The time available to examine one resolution volume is the total observation time divided by the number of resolution elements. To scan a single plane this is

$$\Delta t = \frac{R}{V_a N_x N_y}$$

where R is the mean range and V_a the flight velocity. For the two scanning modes discussed in Section III.3 (50 resolution elements in range, 25 in azimuth) this dwell time is 100 milliseconds (for a maximum range of 20 km) or 25 milliseconds (maximum range of 5 km). The maximum permissible integration time is this time increment divided by the number of views. However, when post-flight processing is carried out an incoherent integration is automatically performed (albeit with some losses). Thus, the signal-to-noise ratio can be estimated based on the above net dwell times if some account is taken of the processing losses (such as scene registration losses). The maximum signal-to-noise is to be obtained with the highest mean output power together with the lowest prf consistent with the data taking mode. However, these values of the prf are generally quite small. For a 100 meter resolution and 150 m/s flight velocity, the minimum time between pulses should be 0.7/N_v sec. where N_v is the number of views. For N_v = 10 the optimum prf is only 14/sec corresponding to a pulse energy of 300 millijoules at a mean power of 5 watts. At lower pulse energies and higher prf's some losses are to be expected due to the fact that incoherent rather than coherent integration takes place.

III.2.4. Propagation Losses and Signal-to-Noise

Atmospheric losses due to molecular absorption and turbulence are significant at low altitudes at the range of interest even under good seeing conditions, and limit the usable ranges.

For a pulsed system operating in a collimated mode (focused at infinity), the SNR is

$$S/N = \eta \frac{J}{32\ hc/\lambda} \frac{D^2\ \overline{n\sigma}\ c\tau}{R^2 + \left(\frac{\pi D^2}{4\lambda}\right)^2} L(R) \quad .$$

where

J = net output energy in the observation time

D = aperture diameter

τ = pulse time

$\overline{n\sigma}$ = particle density times scattering cross-section

η = (mean value at range R)

L = detection efficiency

R = range

L = propagation loss factor

The factor L is the product of the molecular loss L_{mol} and the turbulent loss L_{turb}.

At ranges less than the Rayleigh distance ($R_* = \pi D^2/4\lambda$), the signal-to-noise ratio varies with range only as a result of the loss factor L;

$$S/N \simeq \eta \frac{J}{2\pi^2 h\nu} \frac{\overline{n\sigma}\,\lambda^2\, c\tau}{D^2} L(R) \qquad \text{for } R < R_* \quad .$$

For a 30 cm effective aperture diameter and $\lambda = 10.6\mu$, this expression is appropriate for ranges less than about 7 km.

Within the range limits, some benefit can be obtained by focusing on the range interval of primary interest. For pulse lengths less than the focal depth $\left(\frac{c\tau}{2} < 4R^2\lambda/D^2\right)$, the signal-to-noise from the region near the focal point is

$$S/N = \eta \frac{J\lambda}{32hc} \frac{D^2\ \overline{n\sigma}\ c\tau}{R^2} L(R)$$

and exhibits an inverse square dependence on range in addition to the range dependence through the propagation loss factor.

Molecular absorption results principally from CO_2 lines and the wings of the nearby water vapor bands. Signal-to-noise estimates for a range resolution equal to 10% of the actual range are given in Figure 7. The signal-to-noise ratio is given in terms of its value per unit energy in a resolution volume. For coherent integration of successive pulses the actual signal-to-noise for many pulses can be obtained directly by multiplying the ordinate by the total laser energy allocated to a given resolution volume. Only pulses separated in time by less than the laser line correlation time (reciprocal of the laser bandwidth) can be integrated coherently, however. For the more usual case where the time between pulses is greater than the correlation time, incoherent integration must be used and the effective signal-to-noise will be reduced from the coherent value given in Figure 7 by the factor $N^{-1/2}$ where N is the number of incoherent pulses integrated.

The signal-to-noise levels given in Figure 7 are based on a back scattering coefficient of 10^{-3} km^{-1} at sea level (which is appropriate for clear air) and an overall instrument-detector efficiency of 0.6%. Actual SNR values may vary upwards substantially from this value in hazy conditions and/or for improved sensors. Nevertheless the basic conclusion that must be drawn from this figure is that molecular absorption will limit the maximum workable range to some value less than about 5 km at sea level.

Under conditions of strong surface heating, low altitude turbulence will further degrade the returns. The signal-to-noise ratio in this case is conveniently

Figure 7. - Signal-to-Noise per Joule vs. Range (Atmospheric attenuation included).

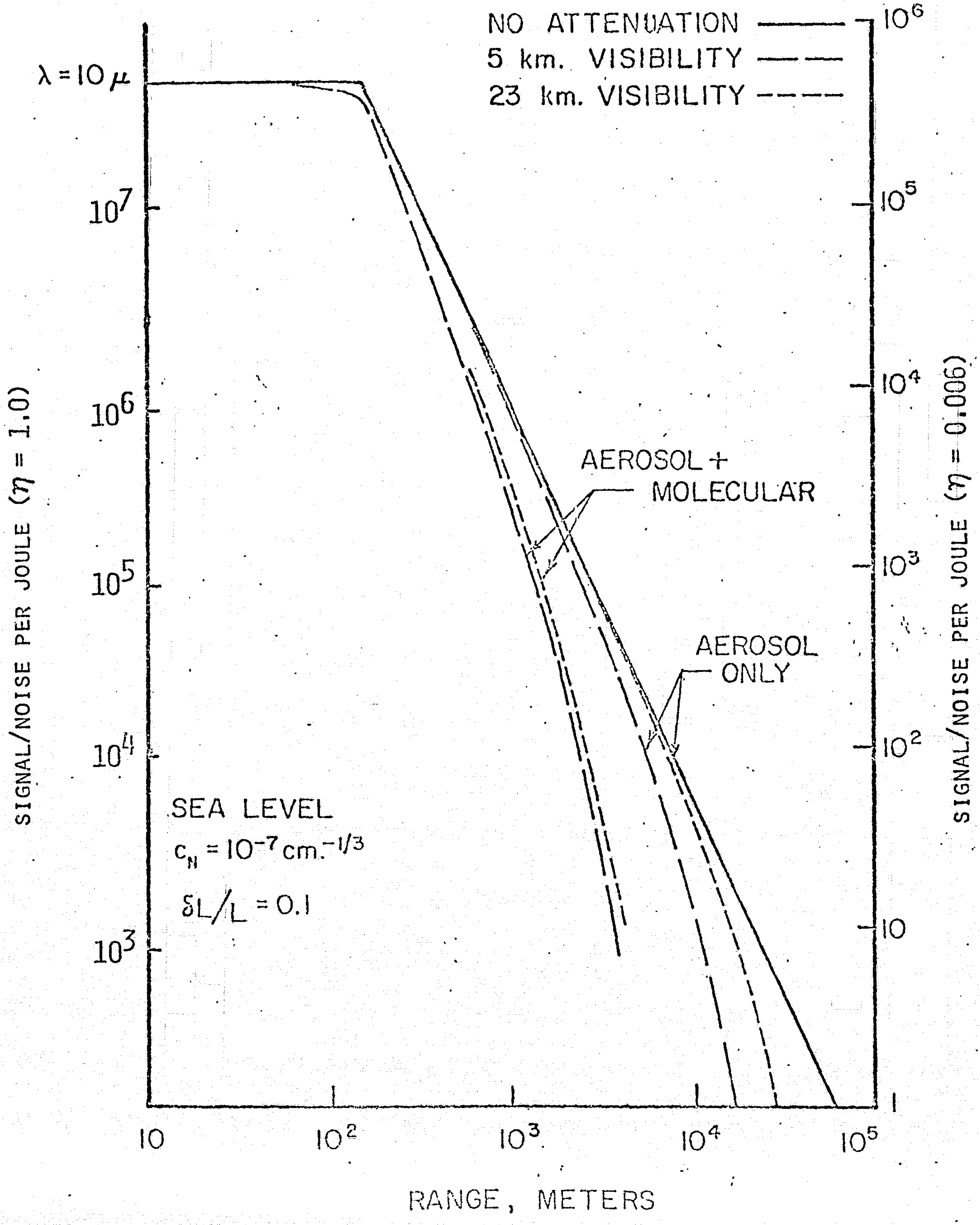

expressed in terms of an effective coherent aperture radius r_a. When r_a is small compared to the actual aperture D, the optimum signal-to-noise (that obtained when the beam is focused on the range point of interest) is given by

$$S/N = \frac{\eta}{8} \frac{J}{H\nu} \overline{n\sigma} \frac{r_a^2}{R^2} c\tau \quad .$$

The value of r_a is given by the expression

$$r_a = 0.0581 \lambda^{6/5} \Big/ \left(C_N^{6/5} R^{3/5} \right)$$

where R is the range and C_N the refractive index structure coefficient due to the turbulence.

III.2.5. Data Handling and Processing

The average rate at which data is to be acquired and recorded is relatively low. For example, for a planar scan with a 25 x 50 mesh, allowing 2 minutes for the total observation and 10 separate scans or views of the observation plane the mean data taking/recording rate is about 200 values/second. With a pulsed system, however, the peak data rates are very much higher: the Doppler spectrum must be analyzed within one pulse time (= $2\Delta X/C$). For a range resolution of 300 meters this is 2.1 μsec (0.7 μsec for 100 m resolution). This corresponds to a peak data handling rate of between 5×10^5 and 1.5×10^6 <u>output</u> values/sec. Two techniques are possible to reduce this peak load: either buffering the input or using longer pulses but maintaining the high spatial resolution by post-flight processing of the multiview data. In the design a tradeoff analysis should be performed to compare the advantages of lower peak data handling rates to the increased complexity of the multiview process. It should be also noted that longer pulses also improve the coherent to incoherent integration time ratio.

When the signal-to-noise ratio per pulse is significantly greater than unity, optimum use of the available power requires that the signal energy be spread as uniformly as possible over the individual measurement degrees of freedom. For a two-dimensional field of the type we are considering here, it is convenient to examine the way information is collected in the (spatial) Fourier transform plane rather than physical plane. Here the coordinates are the wavenumbers k_x and k_y and the measured data consists of the amplitudes of the Fourier modes within a circle about the origin having a radius $k = \pi/\Delta x$, where Δx is the limiting spatial resolution. The spacing between different or independent modes is $\Delta k = 2\pi/L$ where L is the overall linear dimension of the scene. The objective of the measurement is to sample and measure each of these modes.

As is discussed in some detail in Section IV the effect of low range resolution in the laser spatial response function is to permit sampling of the k_x, k_y space by a single sensor only in the neighborhood of a line emanating from the origin ($k_x = k_y = 0$) and perpendicular to the direction of view. Full sampling requires superposition of several views each at a different aspect angle (see Figure 11).

In the presence of white (instrumental) noise optimum measurement strategy requires that the signal energy should be spread more of less uniformly throughout the sampling area in $\vec{k}$ space. Emphasis on particular directions at the expense of others is to be avoided. For a multiview system with a finite number of views (say 10 views) it is, therefore, better to have 10 different aspect views each having a signal-to-noise ratio of 5 (= 7 db) than only 5 views each with twice the signal strength S/N = 10 (10 db). This effect is shown for example, in the simulations of Figures 16 and 17. Here the same total signal energy was assumed constant but distributed over a varying number of view angles. The one-view data in Figures 16 and 17 were calculated as the average of 8 identical measurements each with an independent noise realization; similarly the 8-view data were obtained with a different noise realization for each view. It is clear from this figure that substantially more information is obtained when the measurements are distributed uniformly in aspect angle.

Thus the basic design strategy should be the following: After the desired spatial resolution (Δx) and coverage dimension (L) are established, the merits of working with single sensors having poorer range resolution (than Δx) are to be assessed with respect to data rates, peak powers, signal energy, velocity resolution, etc. If a substantially improved performance can be obtained in this manner, a multiview concept should be generated. The minimum angular spacing between independent views is $\Delta\theta = 0.5\, k_{min}/k_{max} = \Delta x/L$.

If this spacing cannot be achieved then there will be a penalty in terms of the ultimate resolution achievable. The consequences of such incomplete sampling and attempts to ameliorate it are discussed at some length in Section IV.

No attempt will be made here to discuss various specific data handling problems, such as storage, indexing, real time vs. post-flight processing, scene registration, scene overlap losses. Required data recording rates for particular scanning concepts are discussed in the following section.

Curves relating how the number of separate views required must be increased as the pulse time is lengthened in order to maintain a given resolution are given in Figures 24, 25 and 26. These curves were derived by analyzing the results of a limited number of computer simulations of the multiview analysis. The results depend on signal-to-noise levels as well as on the filtering processes assumed. The processing techniques used were not optimum and, for actual design purposes, it would be desirable to investigate improved methods, particularly for the vector wind field analyses.

III. 3 Selected Design Concepts

III. 3.1 Introduction

Based on the preceding analysis we have selected three separate design concepts for more detailed discussion. Two of these, a short range and a long range single plane scanning configurations are recommended for more detailed design. The third configuration requires viewing of several parallel planes simultaneously and consequently has a much higher mean data rate and more stringent requirements for signal-to-noise levels and scene registration requirements. It is suggested that detailed consideration of this last configuration be premised on the successful demonstration of the simpler modes.

III.3.2 A Short Range System

This concept is intended to be appropriate for examining the low altitude outflow region or for probing the vertical velocity profile within 1 to 3 km of the aircraft. In the simplest form the laser line of sight makes one of a set of fixed angles with respect to the aircraft flight axis. A coverage area whose dimension is smaller than the mean range is contemplated. As the aircraft completes a sweep of the beam through the coverage area, the beam aspect angle is reset so as to obtain an additional sweep. This procedure is repeated for as many different aspect angles as geometry permits. The configurations for a two-aspect and a three-aspect angle observation are indicated in Figure 7a. In practice for coverage of an area whose lateral dimension is comparable to the range, only two or three aspect angles are possible. In Table 2a we give characteristic values for the parameters for such a configuration.

Better area coverage and more aspect angles can be obtained at the expense of a more complicated optical-mechanical system in a continuous scanning mode (see Figure 7b). Here a full scan in azimuth is made in the time it takes the aircraft to move one resolution length. The mean data rate is much higher than in the fixed position line of sight (LOS) configurations. Suggested parameters for such a scanning configuration are given in Table 2b. Advantages of the continuous scan multiview mode versus the 2 or 3 position LOS mode include better area coverage and smaller scene overlap losses, lower peak power requirements, lower peak data handling levels, lower incoherent integration losses, good velocity resolution. Disadvantages are the more complex scanning requirements, the requirements for additional post-processing of the data, and the (possible) requirements for greater data storage. If no in-

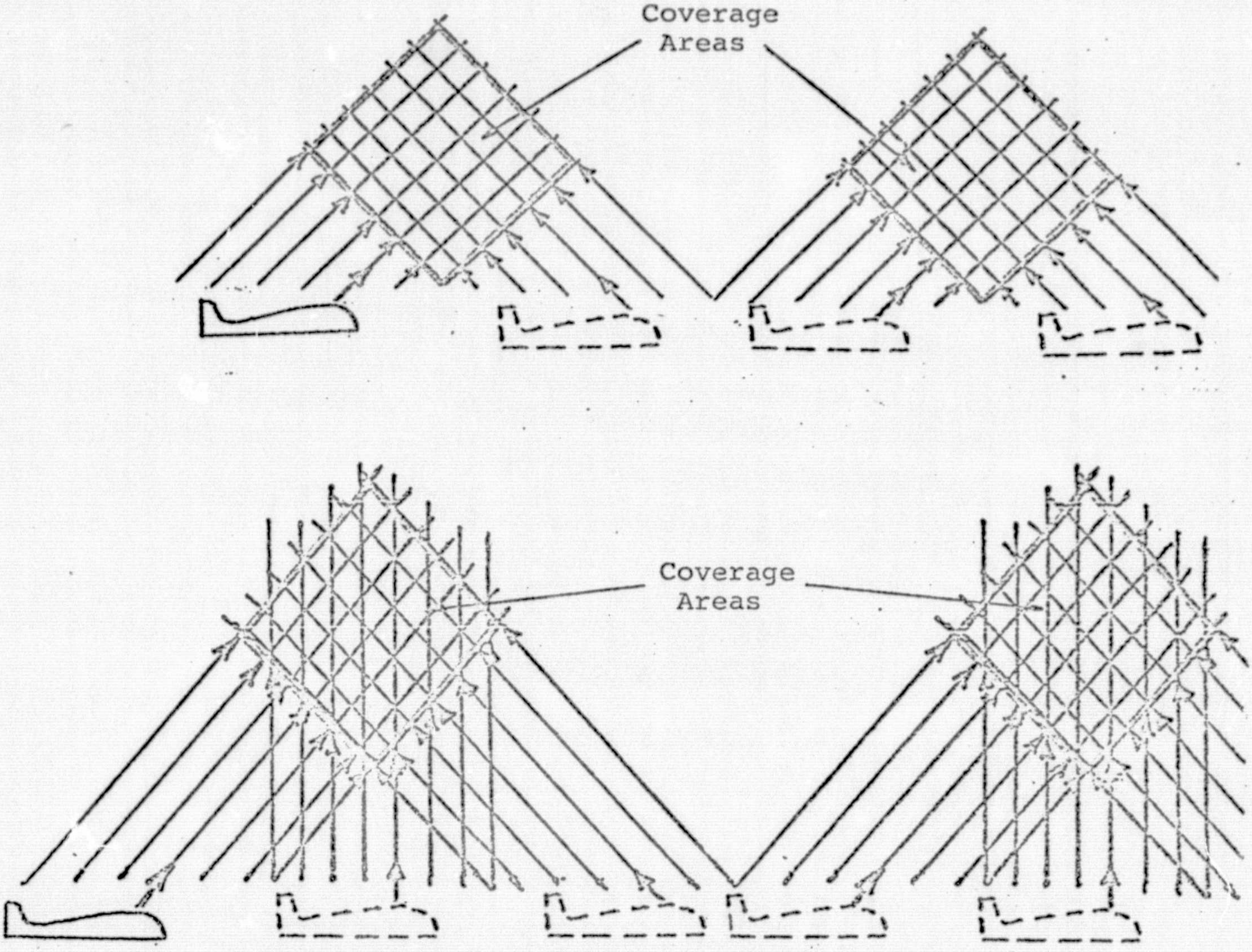

Fig. 7a. A two-view and a three-view fixed position LOS configuration.

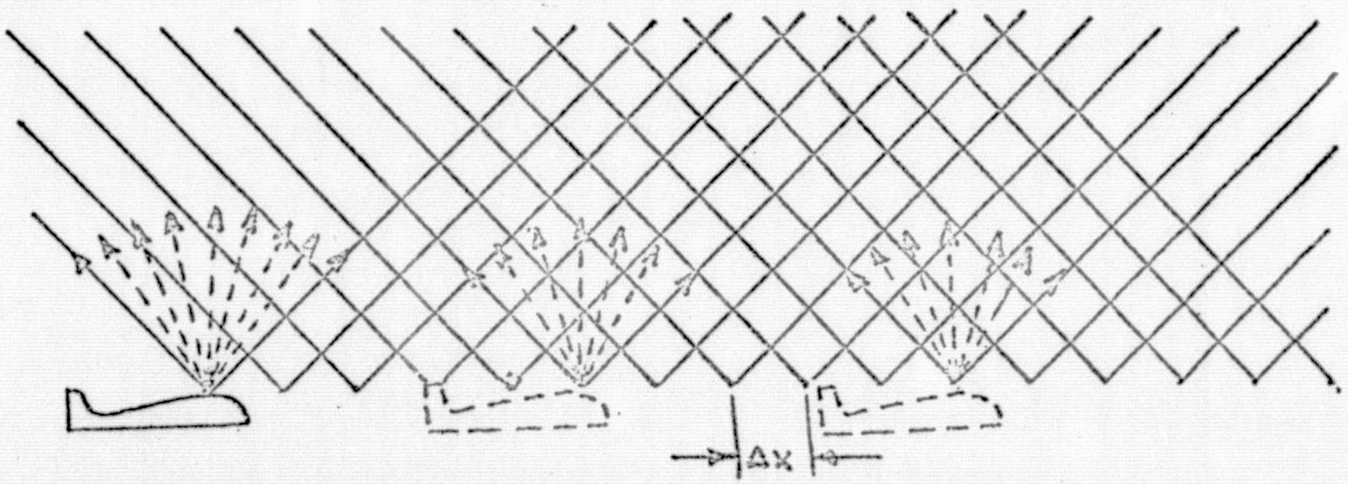

Fig. 7b. A continuous multiview scanning configuration.

Table 3a. Suggested Characteristics for a Two-and Three-View Fixed Position LOS Side Looking System.

	Short Range System		Long Range System	
	2 View	3 View	2 View	3 View
Assumed Flight Velocity (m/s)	150 m/s		300 m/s	
Range to Center of Coverage Area (km)	3 km		15 km	
Diameter of Coverage Area	3 km	2.5 km	15 km	12.5 km
Spatial Resolution (meters)	125x125 m	125x125 m	300x300 m	300x300m
Useful Grid	25x25	20x20	50x50	42x42
Total Observation Time	47 sec	63 sec	2 min	2.7 min
Mean Time Between Azimuthal Points	0.9 sec	1.0 sec	1.2 sec	1.3 sec
Mean Data Recording Rate (value/sec)	28 sec^{-1}	20 sec^{-1}	42 sec^{-1}	32 sec^{-1}
Number of Data Points per Frame	1320	1260	5040	5180
View Angles	$60^{\circ},120^{\circ}$	$45^{\circ},90^{\circ},135^{\circ}$	$60^{\circ},120^{\circ}$	$45^{\circ},90^{\circ},135^{\circ}$
Mean Ranges in Each View (km)	3.5,3.5 km	4.2,3.0,4.2 km	17.5,17.5 km	21,15,21 km
Observation Time in Each View	23,23 sec	23,17,23 sec	1.0,1.0 min	1.0,0.7,1.0 min
Peak Input Data Rate (value/sec)	1.15×10^{6} sec^{-1}		5×10^{5} sec^{-1}	
Pulse Length (time)	125 m (0.4 μsec)		300 m (1 μsec)	
Pulse Energy/average watt of Laser Power	0.9j/watt		1.2j/watt	
Optimum prf (sec^{-1})	1.1 sec^{-1}		0.8 sec^{-1}	
Peak Pulse Power at Optimum prf/watt of Laser Power	2000 KW/watt		1200 KW/watt	
Incoherent Integration loss at prf=100sec^{-1}	-10 db		-10 db	
at prf=1000sec^{-1}	-15 db		-15 db	

Table 3b. Suggested Characteristics for a Multiview Continuous Scanning Side Looking System

	Short Range System	Long Range System
Assumed Flight Velocity (m/s)	150 m/s	300 m/s
Mean Range (km)	3 km	15 km
Spatial Resolution (meter)	125x125 m	300x300 m
Frame Dimensions	3x3 km	15x15 km
Useful Grid	25x25	50x50
Number of Azimuth Points per Scan	25	50
Useful Number of Range Points (½ total number)	25	50
Number of Views per Frame	30	50
Time Between Scans (sec)	.85 sec	1.0 sec
Mean Data Recording Rate (values/sec)	700 sec^{-1}	2500 sec^{-1}
Number of Data Points per frame	18750	125000
Total Time for One Frame	22 sec	50 sec
Peak Input Data Rate	$5x10^4$	10^4
Pulse Length (time)	3 km (10 μsec)	15 km (50 μsec)
Pulse Energy/Average Watt of Laser Power (joules)	0.03j	0.02j
Energy Per Processed Data Point	0.9j	1.0j
Optimum prf (sec^{-1})	30 sec^{-1}	50 sec^{-1}
Peak Pulse Power at Optimum prf/watt of Laser Power	3 KW/watt	0.4 KW/watt
Incoherent Integration loss at a prf=100 sec^{-1}	-2.6 db.	-1.5 db
=1000 sec^{-1}	-7.6 db	-6.5 db

flight processing is carried out, the data recording rate for the continuous scanning multiview mode is 10 to 20 times greater than for the simpler two view fixed LOS mode and can lead to a substantial data load. However, the post-processing techniques are relatively straightforward and it should be possible to carry out in-situ and perhaps even real-time processing. Basically 1 or 2 two-dimensional Fast Fourier transforms are required for each azimuthal scan (i.e. roughly each second) with a 32 x 32 or 64 x 64 grid. When this can be done the signal data recording requirements are relatively low (less than 100 values/second).

III.3.3 A Long Range System

The simplest version of the long range system has the same parameter structure as the short range system. Here, however, the range resolution requirements are less stringent. Candidate sets of system parameters are given in Table 2. Except for the differences in values of the system parameters, the configurations are the same as for the short range systems.

III.3.4 Multiple Plane Scanning System

In Figure 8 we show the basic configuration for a long range scanning system. This system would have the capability of scanning and recording the Doppler signal from set of horizontal planes stacked in the vertical direction. Multiple looks at different aspect angles yield the components of the velocity in each scan plane.

The already developed techniques for processing this two-component data to yield the third velocity component can be implemented. Here the vertical velocity is calculated from the incompressibility relation

$$\frac{\partial w}{\partial z} = -\frac{\partial u}{\partial x} - \frac{\partial v}{\partial y}$$

The vertical velocity w may then be evaluated from

$$w(x,y,z) = -\int_0^z \left(\frac{\partial u}{\partial x} + \frac{\partial v}{\partial y}\right) dz$$

In practice a more complicated equation must be solved to account for the fact that the individual scanned planes are not all parallel (see Fig. 8). Here the measured in-plane components are related to the actual horizontal (u,v) and vertical (w) velocities according to

$$S_u = u\cos\theta + w\sin\theta$$

$$S_v = v\cos\theta + w\sin\theta$$

The vertical velocity is then to be evaluated from

$$\frac{\partial w}{\partial z} = \tan\theta\left(\frac{\partial w}{\partial x} + \frac{\partial w}{\partial y}\right) - \frac{1}{\cos\theta}\left(\frac{\partial S_u}{\partial x} + \frac{\partial S_v}{\partial y}\right)$$

No detailed analysis of this mode has been undertaken during this study. The mean data rates are an order of magnitude greater than for the single plane system and the requirements for measurement accuracy are greater (in order to measure the gradients). It was felt that a more definitive analysis of the simpler modes should precede analysis of this much more sophisticated technique (see Table 3 for two possible configurations).

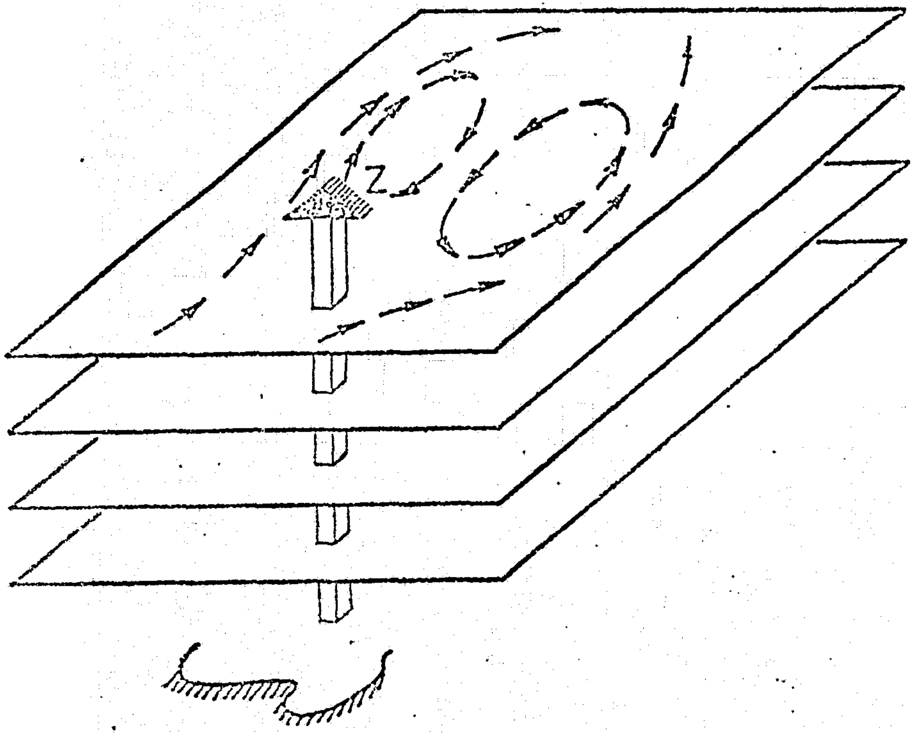

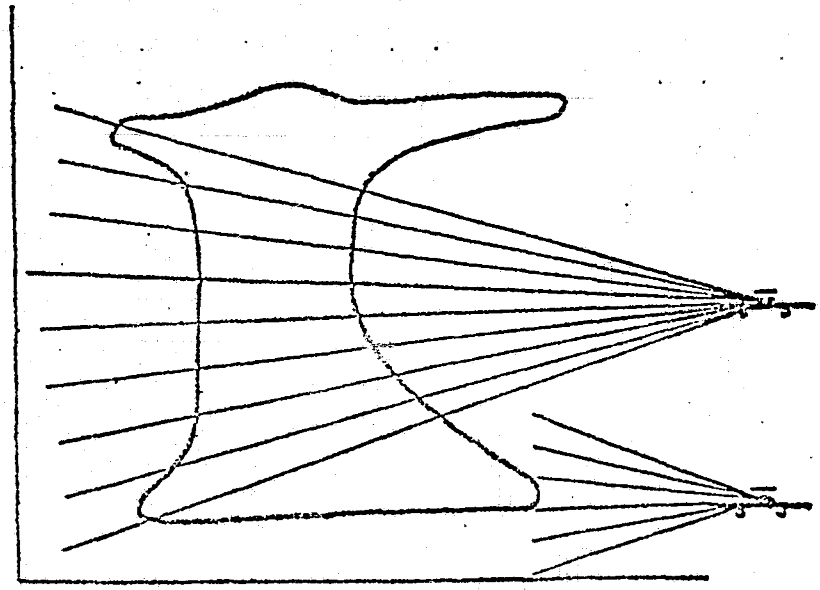

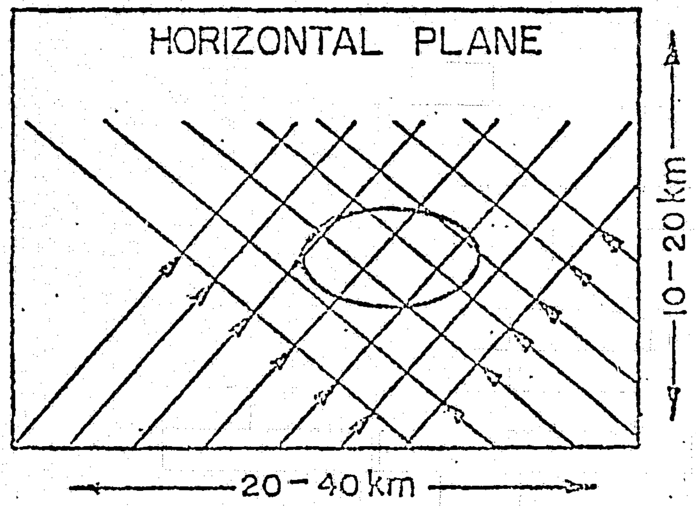

Figure 8 Scanning Configuration for a Long Range Multiple Plane Scanning System

Table 5. Possible Parameters for a Multiple Plane Scanning System

Assumed aircraft speed	300 m/sec	100 m/s
Mean range to coverage area	18 km	18 km
Diameter of coverage area	15 km	15 km
Total observation time (2 views)	2 minutes	6 min.
(3 views)	3 minutes	9 min.
Spatial resolution	300 m x 300 m	
Mean data input rate for 10 planes	420/sec	140 sec
Time between Vertical Scans	1 sec	3 sec.

IV. MULTIVIEW SYSTEM ANALYSIS

IV.1 Introduction

We treat the LDV scanning system as an imaging sensor which views a scene from various directions. The scene is characterized by a reflected or scattered light intensity distribution $\sigma(\vec{x})$ and its Doppler spectrum. The imaging system records a degraded representation of this scene (an N-dimensional scene in general is recorded as an N-dimensional pattern with finite spatial resolution). The finite resolution or spatial gain of the recording system is described by a response function $G(\vec{x}'-\vec{x},\hat{r})$. In this section we will develop a mathematical analysis of this type of sensing system and the processing required to reconstruct the original scene.

The recording system depends on two parameters: the viewing direction defined by the unit vector $\hat{r}$ and the displacement $(\vec{x}'-\vec{x})$ of a spatial point $\vec{x}'$ from the point $\vec{x}$ on which the instrument is focused. The geometry is shown schematically in Fig. 9. The 'photographic' mode is obtained when the resolution in the direction parallel to $\hat{r}$ is so poor as to result effectively in a two rather than three (or a one rather than two) dimensional record. In the present analysis we will be concerned only with sensing systems that approximate the mode for which the resolution in range is very much poorer than the resolution

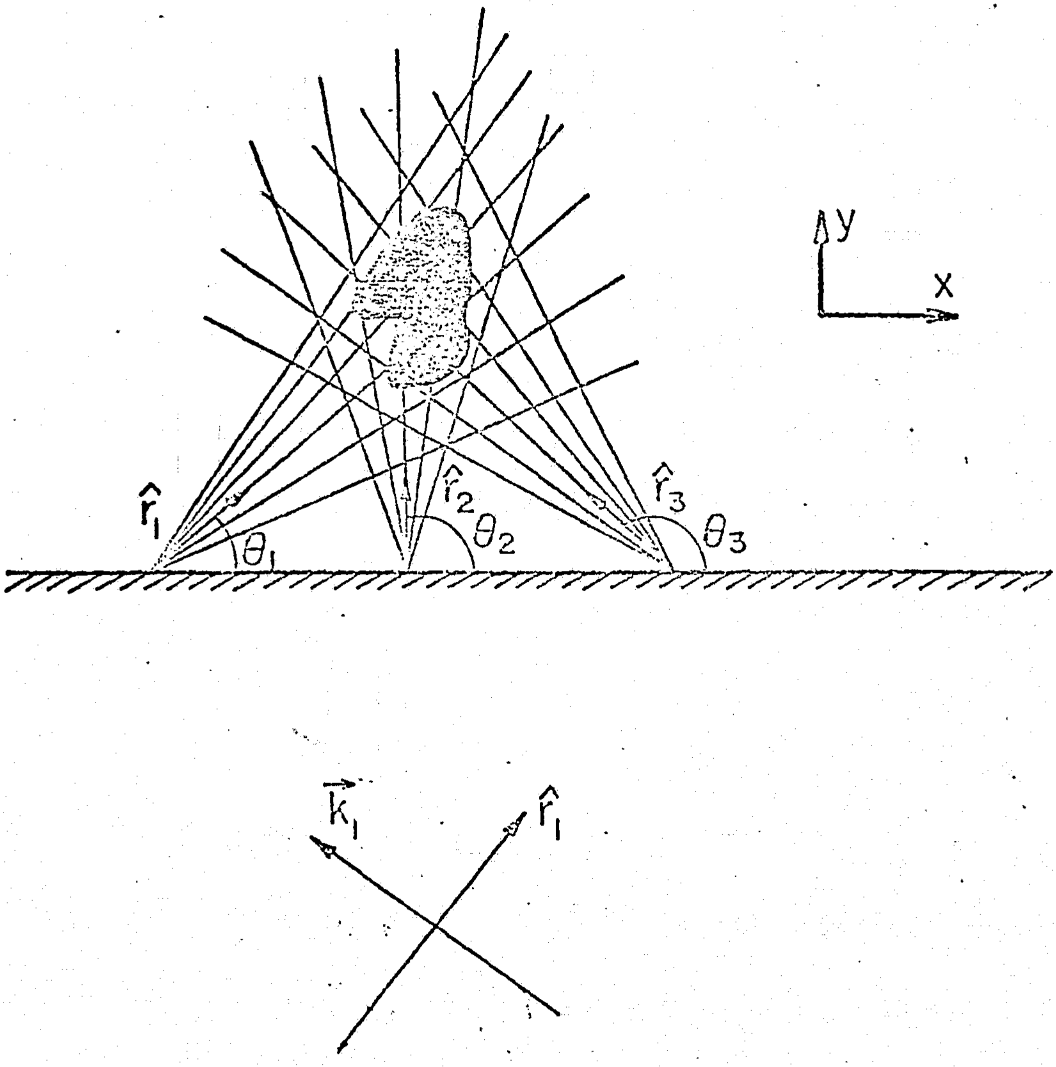

Figure 9. Geometry of Recording System

in azimuth. Good spatial resolution is then achieved only perpendicular to the viewing direction. Depth perception or range resolution is achieved by invoking the stereo effect (i.e. triangulation or parallax). To utilize this effect to obtain depth resolution, comparisons and correlations must be made between the various projections obtained by viewing in more than one direction. In this way the good lateral resolution is used also to achieve localization in range (depth). In the normal photographic viewing situation the target consists of discrete points which can be identified and correlated in the different views. However, in a diffuse scene, there are no such sharply defined features and the ability of an observer to sense depth from even two widely separated views deteriorates.

It is the purpose of this analysis to construct a model of the multi-viewing process for generalized scenes and to construct a mathematical procedure for combining the various projections into a processed full dimensional scene.

Normally a three-dimensional scene is viewed and recorded as two (or more) two-dimensional projections (pictures). For the present analysis however we restrict ourselves to strictly two-dimensional scenes which are recorded as a number of imperfectly resolved two-dimensional scenes or, in the 'photographic' mode, as one-dimensional projections.

We will first (Sec. IV. 2.1) develop the theory for the imaging of a scalar field, such as a variable density of scatterers $\sigma(x,y)$. Secondly we will consider in Sec. IV.2.2 the imaging of a vector field i.e. typically a wind velocity vector field by extending the analysis developed in Sec. IV.2.1.

IV.2 Theory

IV.2.1 SCALAR MODE

We consider the record of a two-dimensional scene as observed with a recording instrument viewing the scene in the direction $\hat{r}$ with finite spatial resolution. When the instrument is set to measure the scene brightness at the point $\vec{x}$, the actual contribution to the recorded value at this point comes from points in the scene in the neighborhood of $\vec{x}$:

$$S(\vec{x},\hat{r}) = \int_{-\infty}^{\infty}\int_{-\infty}^{\infty} G(\vec{s},\hat{r})\ \sigma(\vec{x}+\vec{s})\ ds_x ds_y \qquad (1)$$

Here $G(\vec{s},\hat{r})$ is the resolution function of the instrument and $\sigma(\vec{x})$ is the local brightness of the scene. The unit vector $\hat{r}$ represents the viewing direction. We are particularly interested in resolution function $G(\vec{s},\hat{r})$ of the general form shown in Fig. 10 in which the lateral resolution is very much better than the longitudinal resolution.

ORIGINAL PAGE IS
OF POOR QUALITY

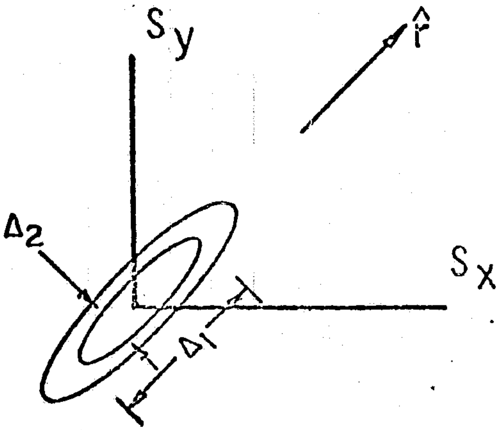

Fig. 10. Contours for the resolution function $G(\vec{s},\hat{r})$ (see Eq. 5 for definition of Δ_1 and Δ_2)

The spatial Fourier Transform of Eq. 1 has the form

$$s(\vec{k},\hat{r}) = g(\vec{k},\hat{r})\ \sigma(\vec{k}) \tag{2}$$

Conceptually it is possible to recover the scene properties (i.e., $\sigma(\vec{x})$ or, equivalently, $\sigma(\vec{k})$) by dividing by $g(\vec{k},\hat{r})$:

$$\sigma(\vec{k}) = \frac{s(\vec{k},\hat{r})}{g(\vec{k},\hat{r})} \tag{3}$$

However, in the presence of finite noise or measurement error, this result is very poorly evaluated in regions where $g(\vec{k},\hat{r})$ is small. Here the noise (n) contained in the measured signal

$$s(\vec{k},\hat{r}) = s_o(\vec{k},\hat{r}) + n(\vec{k},\hat{r}) \tag{4}$$

is strongly amplified and could destroy the image.

The objective of the stereo viewer now is to utilize the fact that data has been taken at different values of $\hat{r}$. Thus he wants to choose $\hat{r}$ as a function of $\vec{k}(=\hat{r}_o(\vec{k}))$ such that $g(\vec{k},\hat{r}_o(\vec{k}))$ is never small. In this way different Fourier components are to be evaluated from different views.

For example, consider the resolution function

$$G(\vec{s},\hat{r}) = \left(\pi\Delta_1\Delta_2\right)^{-1} \exp\left\{-\left(\frac{(\vec{s}\cdot\hat{r})^2}{\Delta_1^2} + \frac{(\vec{s}\times\hat{r})^2}{\Delta_2^2}\right)\right\} \tag{5}$$

This is an asymmetric Gaussion with its long axis (taking $\Delta_2 < \Delta_1$) pointed in the direction $\hat{r}$. The transform $g(\vec{k},\hat{r})$ can be explicitly evaluated:

$$g(\vec{k},\hat{r}) = \int_{-\infty}^{\infty}\int_{-\infty}^{\infty} G(\vec{s},\hat{r})\, e^{-i\vec{k}\cdot\vec{s}}\, ds_x ds_y$$

$$= \exp\left\{-\ (\vec{k}\cdot\hat{r})^2\ \Delta_1^2/4 - (\vec{k}\times\hat{r})^2\ \Delta_2^2/4\right\} \tag{6}$$

For good recovery of the object scene when $\Delta_2 << \Delta_1$ the solution $\sigma(\vec{k})$ should be evaluated from Eq. 3 with $\vec{k}\cdot\hat{r}$ maintained as small as possible, i.e., if possible near $\vec{k} = \hat{\eta}k$ where $\hat{\eta}$ is a unit vector perpendicular to $\hat{r}$.

Simulated Example

In order to demonstrate the viewing process, we consider a simple distribution of diffuse targets described by:

$$\sigma(\vec{x}) = \sum_n \alpha_n \exp\left(-(\vec{x}-\vec{x}_n)^2/a_n^2\right) \qquad (8)$$

and we imagine that the observer views this field with the response function:

$$G(\vec{s},\hat{r}) = \frac{1}{\pi\Delta_1\Delta_2} \exp\left\{-\frac{(\vec{s}\cdot\hat{r})^2}{\Delta_1^2} - \frac{(\vec{s}\times\hat{r})^2}{\Delta_2^2}\right\} \qquad (9)$$

For values of a_n much smaller than Δ_1 and Δ_2 and as well less than the mutual separations, the targets appear as individual discrete points. On the other hand, when the a_n's are large, the scene brightness is smooth and slowly varying.

The measured signal in the absence of noise has the form

$$S_o(\vec{x},\hat{r}) = \sum_n \alpha_n \int_{-\infty}^{\infty}\int_{-\infty}^{\infty} \exp\left(-\frac{(\vec{s}\cdot\hat{r})^2}{\Delta_1^2} - \frac{(\vec{s}\times\hat{r})^2}{\Delta_2^2} - \frac{(\vec{x}+\vec{s}-\vec{x}_n)^2}{a_n^2}\right)\frac{ds_x\,ds_y}{\pi\Delta_1\Delta_2} \qquad (10)$$

Here the unit vector $\hat{r}$ in direction of line of sight has the components (see Fig.13) $\hat{r} = (\cos\Theta, \sin\Theta)$ and $\vec{s}(=(s_x,s_y))$ is the vector displacement from the instrument setting $\vec{x}$.

At a given value of $\hat{r}$ (i.e. a given view) $S(\vec{x},\hat{r})$ $(=s_o(\vec{x},\vec{r})$ + noise) is the recorded image. A normal two-view stereo image would have two images taken at two different values of $\hat{r}$. ($\hat{r}_1$ and $\hat{r}_2$). In the "photographic" mode, the depth of field, Δ_1, is typically very large compared to the lateral resolution Δ_2.

For our example of an assembly of diffuse targets (Eq. 8), the signal can be evaluated explicitly:

$$s_o(\vec{x},\hat{r}) = \sum_n \frac{\alpha_n a_n^2}{\left[\left(a_n^2+\Delta_1^2\right)\left(a_n^2+\Delta_2^2\right)\right]^{1/2}} \exp\left\{-\frac{\left[(\vec{x}-\vec{x}_n)\cdot\hat{r}\right]^2}{a_n^2+\Delta_1^2} - \frac{\left[(\vec{x}-\vec{x}_n)\times\hat{r}\right]^2}{a_n^2+\Delta_2^2}\right\} \qquad (11)$$

We allow for measurement error with a noise term $N(\vec{x},\hat{r})$ which is to be obtained by constructing independent realizations of the viewed field for each viewing direction $\hat{r}$. We assume the noise to be homogeneous (i.e. $\langle N(\vec{x},\hat{r})\rangle$ the expectation $= N_o$ = constant).

Thus the net measured signal is

$$S(\vec{x},\hat{r}) = S_o(\vec{x},\hat{r}) + N(\vec{x},\hat{r}) \qquad (12)$$

The Fourier transform of the signal alone can be explicitly evaluated in the form

$$S_{o\vec{k}}(\hat{r}) = \sum_n \alpha_n a_n^2 \exp\left[-\frac{1}{4}(\vec{k}\cdot\hat{r})^2 (a_n^2+\Delta_1^2) - \frac{1}{4}(\vec{k}\times\hat{r})^2 (a_n^2+\Delta_2^2)\right]$$

$$\times \exp(-i\vec{k}\cdot\vec{x}_n) \qquad (13)$$

The noise field itself we take as white, that is,

$$n_{\vec{k}} = N_o e^{i\phi_{\vec{k}}}, \tag{14}$$

where $\phi_{\vec{k}}$ is a random quantity uniformly distributed in $(0,2\pi)$.

The deduced Fourier transform of the object field is obtained by dividing by the transform of the instrumental response function.

$$\sigma'_{\vec{k}} = s_{\vec{k}}/g_{\vec{k}} = \frac{s_{o\vec{k}}(\hat{r})}{g_{\vec{k}}(\hat{r})} + \frac{n_{\vec{k}}(\hat{r})}{g_{\vec{k}}(\hat{r})} \tag{15}$$

The instrument response function transform is

$$g_{\vec{k}} = \exp\left(-\left(\frac{\vec{k}\cdot\hat{r}\Delta_1}{2}\right)^2 - \left(\frac{(\vec{k}\times\hat{r})\Delta_2}{2}\right)^2\right) \tag{16}$$

To avoid singularities at high $\vec{k}$ we introduce a weighting function $w(\vec{k})$ and get our final expression for the processed image:

$$\sigma'_{\vec{k}} = s_{\vec{k}} w_{\vec{k}}/g_{\vec{k}} \tag{17}$$

with

$$s_{\vec{k}} = \left[S_{o\vec{k}}(\hat{r}) + n_{\vec{k}}(\hat{r})\right] \tag{18}$$

There are two limiting cases

i) <u>Deconvolution Solution</u>

This arises if $w(\vec{k}) = 1$ and noise $n_{\vec{k}} \to 0$, giving the solution

$$\sigma'_{\vec{k}} = S_o(\vec{k},\hat{r})/g(\vec{k},\hat{r})$$

ii) <u>Matched Filter Solution</u>

This arises if $w(\vec{k}) = w(\vec{k})_{opt}$ where $w(\vec{k})_{opt}$ is the optimal weighting function specified by choosing

$$w_{\vec{k}} = \frac{|g_k|^2 \left(1 + \langle |n_{\vec{k}}|^2 \rangle / S_o{}^2\right)}{|g_{\vec{k}}|^2 + \langle |n_{\vec{k}}|^2 \rangle / S_o{}^2} \tag{19}$$

where $S_o{}^2$ is the signal power $\left(S_o{}^2 = \sum_{\vec{k}} |S_k{}^2|.\right)$ For the white noise case:

$$w_{\vec{k}} = \frac{|g_{\vec{k}}|^2 \left(1 + N_o{}^2/S_o{}^2\right)}{|g_{\vec{k}}|^2 + N_o{}^2/S_o{}^2} \tag{20}$$

The matched filter solution in the absence of noise $n_{\vec{k}}$ is then

$$\sigma'(\vec{k}) = s_o(\vec{k},\hat{r})\, g^*(\vec{k},\hat{r}) \frac{\left(1 + (N/S)^2\right)}{\left(|g(\vec{k},\hat{r})|^2 + (N/S)^2\right)} \tag{21}$$

For the case of N_v viewing directions (21) may be generalized to a weighted average over the various views:

$$\sigma'(\vec{k}) = \sum_{\text{views}} s_o(\vec{k},\hat{r}_i) \left\{ \frac{g^*(\vec{k},\hat{r}_i)\left(1 + (N/S)^2\right)}{|g(\vec{k},\hat{r}_i)|^2 + (N/S)^2} \right\} w(\vec{k},\hat{r}_i) \Big/ \sum w(\vec{k},\hat{r}_i) \tag{22}$$

A fundamental problem in reconstruction of the multi-dimensional image arises when there are only a discrete set of values of $\hat{r}$ at which measurements have been made. Although it would appear from Eq. (21) that a large number of separate views are required to determine the spatial function $\sigma(\vec{x})$ in general, experience tells us that this is commonly not the case. For example, the principle that only two two-dimensional projections are often all that is required to reconstruct a complete three-dimensional image in universally used in conventional stereo optical systems.* We expect, however, that such simple reconstruction is possible only under certain conditions; that is, when the object is made up of a finite number of discrete and identifiable points (or lines in 3-D). In order to test this hypothesis we simulate the essential features of such scenes by taking a_n much smaller than both Δ_1 and Δ_2, and choosing α_n large enough that noise can be ignored ($n_{\vec{k}} \rightarrow 0$).

In this case the measured signal takes the form

---

*including homosapiens

$$S(\vec{x},\hat{r}) = \sum_{n=1}^{N} \alpha_n \exp\left[- \frac{\left[(\vec{x}-\vec{x}_n)\cdot\hat{r}\right]^2}{\Delta_1^{\,2}} - \frac{\left[(\vec{x}-\vec{x}_n)\times\hat{r}\right]^2}{\Delta_2^{\,2}}\right] \frac{a_n^{\,2}}{\Delta_1\Delta_2} \tag{23}$$

and the Fourier transform of the signal is

$$s_{o_{\vec{k}}}(\hat{r}) = \sum_{n=1}^{N} \alpha_n \, a_n^{\,2} \exp\left(- \tfrac{1}{4}(\vec{k}\cdot\hat{r})\, \Delta_1^{\,2} - \tfrac{1}{4}(\vec{k}\times\hat{r})^2 \, \Delta_2^{\,2} - i\vec{k}\cdot\vec{x}_n\right) \tag{24}$$

When a sufficiently large number of views have been measured it is possible to select $\hat{r}$ at each $\vec{k}$ to be perpendicular to $\vec{k}$ $(r = \vec{\eta}(\vec{k})$ where $\vec{\eta}.\vec{k} = 0)$. In this case the signal has the form

$$s_{o_{\vec{k}}}(\hat{r} = \hat{\eta}(\vec{k})) = \sum_{n=1}^{N} \alpha_n \, a_n^{\,2} \exp(-k^2\Delta_2^{\,2}/4 - i\vec{k}.\vec{x}_n) \tag{25}$$

This signal in x-space has the form

$$S_o(\vec{x}) = \int \sigma(\vec{x}+\vec{s}) \, G_2(\vec{s}) \, ds_x \, ds_y \tag{26}$$

where

$$G_2(\vec{s}) = \exp(-\vec{s}^{\,2}/\Delta_2^{\,2}) \Big/ (\pi\Delta_2^{\,2})$$

Thus, when enough views are available, it is possible to reconstitute the signal as it would have been seen by a sensor with the orignal lateral resolution Δ_2 in both range and azimuth. This is true regardless of the value of the original range resolution Δ_1. This is the essence of the multiview process.

The number of view directions required to permit the choice $\hat{r} = \eta(\vec{k})$ is, in general, equal to L/Δ where L is the dimension of the viewed area and Δ the desired resolution (i.e. $\Delta \approx \Delta_2$).

If only a smaller number of views have been measured, it will not be possible to choose $\hat{r}(\vec{k})$ perpendicular to $\vec{k}$ for every direction and approximation procedures are required first to fill in the regions of $\vec{k}$-space not covered by the different measured viewing directions. One such procedure could be logarithmic interpolation in k space in regions of small $\sigma'(\vec{k})$ as illustrated in Fig. 11. It can be shown that this procedure will reduce the number of views required when the structured region occupies only a small area within the total viewed area. In this case the number of views required, when Δ_1 is very large, is reduced to $\delta L/\Delta$ where δL is the dimension of the structured region. Similarly, when Δ_1 is finite, the number of views never needs to be greater than Δ_1/Δ. Examples of these processing techniques are discussed more fully in Section IV.3.3.

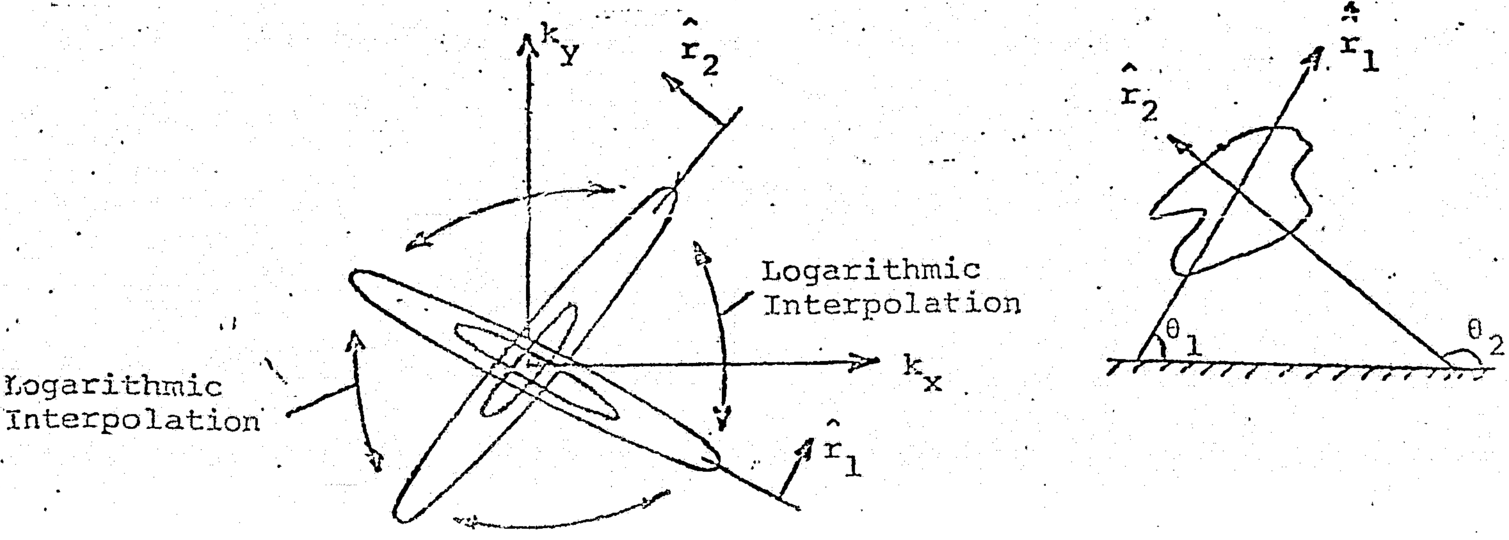

Fig. 11. Interpolate in $\vec{k}$ space in Regions of Small $\sigma'(k)$

IV.2.2 Vector Mode

The basic concepts of this section closely follows that of Section IV.2.1 with extensions to account for the vector field.

In this mode a velocity vector field is specified over the spatial region: $\vec{u}(x,y) = (u(x,y), v(x,y))$.

For example calculations, we have chosen a velocity field that simulates a cross-section of the horizontal wind field of a storm advancing through the surrounding atmosphere (Fig. 12). This field can be represented for simulation purposes by

$$\vec{u}(x,y) = \vec{u}_o + \sum_{i=1}^{\text{vortex centers}} \frac{(\vec{x}-\vec{x}_i) \times \vec{\Gamma}_i}{|\vec{x}-\vec{x}_i|^2} \left(1 - e^{\frac{-|\vec{x}-\vec{x}_i|^2}{a_i^2}} \right) \tag{27}$$

where $\vec{x}_i$ = position of vortex center i

a_i = 1/e radius of vortex i

$\vec{u}_o$ = constant vector velocity.

$\vec{\Gamma}_i = (0,0,\Gamma)$ and Γ = vortex strength

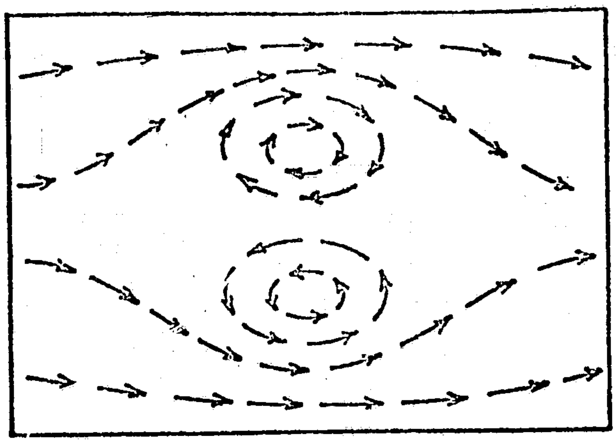

Fig.12. Typical Velocity Field Distribution

For these calculations we take the scattering coefficient to be independent of position.

Eq. 1 again gives the zeroth Doppler moment sensed by the instrument at the point $\vec{x}$ i.e.

$$S_o(\vec{x},\hat{r}) = \int \sigma(\vec{x}')\ G(\vec{x}-\vec{x}',\hat{r})\,d\vec{x}'$$

This would be evaluated by the instrument from the measured Doppler spectrum I(f):

$$\sim \int I(f)\,df$$

In additon we must sense the first Doppler moment:

$$S_{\|}(\vec{x},\hat{r}) = \int \sigma(\vec{x}')\ u_{\|}(\vec{x},\hat{r})\ G(\vec{x}-\vec{x}',\hat{r})\,d\vec{x}'$$

$$\sim \int fI(f)\,df$$

The geometry is shown schematically in Fig. 13. Here $u_{\parallel}(\vec{x},\hat{r})$ is the velocity in the viewing direction $\hat{r}$.

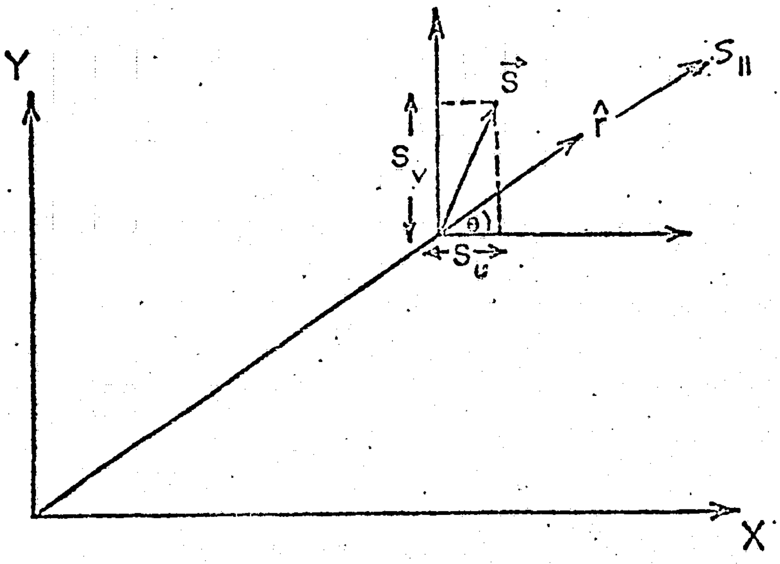

Figure 13. Velocity Components in Viewed Field

The horizontal and vertical components of the first moment can be written down as follows:

$$S_u(\vec{x},\hat{r}) = \int \sigma(\vec{x}')\,u(\vec{x}')\,G(\vec{x}-\vec{x}',\hat{r})\,d\vec{x}' \quad : \quad \text{horizontal} \qquad (30)$$

$$S_v(\vec{x},\hat{r}) = \int \sigma(\vec{x}')\,v(\vec{x}')\,G(\vec{x}-\vec{x}',\hat{r})\,d\vec{x}' \quad : \quad \text{vertical} \qquad (31)$$

and hence

$$S_{\parallel} = S_u \cos\theta + S_v \sin\theta \qquad (32)$$

The spatial Fourier transform of Eq. 28 (see Eq. 1) has the form

$$S_o(\vec{x},\hat{r}) \rightarrow s_o(\vec{k},\hat{r}) = \sigma(\vec{k})\ g(\vec{k},\hat{r}) \qquad (33)$$

Similarly the spatial Fourier transforms of Eq. 30 and Eq. 31 are given by

$$S_u(\vec{x},\hat{r}) \rightarrow s_u(\vec{k},\hat{r}) = (\sigma u)_{\vec{k}}\; g(\vec{k},\hat{r}) \qquad (34)$$

$$S_v(\vec{x},\hat{r}) \rightarrow s_v(\vec{k},\hat{r}) = (\sigma v)_{k}\; g(\vec{k},\hat{r}) \qquad (35)$$

The simulated measured data is now two quantities in $\vec{k}$ space at a given viewing direction $\hat{r}_J$ $S_o(\vec{x},\hat{r})$ and $S_{\|}(\vec{x},\hat{r})$.

Combining Eq. 32, Eq. 34 and 35 we have

$$s_{\|}(\vec{k},\hat{r}) = \left[(\sigma u)_{\vec{k}} \cos\theta + (\sigma v)_{\vec{k}} \sin\theta\right] g(\vec{k},\hat{r}) \qquad (36)$$

For this vector field two or more views are required to reconstruct the scene. Taking Eq. 36 at two different viewing directions $\hat{r}_1$, and $\hat{r}_2$ (or at viewing angles θ_1 and θ_2) we can solve for $(\sigma u)_{\vec{k}}$ and $(\sigma v)_{\vec{k}}$ to give the matched filter solutions for the velocity components as

$$(\sigma u)'_{\vec{k}} = \left[\frac{s_{\|}(\hat{r}_1)\ \sin\theta_2 \bar{g} g_1^*}{|g_1|^2 + (N/S)^2} - \frac{s_{\|}(\hat{r}_2)\ \sin\theta_1 \bar{g} g_2^*}{|g_2|^2 + (N/S)^2}\right] \Bigg/ \sin(\theta_2 - \theta_1) \qquad (37)$$

$$(\sigma v)'_{\vec{k}} = \left[\frac{-s_{\|}(\hat{r}_1)\ \cos\theta_2 \bar{g} g_1^*}{|g_1|^2 + (N/S)^2} + \frac{s_{\|}(\hat{r}_2)\ \cos\theta_1 \bar{g} g_2^*}{|g_2|^2 + (N/S)^2}\right] \Bigg/ \sin(\theta_2 - \theta_1) \qquad (38)$$

where $\bar{g} = 1 + (N/S)^2$. These components can be averaged over a number of sets of pairs of views $\left(N_{\text{pairs}}\right)$ to give

$$(\sigma u)'_{\vec{k}} = \frac{1}{N_{\text{pairs}}} \sum_{\substack{\text{pairs of} \\ \text{views}}} (\text{Eq. } 37) \qquad (39)$$

$$(\sigma v)'_{\vec{k}} = \frac{1}{N_{\text{pairs}}} \sum_{\substack{\text{pairs of} \\ \text{views}}} (\text{Eq. } 38) \qquad (40)$$

Note that because of possibility of small denominators in Eq. 37 and 38, these sums should be restricted to only the more widely separated pairs of views. As before logarithmic interpolation can be used to interpolate in regions of small $(\sigma u)'_{\vec{k}}$ and small $(\sigma v)'_{\vec{k}}$. Performing the inverse transform to $\vec{x}$ space gives

$$u(\vec{x}) = (\sigma u)'/\sigma' \qquad (41)$$

and

$$v(\vec{x}) = (\sigma v)'/\sigma' \qquad (42)$$

IV.3 Simulation of a Multiview System

IV.3.1 Introduction

The procedures described in the preceding section have been formulated on a computer and a number of simulations carried out for both scalar and vector fields. The basic features of the output and display are shown in an example in Fig. 14, 15. Here the scene is taken to be the word NASA represented by a sequence of simulated Gaussian shaped scattering centers. Two types of output display are shown: a contour plot of the processed image field and a raster plot where the intensity is proportional to the computed local image density. In Figures 14a and 15a the original scene is shown and in Figures 14b and 15b the scene as seen by a single sensor with a range resolution equal to 1/4 times the image letter heights. Matched filtering has been used to construct the images with an assumed SNR for the matched filter of 1.0. However, no noise was actually present in the simulated data. For a single view (Fig. 14b, 15b) the sensor resolution is inadequate to resolve the pattern. Figures 14c, d, e and 15c, d, e show how the processed spatial resolution improves and the pattern emerges as the number of views is increased. The pattern is recognizable with four views and very clear with 24 views.

Example of a Multivew Scene - Raster Plot

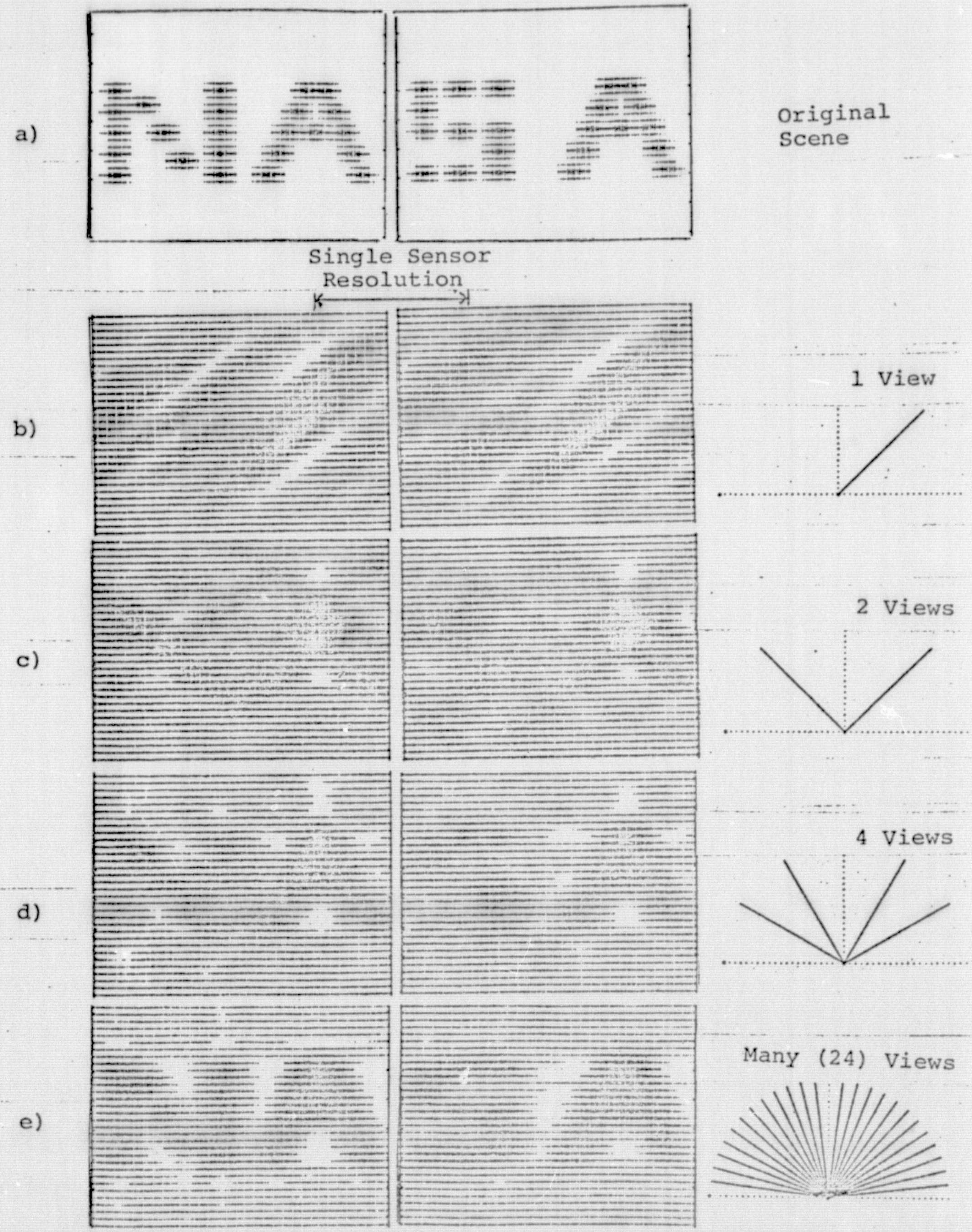

Figure 14

Example of a Multiviewed Scene - Contour Plot

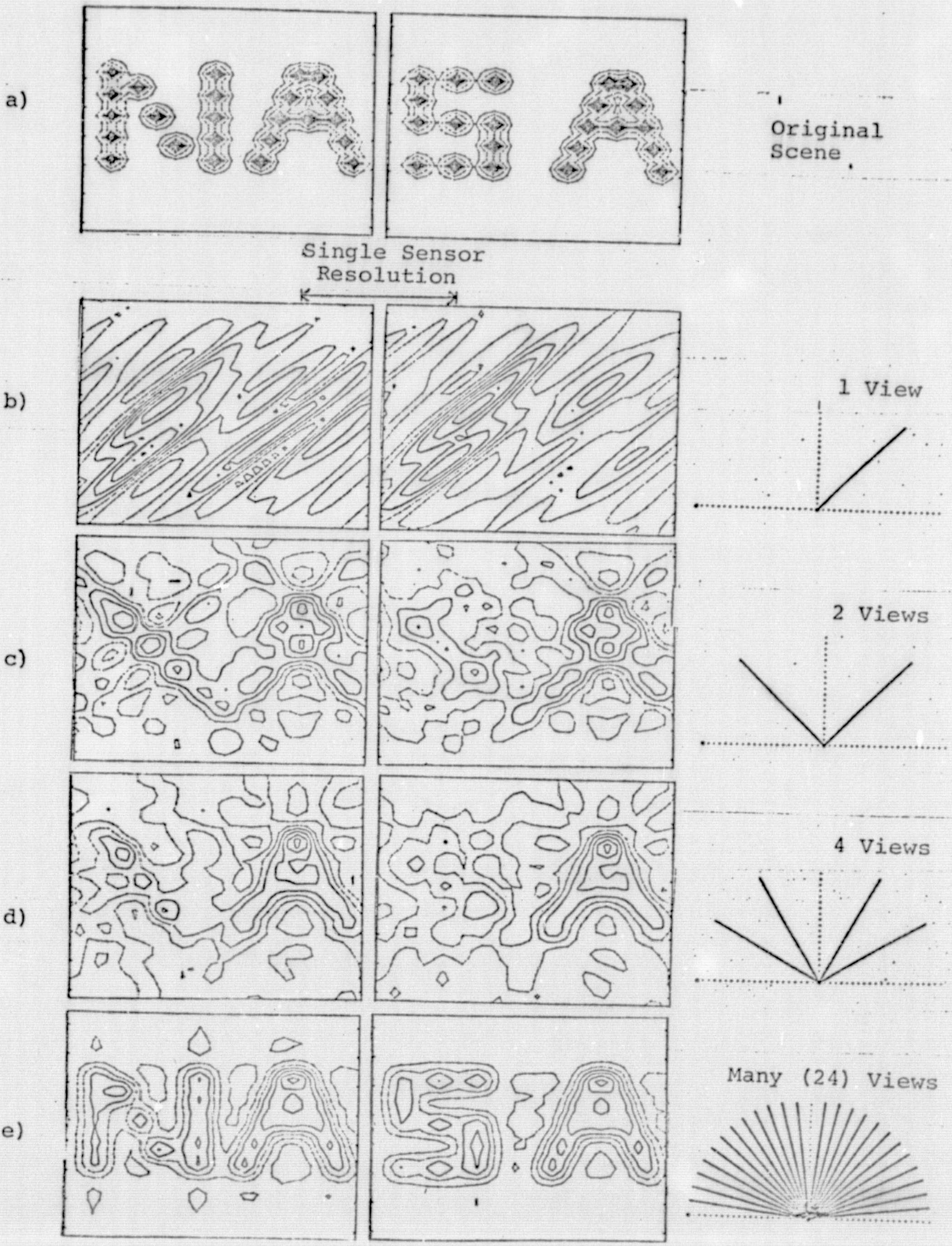

Figure 15

The basic problem now is to quantify the processing procedures so that the relationship between single sensor resolution, number of views, processing filters and final image resolution can be established. A quantitative measure of the quality of the image reconstruction is required. The Rayleigh criteria for defining the resolving power of an optical system is a standard method. It gives a good measure of the smallest scale structure that the instrument will sense. However, it is not very useful in this application since it gives no indication of distorted or false images or of the presence of other processing induced irregularities. We have found the cross correlation coefficient between the reconstructed image and the original scene to be a useful measure of image quality. This quantity is defined as

$$C_o = \frac{\int \sigma'(\vec{x})\ \sigma_o(\vec{x})\, dxdy}{\left[\int \sigma'^2(\vec{x})\, dxdy \int \sigma_o^2(\vec{x})\, dxdy\right]^{\frac{1}{2}}}$$

where $\sigma_o(x)$ is the original scene and $\sigma'(\vec{x})$ the reconstruction.

For simple localized images, this correlation coefficient can be interpreted directly in terms of a spatial resolution. For example, for a source distribution of the form e^{-x^2/Δ_s^2} and an image distribution of the form e^{-x^2/Δ_I^2}, the cross correlation is

$$C_o^2 = \frac{2}{\frac{\Delta_s}{\Delta_I} + \frac{\Delta_I}{\Delta_s}} \tag{44}$$

For an image which is much broader than the original source the quantity $2/C_o{}^2$ is effectively the ratio of the image dimension to the original source size (Δ_I/Δ_S). Because of this simple relationship between resolution and correlation coefficient we will use the quantity C_o^2 as the appropriate measure for comparing different processing techniques.

IV.3.2 Results

To test the multiview process a number of simulations were run using test patterns for both scalar and vector fields for the original scene (see Sec. IV.2). The data is presented in two forms: contour plots and raster plots, the former being more useful for quantitative analysis and the latter giving a more pictorial sense of the data. In Figures 16 and 17 we show the effect of varying the number of views for two different sensor resolutions for a scalar field. The original scene of three Gaussian shaped scalar scattering sources is also shown. The upper four figures correspond to a very poor initial spatial resolution ($2\Delta_1 = \Delta X_o = 24$ units) and show a substantial improvement of the scene resolution as the number of views

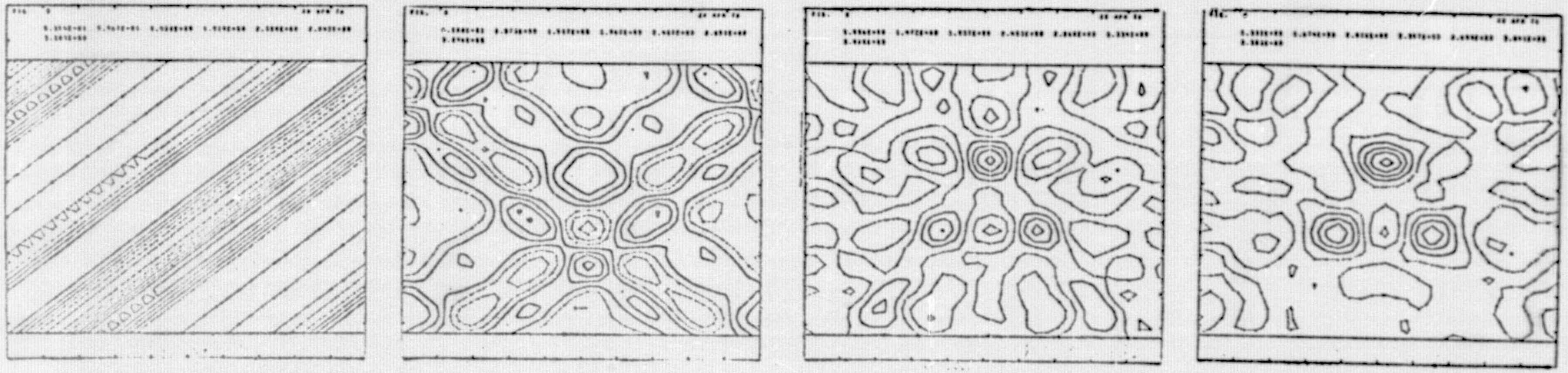

1 View $2\Delta_1 = 24$

2 View $2\Delta_1 = 24$

4 View $2\Delta_1 = 24$

8 View $2\Delta_1 = 24$

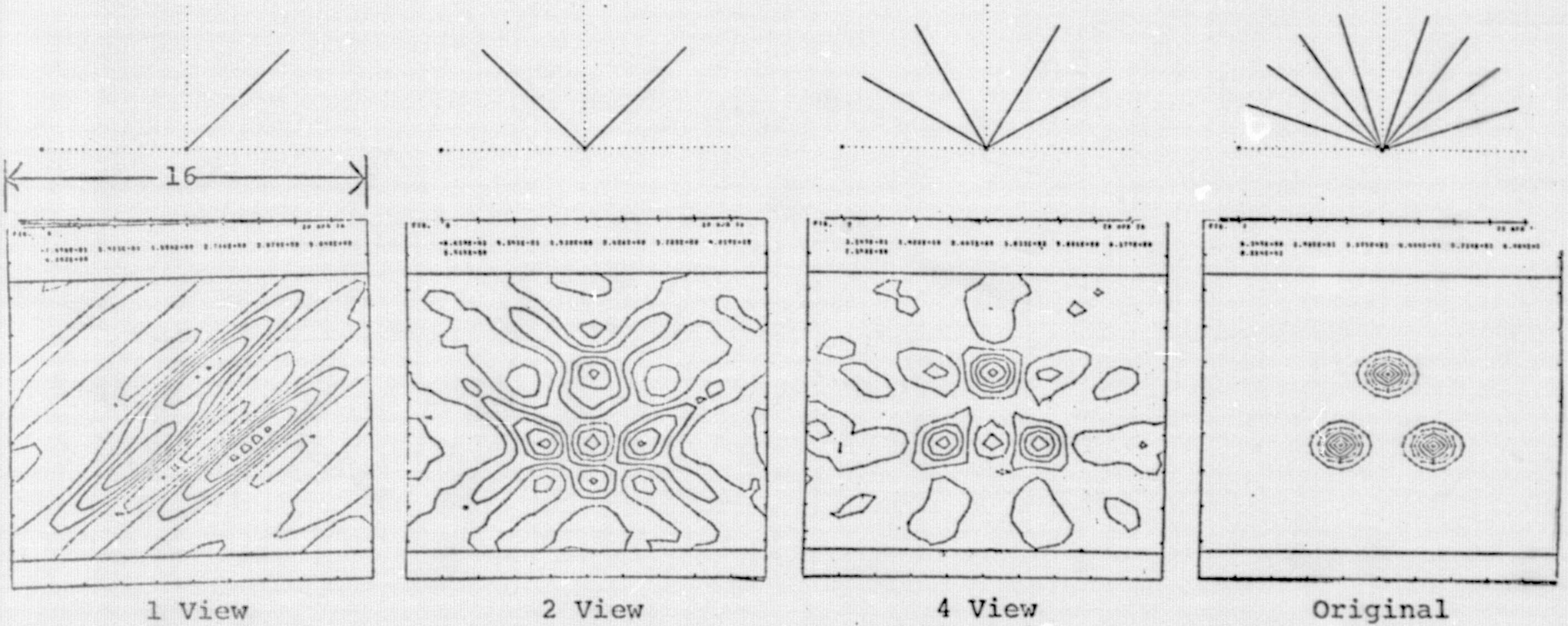

1 View $2\Delta_1 = 8$

2 View $2\Delta_1 = 8$

4 View $2\Delta_1 = 8$

Original Scene

Fig. 16. Reconstruction of a Scalar Field (Contour Plots).

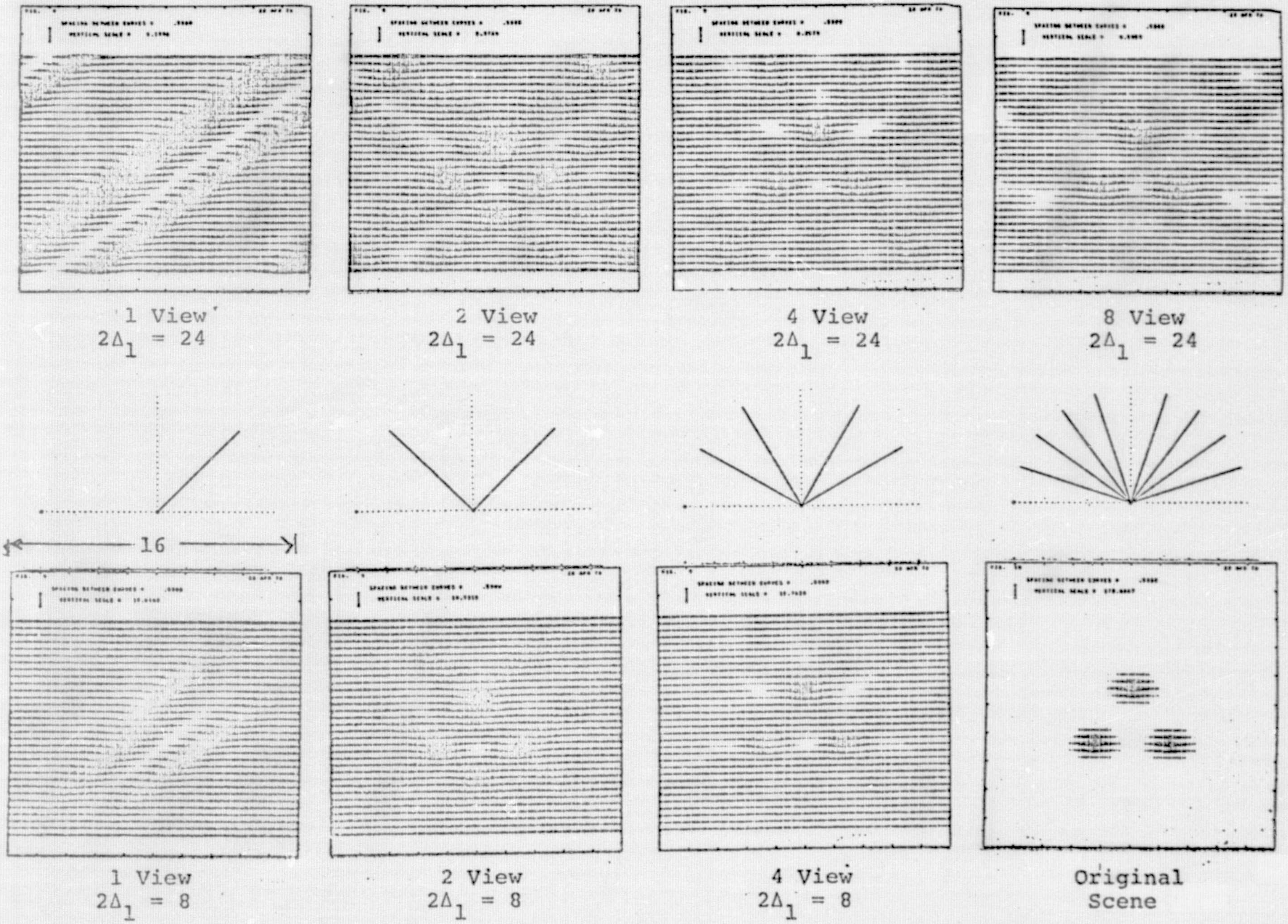

1 View
$2\Delta_1 = 24$

2 View
$2\Delta_1 = 24$

4 View
$2\Delta_1 = 24$

8 View
$2\Delta_1 = 24$

1 View
$2\Delta_1 = 8$

2 View
$2\Delta_1 = 8$

4 View
$2\Delta_1 = 8$

Original
Scene

Fig. 17. Reconstruction of a Scalar Field (Raster Plot).

is increased. The lower three figures have a higher spatial resolution to start with and achieve the same resolution as the first set at a lower number of views. This effect is shown more quantitatively in Figures 18 and 24. In Figure 18 we show how the correlation quantity C_o^2 (for a two-view model) decreases with deteriorating sensor resolution, and shows roughly the inverse relation expected from Eq. 44. In Figure 24, we show in a quantitative way how increasing the number of views can offset this degradation.

Two signal-to-noise values enter into these simulations: a) the actual instrument noise that is to be added to the simulated measured quantity before processing and b) the assumed or expected value of the signal-to-noise value that is to be included in the matched filter expression. In most of the calculations shown a rather low (but finite) value of instrumental noise was selected in order to demonstrate the expected profile of the signal. Various values for S/N of the matched filter were selected for demonstration purposes. However, it is to be noted that in practice the best results will be obtained by matching the filter S/N to that of the actual signal. In Figures 19 and 20 we show the effect of varying the actual instrumental or background noise in a typical example. Here it is seen that too low a value of S/N in the filter leads to a

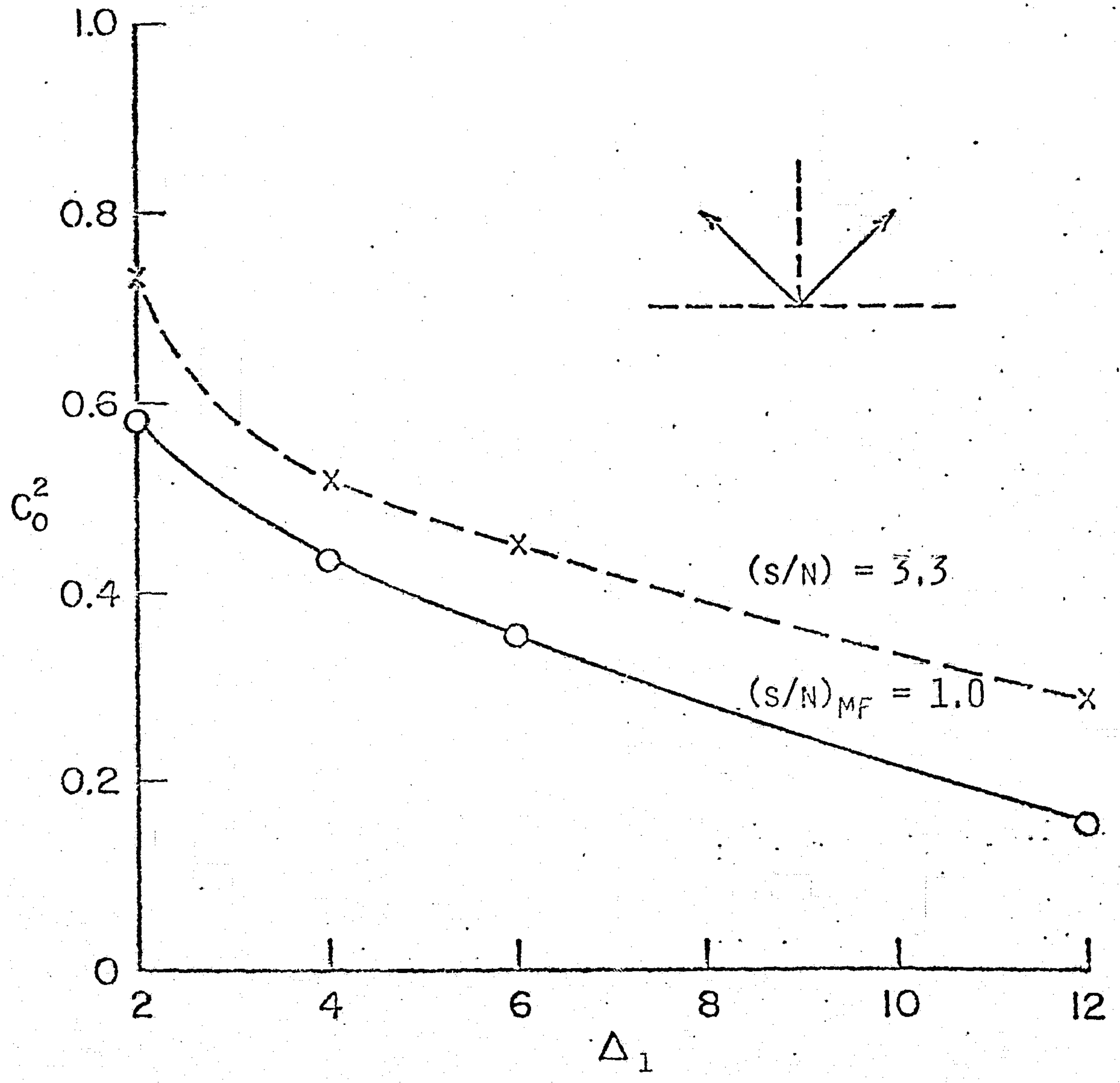

Fig. 18. Image quality parameter C_0^2 for a two-view reconstruction of the scalar field shown in Figs. 16 and 17 (Δ_1 = 1/2 range resolution between 3 db points). Values for the (voltage) S/N level assumed in the matched filter are indicated.

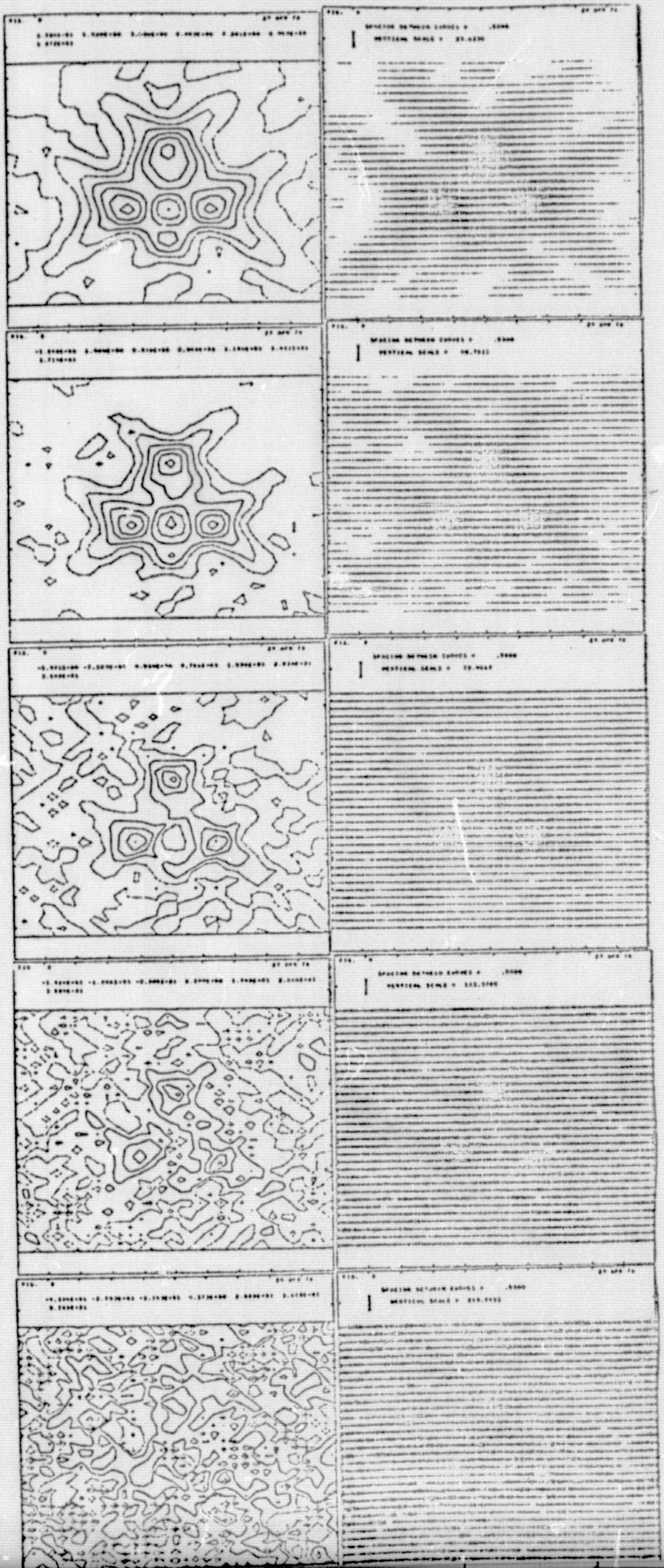

(a)
S/N = 1.0

(b)
S/N = 3.2

(c)
S/N = 10

(d)
S/N = 32

(e)
S/N = 100

Fig. 19. Effect of the Assumed Value of N/S in Matched Filter (At a fixed instrument S/N = 25

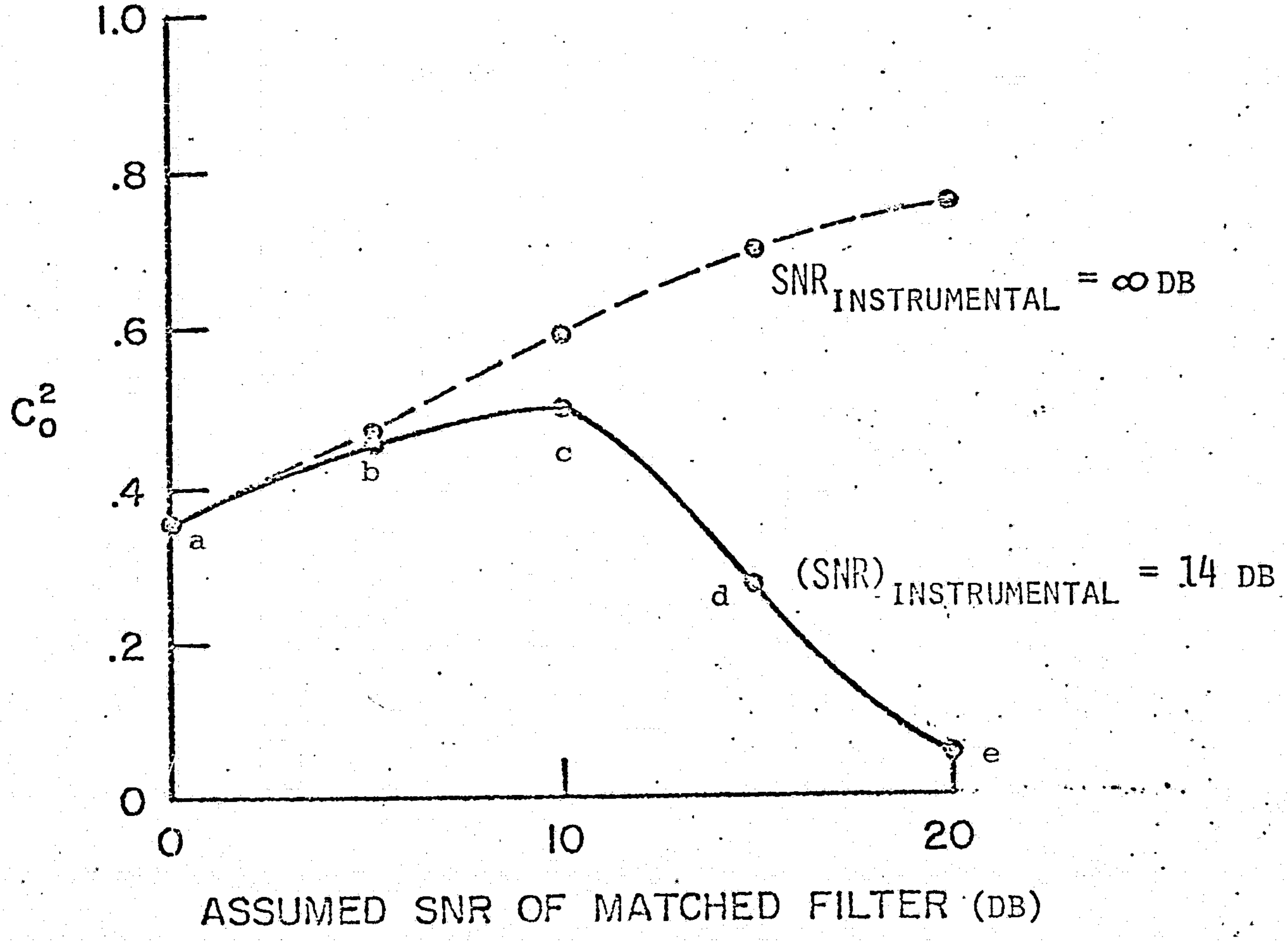

Figure 20. Variation of the image quality with assumed value of the signal-to-noise ratio in the matched filter. (Pictures in Figure 19 refer to points at a, b, c, d and e)

broadened pattern whereas too high a value leads very noisy looking data. The 'best' image, as defined by the correlation coefficient C_o^2 being maximum, occurs when the S/N of the filter is matched to that of the signal (Figure 20).

In Figures 21, 22 we show a similar set of simulations to those of Figs. 16, and 17 except now for a vector field. The scalar quantity presented in these figures is now the speed $(u^2+v^2)^{1/2}$ rather than the cross-section. The vector field chosen for this example is that given in Section IV.2.2, Eq. 27 and was chosen as a rough simulation of the horizontal velocity field of a moving storm.

In addition to the contour and raster plots of the speed, we also show vector plots of the velocity (Figure 23). The velocity vector at any point is given by a line whose length is proportional to the speed and whose direction is indicated by the point at the front of the line.

From the two-dimensional reconstructions just described we have constructed a set of curves relating the number of viewing directions to the basic sensor resolution length $(2\Delta_1)$ for fixed values of the correlation coefficient C_o. The plots are presented as a function of the inverse of Δ_1 since this is directly proportional to a quantity of direct interest to the electronics design - the peak data handling rate.

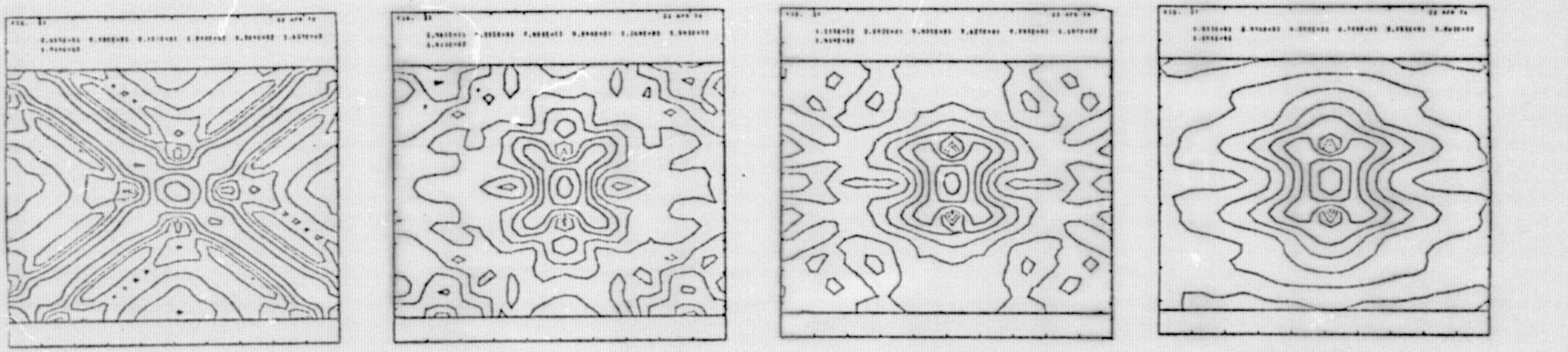

2 View $2\Delta_1 = 24$

4 View $2\Delta_1 = 24$

8 View $2\Delta_1 = 24$

24 View $2\Delta_1 = 24$

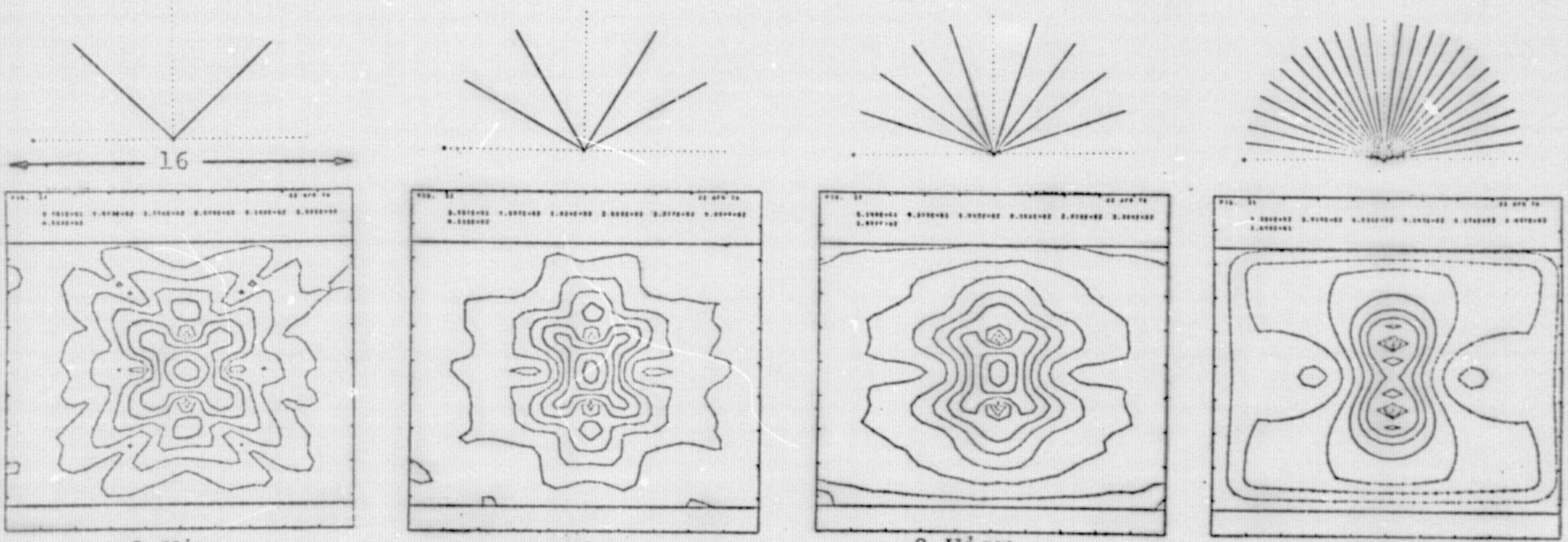

2 View $2\Delta_1 = 8$

4 View $2\Delta_1 = 8$

8 View $2\Delta_1 = 8$

Original Scene

Figure 21. Contour plots of image reconstructions for a vector field. Quantity plotted is the local magnitude of the velocity. (All Graphs S/N = 1, HI-PASS FILTER)

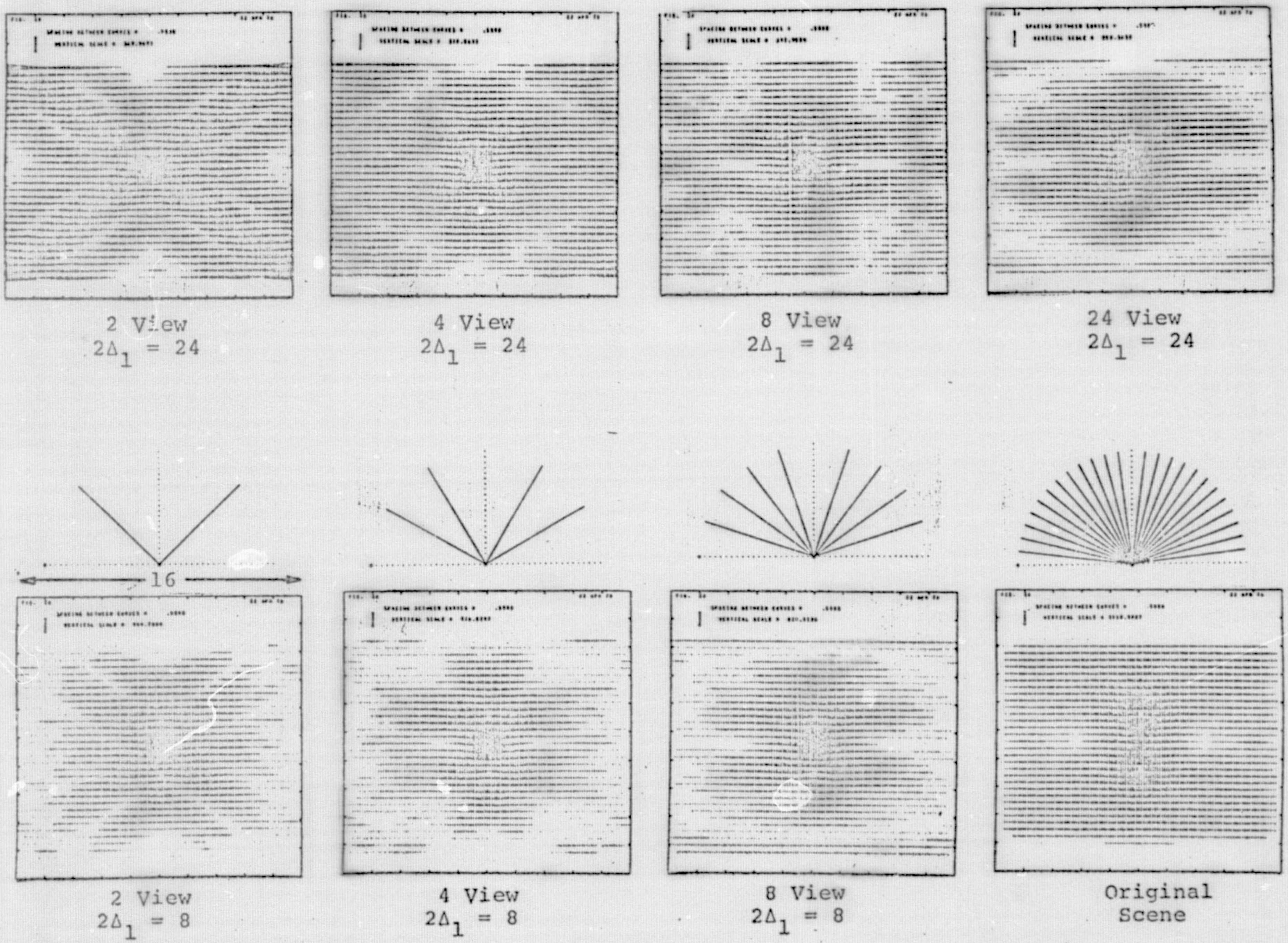

2 View
$2\Delta_1 = 24$

4 View
$2\Delta_1 = 24$

8 View
$2\Delta_1 = 24$

24 View
$2\Delta_1 = 24$

2 View
$2\Delta_1 = 8$

4 View
$2\Delta_1 = 8$

8 View
$2\Delta_1 = 8$

Original
Scene

Figure 22. Raster plots of image reconstructions for a vector field. Quantity plotted is the local magnitude of the velocity. (All Graphs S/N = 1, HI-PASS FILTER)

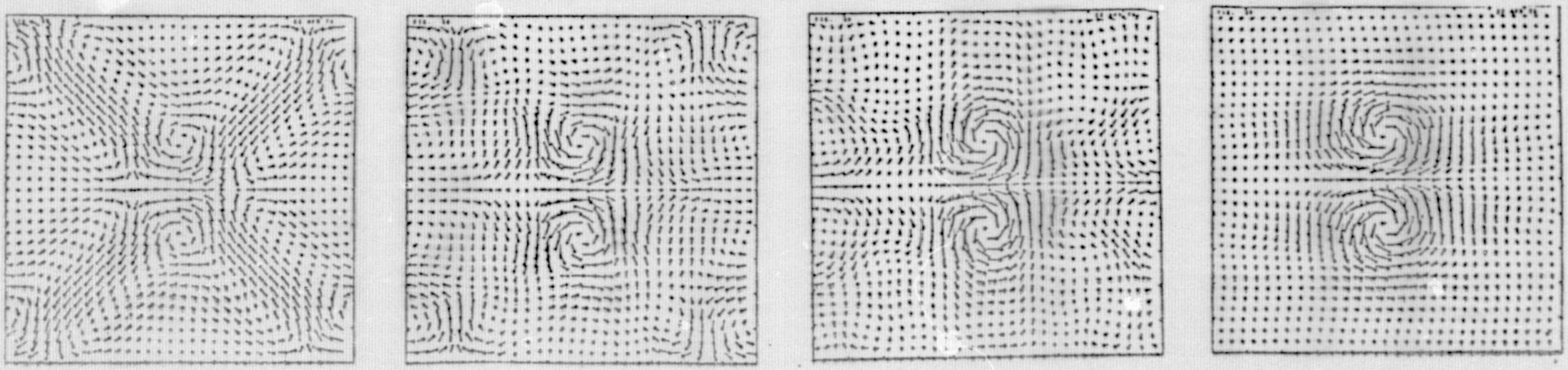

2 View $2\Delta_1 = 24$

4 View $2\Delta_1 = 24$

8 View $2\Delta_1 = 24$

24 View $2\Delta_1 = 24$

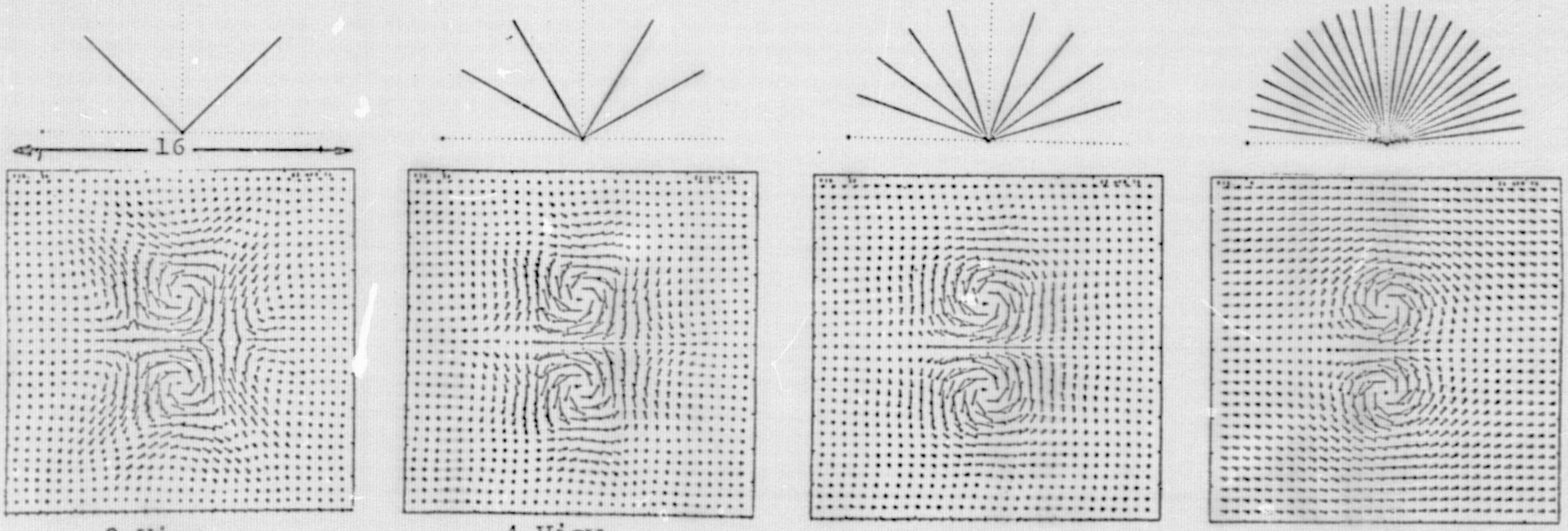

2 View $2\Delta_1 = 8$

4 View $2\Delta_1 = 8$

8 View $2\Delta_1 = 8$

Original Scene

Figure 23. Vector plots of the image reconstruction for a vector field. (All Graphs S/N = 1, HI-PASS FILTER)

The qualitative features of the images shown in Figures 16 to 23 appear generally consistent with the quantitative correlations shown in Figures 24 to 26. For the scalar mode the number of views must be increased roughly in proportion to an increase in resolution length to maintain the same image resolution. Of course, a saturation in this relation is reached when the reconstructed image is close to the original scene.

The vector field reconstructions (Figure 21, 22 and 23) are not as satisfactory as the scalar field reconstructions. The same general trends are evident, but substantially larger numbers of views appear to be required to fully resolve the vector image. It is felt that a more detailed analysis of the filtering and reconstruction process for the vector field will be required to develop an improved algorithm. Preliminary attempts to evaluate the efficacy of various filtering techniques to improve the image quality are discussed in the next section.

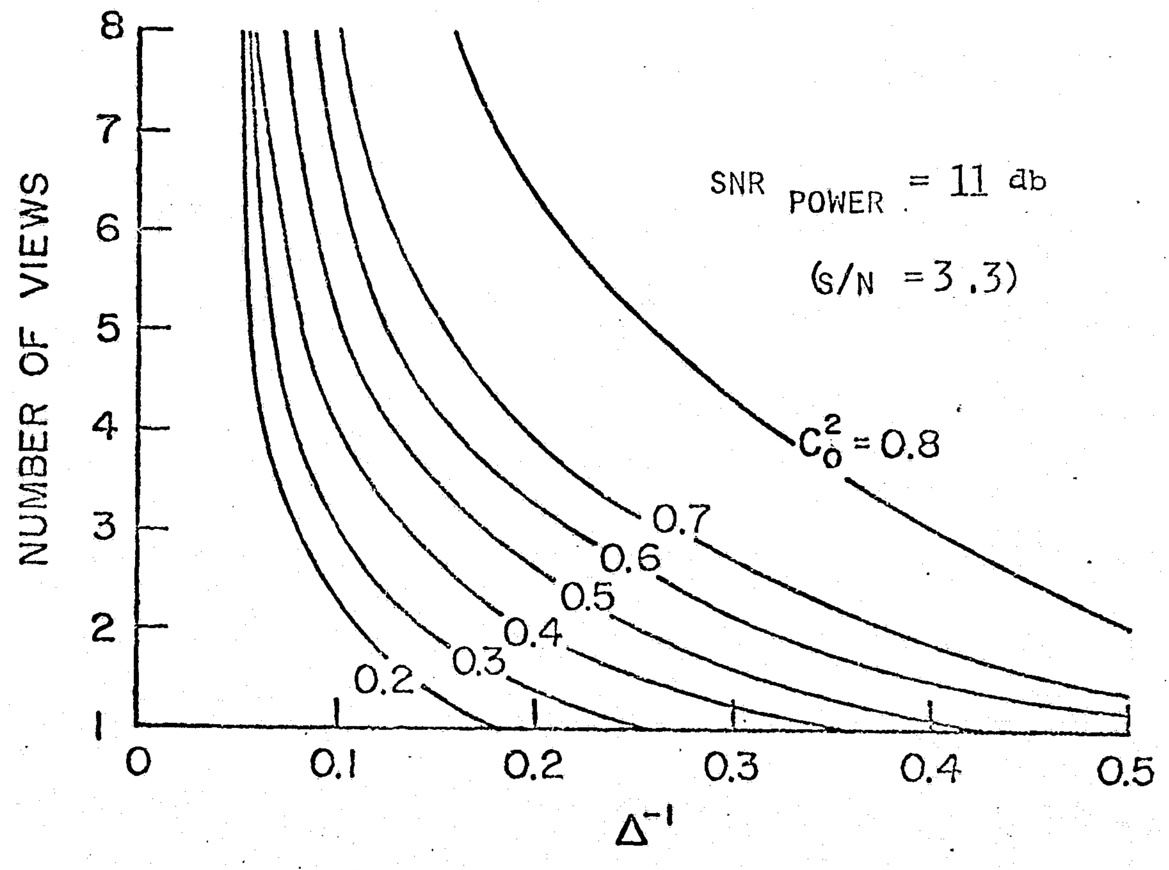

Figure 24 . Number of views required to maintain a given processed image resolution as a function of the single sensor range resolution (3 db resolution = 2Δ). The parameter C_o is the cross correlation between the processed scene and the actual scene. (Scalar Mode)

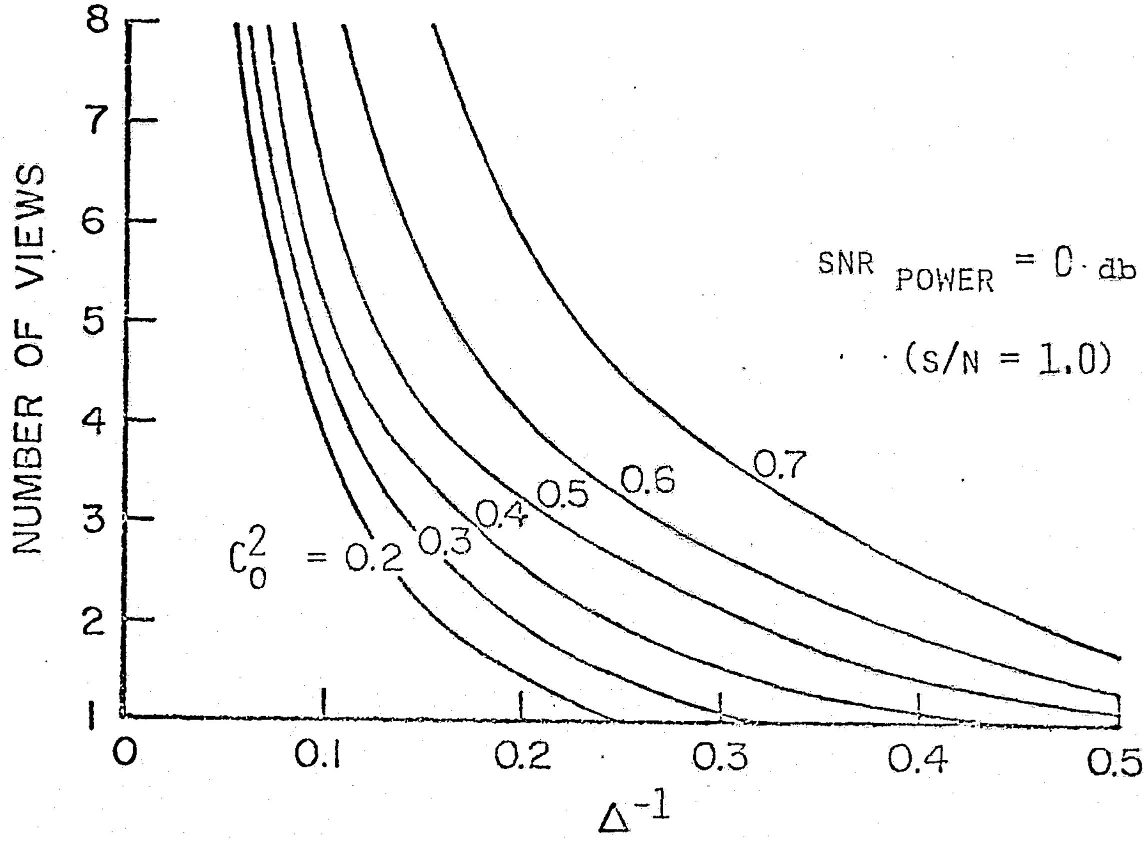

Figure 25. Number of views required to maintain a given processed image resolution as a function of the single sensor range resolution (3 db resolution = 2Δ). The parameter C_o is the cross correlation between the processed scene and the actual scene. (Scalar Mode)

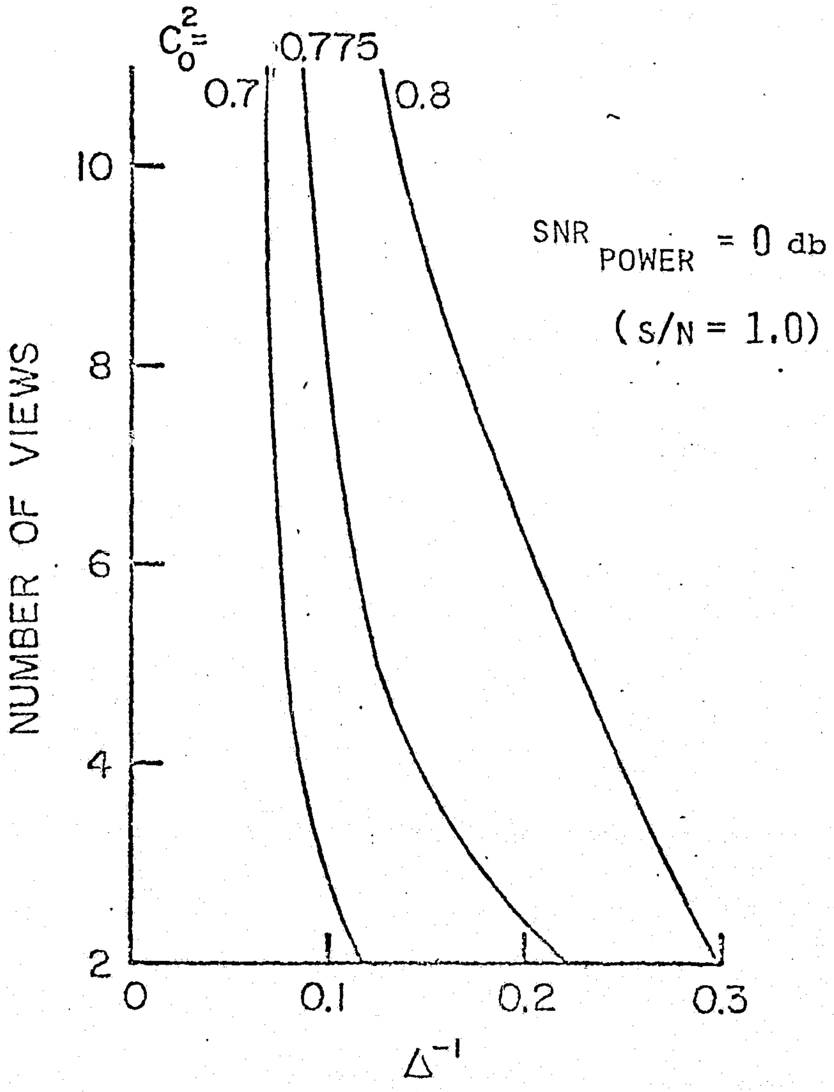

Figure 26. Number of views required to maintain a given processed image resolution as a function of the single sensor range resolution (3 db resolution = 2Δ). The parameter C_o is the cross correlation between the processed scene and the actual scene. (Vector Mode)

IV.3.3 Image Enhancement Procedures

The essential feature of the multiview process when the number of views is finite but at the same time the sensor resolution is poor is that the measurement incompletely samples the scene. In some directions detailed information is available but in others very little. In the Fourier (wavenumber; (k_x, k_y)) domain this means that data is given only along certain rays emanating from the origin ($k_x = k_y = 0$). A variety of methods for filling in or interpolating this data can be discussed and we will present one preliminary approach to this problem later in this section. First, however, we consider the proper choice of filters when the sampling is adequate. Simply adding together the independent views will not yield a perfect scene reconstruction. A point function ($\sigma(\vec{x}) = \delta(\vec{x})$) will yield an image $\sigma'(\vec{x})$ in this process which decays inversely as the radius ($\sigma' \sim 1/\sqrt{x^2+y^2}$).

A very simple filtering procedure has been used in Figs 27/29 to improve the image resolution of such data. This is basically a high pass filter. The final pictures are less smooth but the spurious wide wings associated with the multiview superposition are eliminated.

To investigate how well filtering procedures could improve the reconstruction of an incompletely sampled scene a single Gaussian source was examined (see Figure 30).

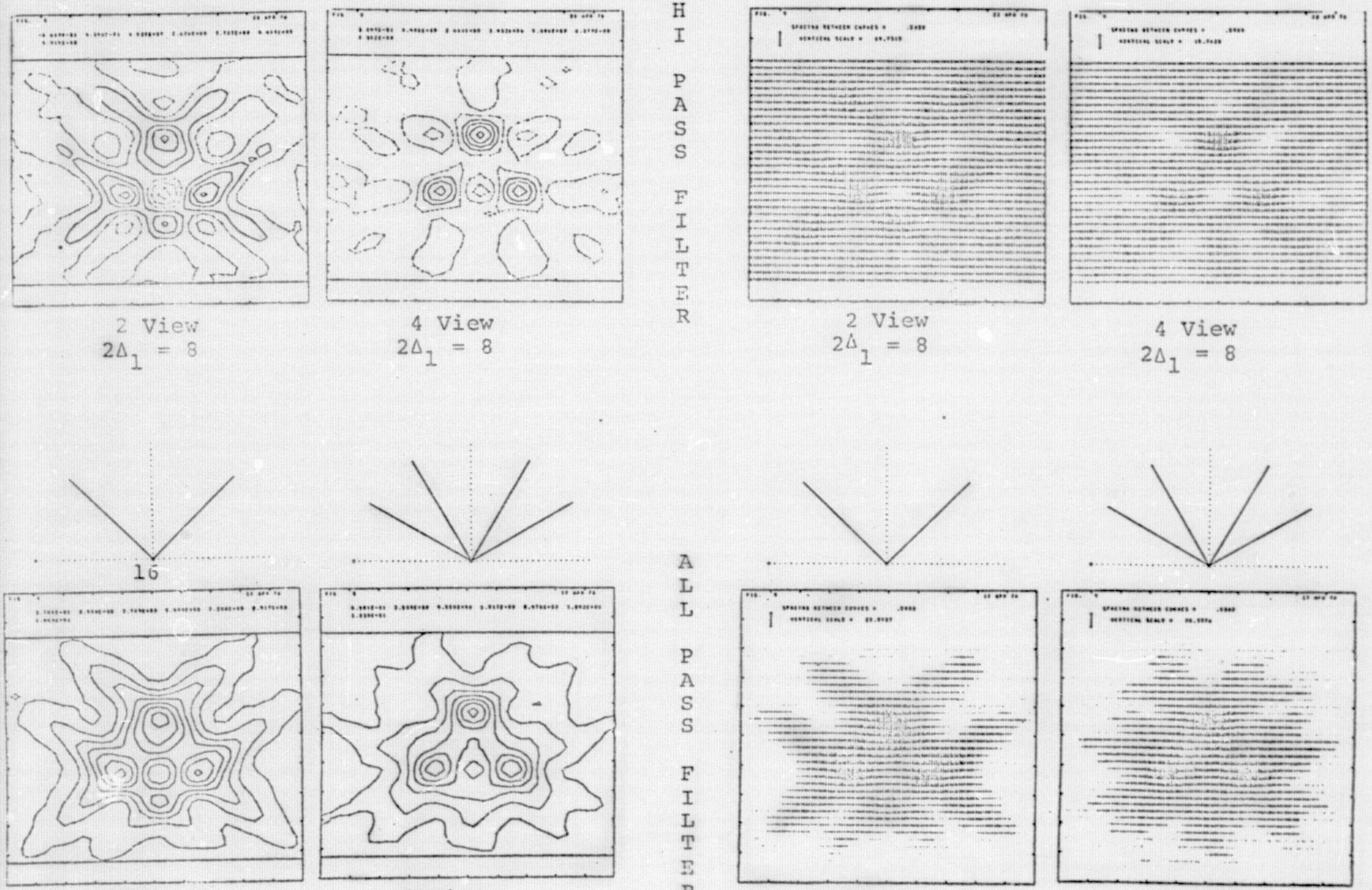

2 View $2\Delta_1 = 8$

4 View $2\Delta_1 = 8$

2 View $2\Delta_1 = 8$

4 View $2\Delta_1 = 8$

2 View $2\Delta_1 = 8$

4 View $2\Delta_1 = 8$

2 View $2\Delta_1 = 8$

4 View $2\Delta_1 = 8$

Figure 27. Effect of high pass filtering (scalar mode, all graphs N/S = 1). Note 3rd and 4th column graphs are Raster Plot representations of 1st and 2nd columns.

C2

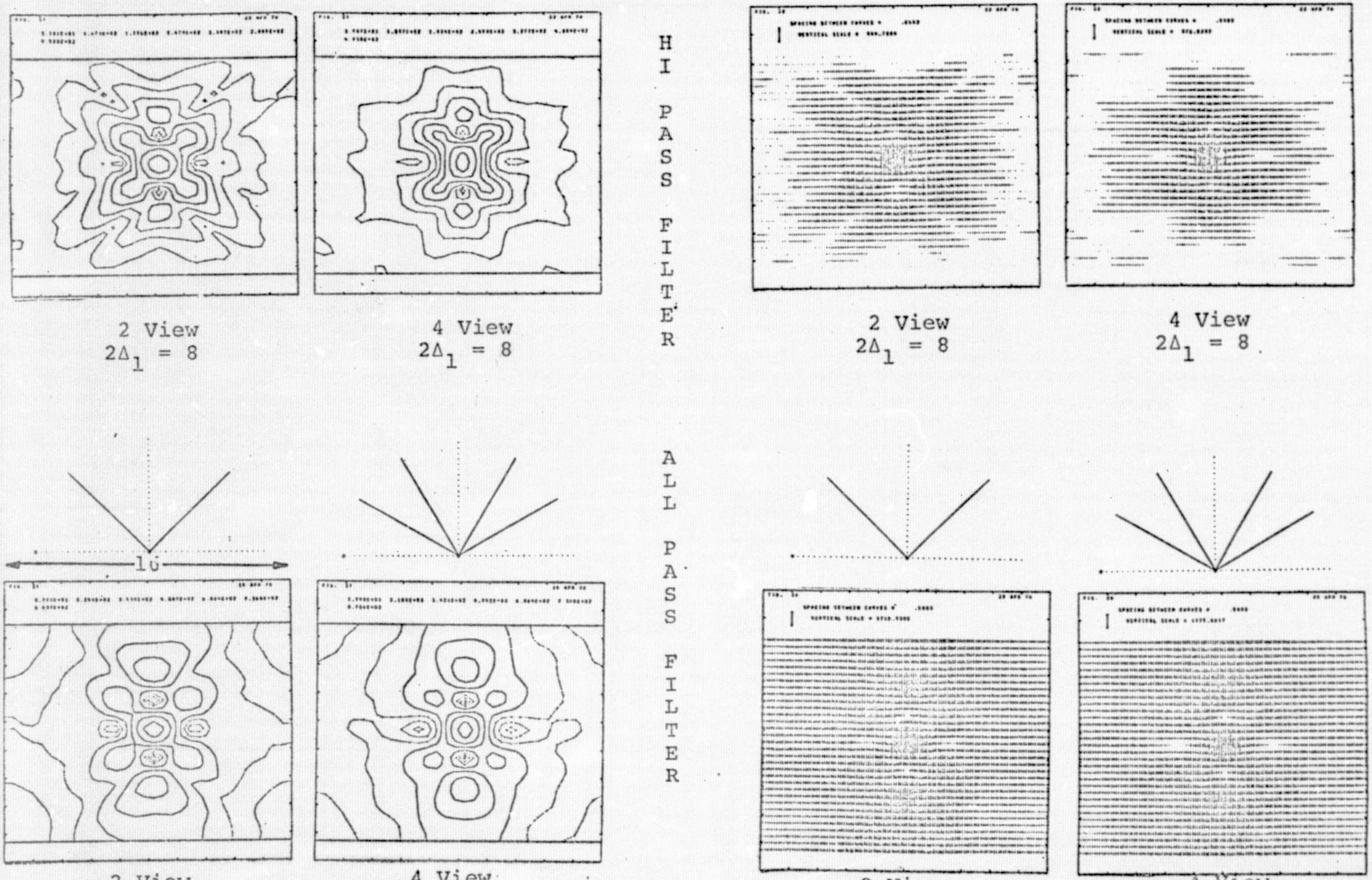

2 View $2\Delta_1 = 8$

4 View $2\Delta_1 = 8$

2 View $2\Delta_1 = 8$

4 View $2\Delta_1 = 8$

2 View $2\Delta_1 = 8$

4 View $2\Delta_1 = 8$

2 View $2\Delta_1 = 8$

4 View $2\Delta_1 = 8$

Figure 28. Effect of high pass filter (vector mode, speed distribution; all graphs N/S = 1) Note: 3rd and 4th column graphs are Raster plot representations of 1st and 2nd columns.

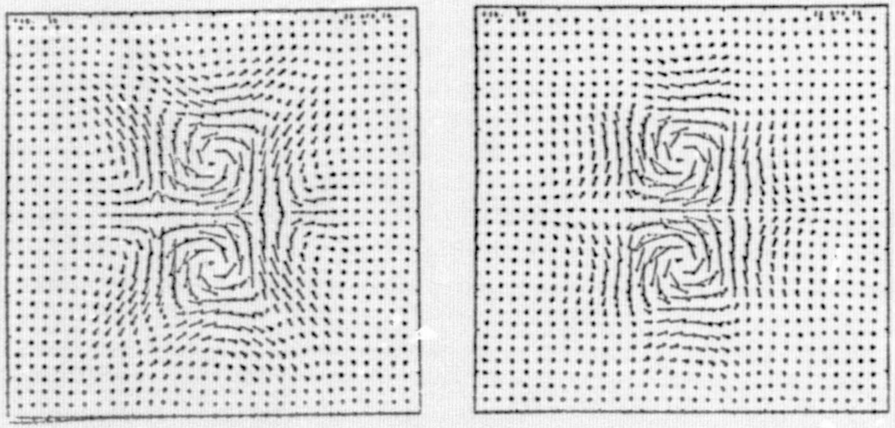

2 View
$2\Delta_1 = 8$

4 View
$2\Delta_1 = 8$

HI PASS FILTER

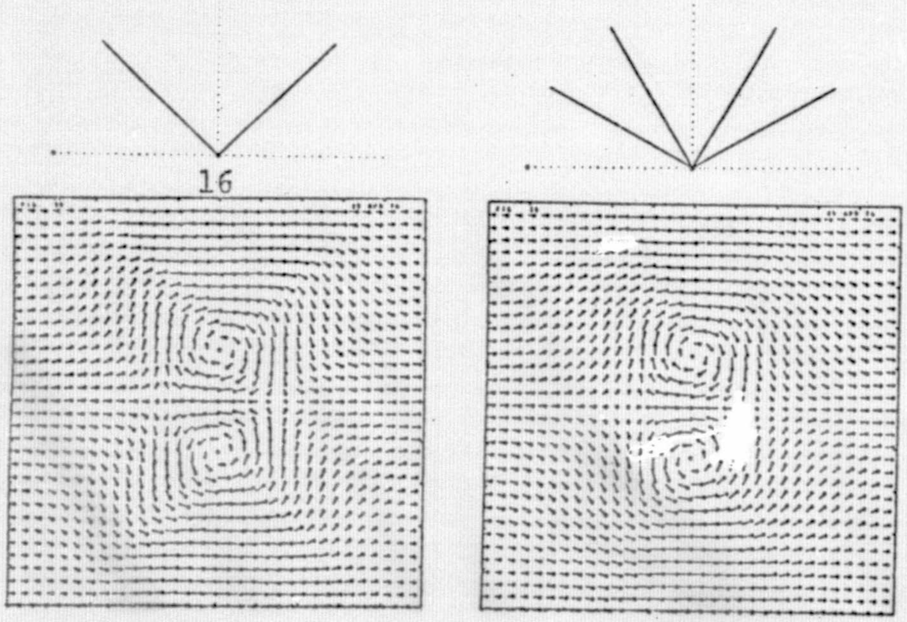

2 View
$2\Delta_1 = 8$

4 View
$2\Delta_1 = 8$

ALL PASS FILTER

Fig. 29. Effect of high pass filter (vector modes; all graphs N/S = 1).

An extreme case was taken with a full width instrument longitudinal resolution of $2\Delta_1 = 24$ units and two views. The instrument noise level was initially taken as zero (Fig 30a and 30b) and then taken as 14 db (Fig. 30c and 30d). The 2nd row of pictures shows the reconstructed scene after applying the matched filter. This would be the same situation as for all previous pictures (except with the addition of the application of the hi-pass filter).

The 3rd row of pictures shows the scene after a post processing (described below) and finally after a hi-pass filter was applied (4th row of pictures).

Essentially the post-processing procedure attempts to fill in regions in k-space away from viewing directions where the data is poorly represented or non-existent.

First the data in k-space (i.e. the actual data as measured from the instrument) is homomorphically filtered, (i.e. the log of the data is taken and the imaginary part (the phase of the original data) is smoothed. Each point in k-space is then weighted by the quantity $W(k_x,k_y) = \sum_{\text{views}} W_o$ where $W_o = \sum_{\text{views}} g_1^2(1 + N^2/S^2)/(g^2 + N^2/S^2)$ (see Eq. 20). This factor is a function of viewing angle, and correctly retains the integrity of the data along viewing directions. In addition to giving a unit weighting to directions near the viewing directions it assigns low weighting where the data strength is very low. The data is then averaged in the angular direction according to these weighting factors, i.e. unit weighted ('good') data are not changed, whereas data with low weight is interpolated from more highly weighted data. This has the effect of filling in data in poorly sampled regions from data in well sampled regions. This procedure works reasonably well for the single Gaussian case (Figure 30). The same procedure was applied to the standard three Gaussian source case. For the case considered of two viewing directions and $2\Delta_1 = 24$ it was found that the internal structure of the scene was not very well represented although the procedure did strongly localize the image structure and suppressed the spurious far distant contributions. (Figure 31)

Based on these preliminary results it appears that substantial image improvement can be achieved by the post processing procedures. However, the treatments reported here are not universally applicable to different scene types and more experimentation is needed.

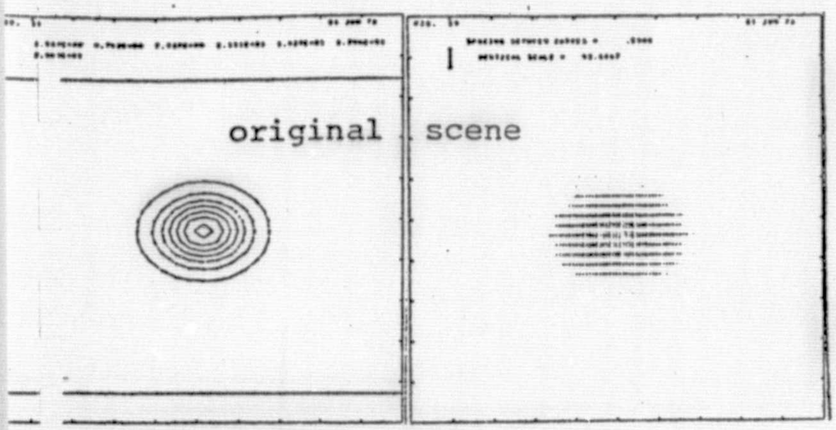

Figure 30. Effect of post-processing filters (scalar field, single Gaussian source.) All graphs are for 2 view, low sensor resolution ($2\Delta_1 = 24$), N/S of matched filter = 0.1. The 1st column has no instrumental noise whereas for the 3rd column (N/S) instrument = 0.04. The 2nd and 4th columns of raster plot are representations of the 1st and 3rd columns.

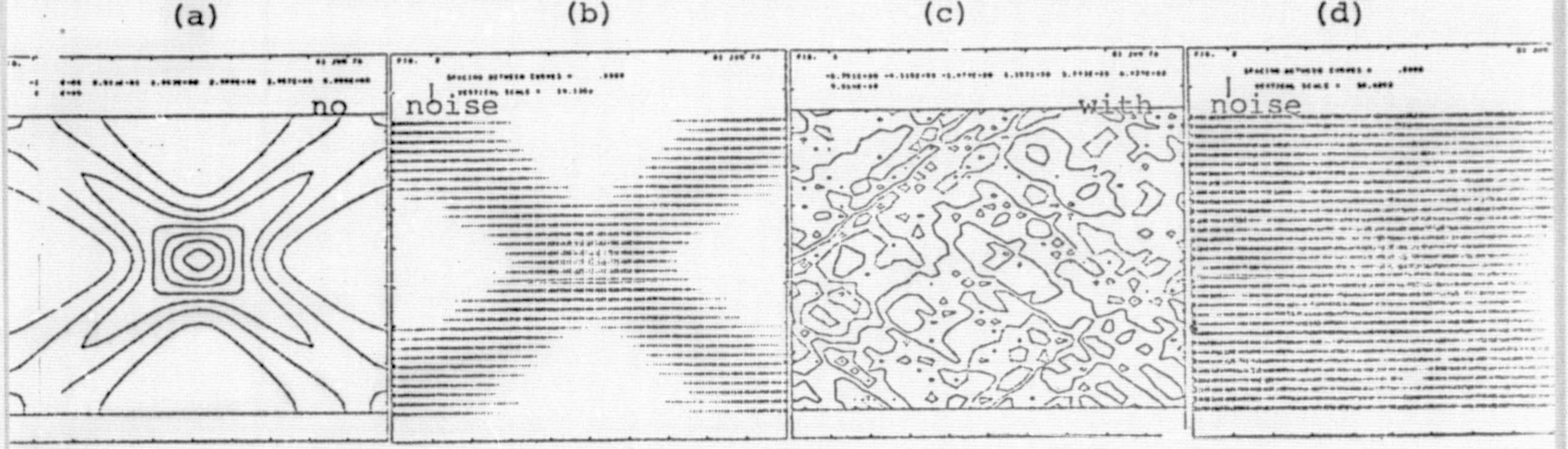

Reconstructions after applying matched filter

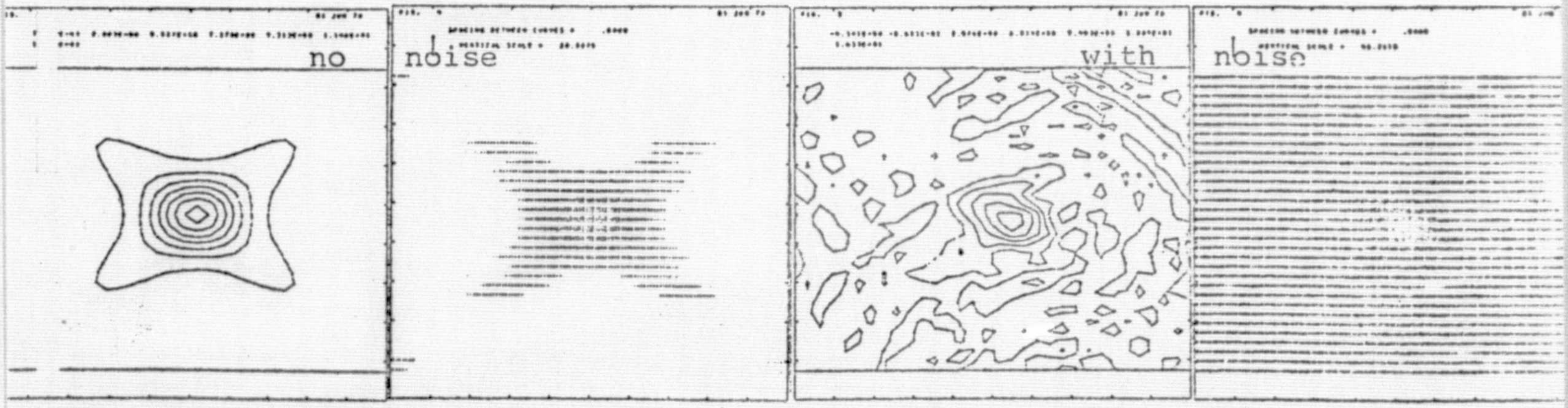

Reconstructions after post-processing

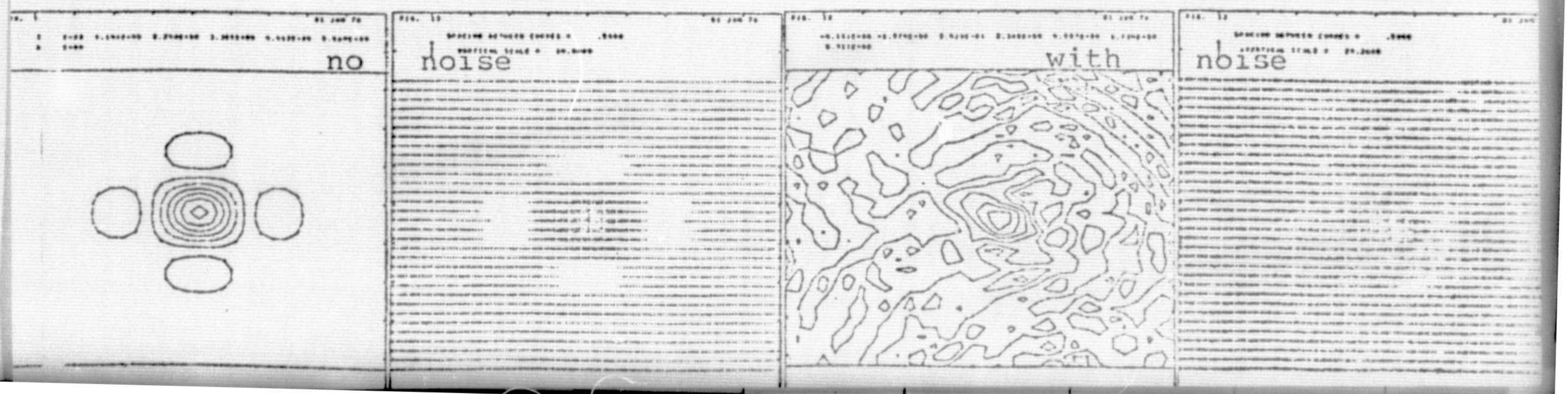

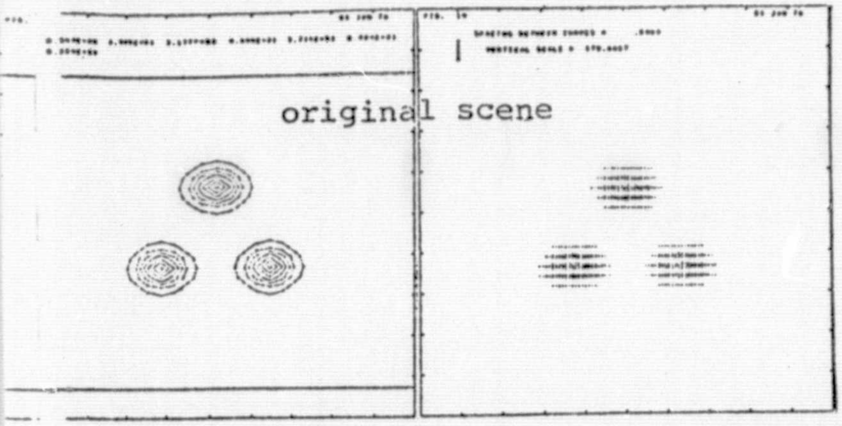

Figure 31. Effect of post-processing filters (scalar field, 3 Gaussian sources.) All graphs are for 2 view, low sensor resolution $(2\Delta_1 = 24)$, N/S of matched filter = 0.1. The 1st column has no instrumental noise whereas for the 3rd column (N/S) instrument = 0.04 The 2nd and 4th columns of raster plot are representations of the 1st and 3rd columns.

(a) (b) (c) (d)

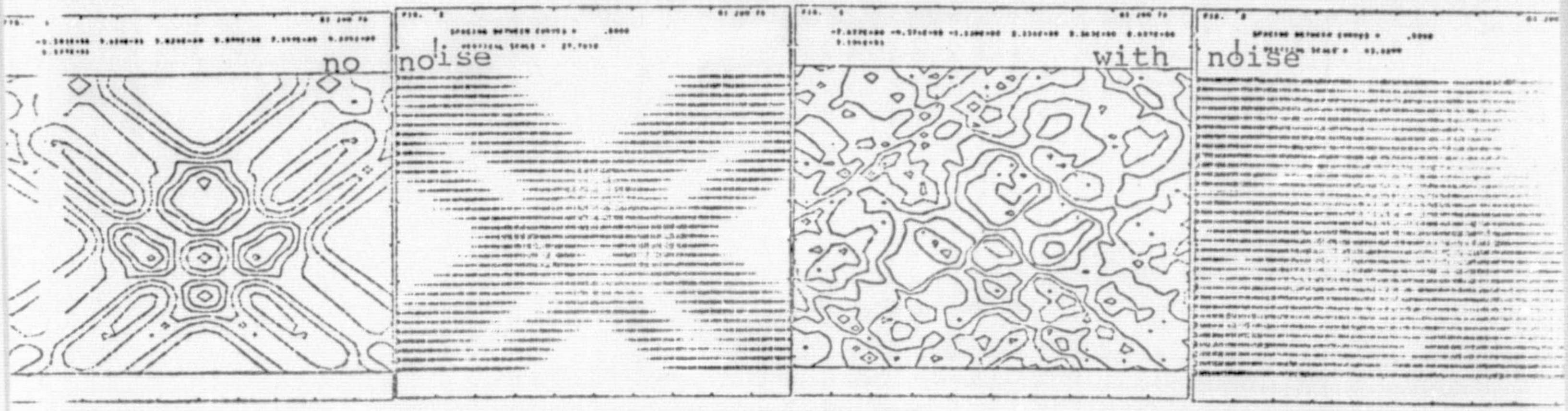

Reconstructions after applying matched filter

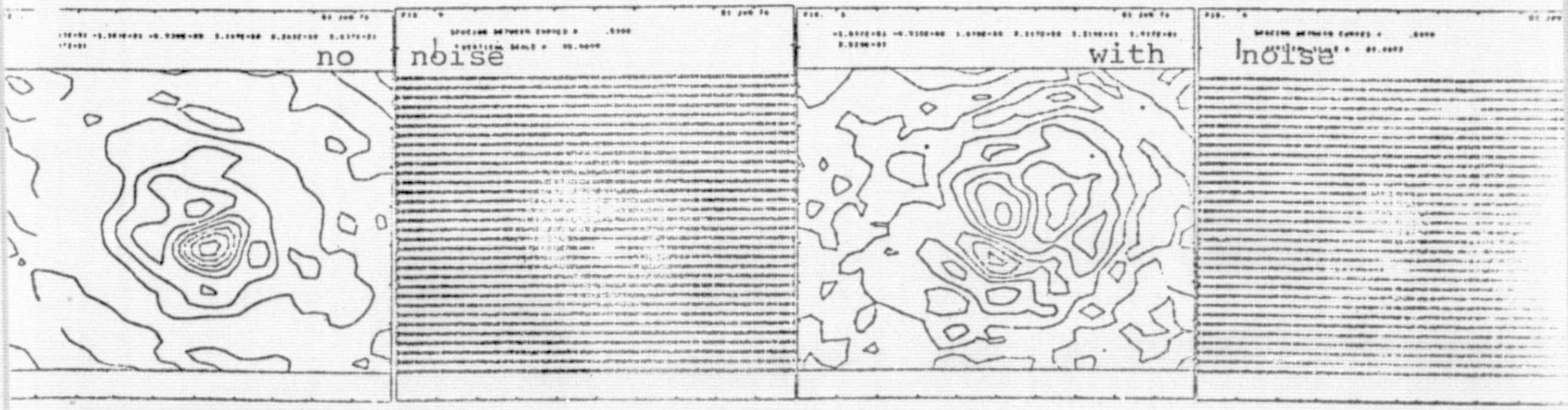

Reconstructions after post-processing

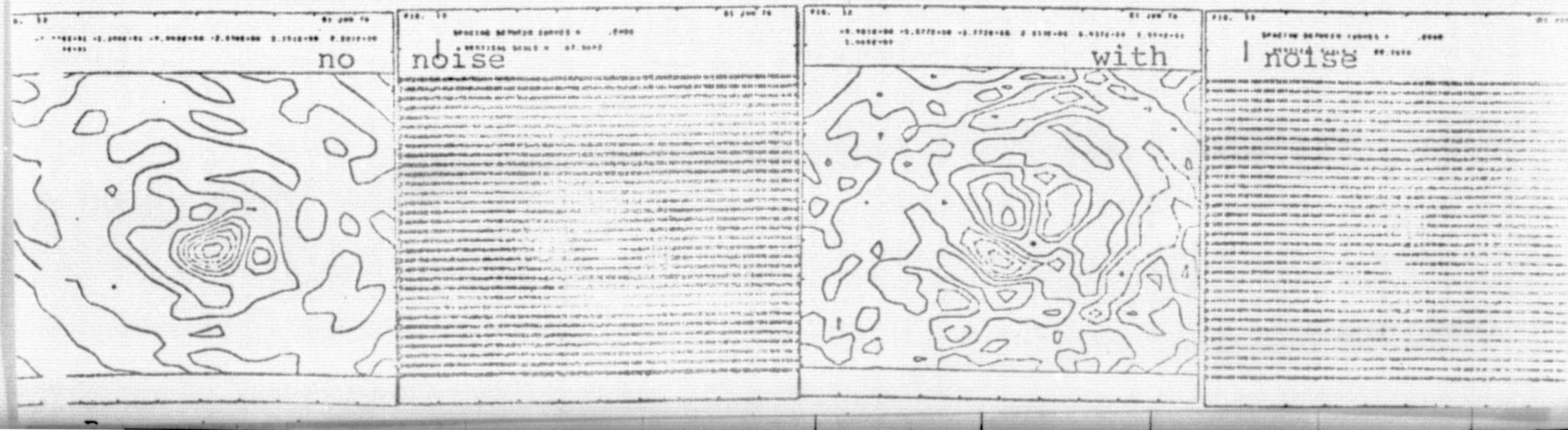

V. Conclusions and Recommendations

The essential conclusion of this study is that aircraft flight velocities are high enough and severe storm lifetimes are long enough that it is possible for a single airborne Doppler system, operating at a range of less than about 20 km, to view the storm area from two or more substantially different aspects before the storm characteristics change appreciably. This permits resolution of the spatial distribution of the velocity vector by a single coaxial system operating in a fly-by mode. In addition, it is suggested that, when the instrumental range resolution is poor, post-flight processing of such fly-by multi-view data can be carried out to materially improve the spatial resolution of the data.

When peak laser power levels and/or peak data handling rates are limiting problems (as is expected to be the case), substantial gains in signal-to-noise as well as velocity resolution are possible by implementing the multiview mode with strongly degraded single sensor resolution. Here the long pulse times permit a higher ratio of coherent to incoherent integration and a more accurate determination of velocity. The penalty required is that of a more complex optical scanning system as well as additional real-time or post-flight time data storage and processing.

Two essentially different scanning configurations have been identified, one a long-range (out to 10-20 km) roughly horizontal plane mode intended to allow probing of the velocity field around the storm at the higher altitudes (4-10 km). The other is a shorter range (out to 1-3 km) mode in which a vertical or horizontal plane is scanned for velocity (and possibly turbulence), and is intended for diagnostics of the lower altitude region below the storm and in the out-flow region. The first mode has a prototype form and an advanced form. In the prototype, only a single horizontal plane would be scanned for the u and v components of the horizontal velocity as well as certain combinations of their gradients (vorticity, convergence). In the advanced mode, multiple plane (simultaneous) capability is desired (10 or more stacked horizontal planes) and would be used to extract u, v, and w velocity information (and gradient) by processing the measured u and v data.

Application of the advanced mode may be primarily to complement the dual-Doppler radar measurements because of the limitations imposed by cloud attenuation as well as low-altitude attenuation. These may prevent the laser system by itself from acquiring all the data required in the full storm-related volume to permit reconstruction of the full velocity field.

It is recommended that detailed design consideration be given only to the short-range mode and the prototype long-range mode. Implementation of the advanced mode should be delayed until successful testing of the prototype mode is accomplished and/or additional analysis of the full 3D mode has been carried out.

Both the short-range and the long-range modes will require multiple-view capability; that is, scanning of the viewed area from two or more different aspect angles (within a possible range from 10° to 90°). These multiple views are required for two purposes: for extracting velocity vector data and for enhancing range resolution. A system that views each point in space from one direction only can only be used in conjunction with some assumptions such as horizontal uniformity of the wind field (as in VAD systems) and is not one of the permissible modes for this application.

Tradeoffs between number of views and range resolution exist. A degraded range resolution (due to a long pulse time) in the real-time data may be acceptable if a sufficient number of different views exist to allow post-flight processing for image reconstruction. Detailed plots of this tradeoff are given in Figure 24, 25, and 26. These data are derived from computer simulations and give the interdependence of number of views and sensor resolution that must obeyed in order to maintain a given processed image quality.

Under circumstances where pulse lengths are short enough to produce adequate range and velocity resolution without processing, only two views are required for the vector velocity field. However, it must be remembered that the vector fields are basically being differenced in the processing at least once and perhaps twice (once to get the components and again to get the vorticity and/or convergence). Thus high signal-to-noise levels are required as well as a finer grid.

Even for a many-view system the average output data rate (the data required to define the flow field that must be recorded per second) is relatively low (less than 100 data points per second). Without some real time processing, a 10 to 20 times higher recording rate may be required for the optimal multiview, continuous scan system. The advanced system will also require a 10-to-40-times higher rate. However, even here the total amount of data to be stored during a single measurement is expected to be less than 3×10^6 data. Thus the data storage is probably not severe. However, the peak data handling rate at the front end may for some designs be very high with a very low duty cycle. Thus it is recommended that serious consideration be given to modes in which the peak data handling rates are traded off against fairly extensive post-flight processing procedures.

Design Recommendations

It is suggested that aspects of the following problem areas be addressed in the design analysis.

(1) Registration and storm region transport. Combining multiple views requires that the data be recorded in a fixed spatial reference frame rather than just the a/c frame. Since different views are displaced in time, the relative displacement of the a/c to the storm needs to be accounted for in the recording of the data.

(2) Techniques for obtaining the zeroth, first, and second Doppler moments (backscatter level, mean velocity, and velocity spread) in each space-time resolution element from the Doppler spectra.

(3) Scanning techniques for obtaining 2, 3, 4 and/or many (10-30) aspect looks at the target region in a fly-by.

(4) Relation between peak front-end data handling rates and pulse duration and shape.

(5) Tradeoff between pulse duration and number of views (i.e., between peak front-end data handling rates and multi-view scanning techniques).

(6) Real-time partial processing and display for purpose of data quality monitoring...and reduction of data storage.

Appendix I

MATCHED FILTER PROCESSING - AN EXAMPLE

In order to demonstrate the nature of the matched filter process, we consider the detection and processing of the signal resulting from the illumination of a point scatterer. For convenience we treat only the one-dimensional problem.

The scatterer is located at the point $x = x_o$ and is described by the distribution function

$$\sigma(x) = \sigma_o \delta(x-x_o) \quad . \tag{1}$$

For this example we choose a Gaussian shape for the instrument response function:

$$G(u) = \exp(-u^2/\Delta^2)/(\sqrt{\pi}\Delta) \quad . \tag{2}$$

The detected signal is

$$S(x) = \int \sigma(x') \ G(x-x')dx' + \text{noise} \tag{3}$$

and its Fourier transform is

$$s(k) = \sigma(k) \ g(k) + n(k) \quad . \tag{4}$$

For reference we note that the transform of the original scattering function is

$$\sigma(k) = \sigma_o \exp(ikx_o) \tag{5}$$

and that of the instrument response function is

$$g(k) = \exp(-k^2\Delta^2/4). \qquad (6)$$

In the total absence of noise, the signal may be processed by a deconvolution filter to yield the original scatterer distribution:

$$\sigma'(k) = \frac{1}{g(k)}\left[s(k)\right] = \sigma(k) = \sigma_o e^{ikx_o} \qquad (7)$$

In the presence of finite noise however, this deconvolved signal becomes

$$\sigma'(k) = \sigma(k) + n(k)/g(k) \qquad (8)$$

In regions where $g(k)$ is small ($k >> 1/\Delta$) the noise is greatly amplified and can effectively destroy the imaging process. Here an appropriate matched filter should be used. For optimal processing in the presence of white noise, the deconvolution filter $(g(k))^{-1}$ should be multiplied by a weighting factor $w(k)$ given by

$$w(k) = \frac{|g|^2(1+(N/S)^2)}{(N/S)^2 + |g|^2} \qquad (9)$$

where S/N is the expected signal/noise ratio.

Thus the processed signal is

$$\sigma'(k) = \frac{s(k)g^*(k)(1+(N/S)^2)}{|g|^2 + (N/S)^2} \qquad (10)$$

and the noise is

$$n'(k) = \frac{n(k)\,g^*(k)\,(1 + (N/S)^2)}{|g|^2 + (N/S)^2} \tag{11}$$

For our point scatterer example this signal has the explicit form

$$\sigma'(k) = \sigma_o e^{ikx_o} \frac{(1 + (N/S)^2)}{1 + (N/S)^2 \exp(k^2\Delta^2/2))} \tag{12}$$

In x-space this processed signal has the form

$$\sigma'(x) = \sigma_o \int \frac{e^{ik(x-x_o)}\,(1 + (N/S)^2)\,dk}{\left[1 + (N/S)^2 \exp(k^2\Delta^2/2)\right]} \tag{13}$$

For high signal-noise ratios (N/S << 1) an approximate evaluation of this integral can be obtained by setting the denominator equal to 1 for $|k\Delta| < \sqrt{\ln\,(S/N)}$ and to infinity otherwise. In this approximation

$$\sigma'(x) = \frac{4\sigma_o}{\Delta} \frac{\sin\left(\frac{\pi}{2}\,\frac{x-x_o}{\Delta^*}\right)}{\frac{\pi}{2}\left(\frac{x-x_o}{\Delta^*}\right)} \tag{14}$$

where

$$\Delta^* = \frac{\pi}{4}\,\frac{\Delta}{\sqrt{\ln\,(S/N)}}$$

Thus the width of the processed image is reduced from the instrumental width by the factor

$$\frac{\Delta^*}{\Delta} = \frac{\pi}{4\sqrt{\ell n\ (S/N)}} \tag{15}$$

The extent of the image improvement that can be achieved at high signal/noise ratios depends explicity on the shape of the instrument function. For example, a box function of the form:

$$G(u) = 1 \text{ for } |u| \le \Delta \tag{16}$$

$$= 0 \quad \text{otherwise}$$

has a reconstructed image of the form

$$\sigma'(x) = \sigma_o \int \frac{e^{ik(x-x_o)} (1 + (N/S)^2 dk}{1 + (N/S)^2 \left(\frac{k\Delta}{\sin k\Delta}\right)^2} \tag{17}$$

An approximate estimate of this integral (as before) leads to a simple but different dependence of the processed image width on the (voltage) signal to noise ratio:

$$\frac{\Delta^*}{\Delta} \approx \pi/(\sqrt{2}\ (S/N)) = \pi/\sqrt{2(S/N)_{\text{power}}} \tag{18}$$

This box shaped resolution function exhibits a much greater reduction in image width at high S/N values than does the Gaussian form. This results from the sharp cutoff at the edge of the resolution function and the resulting relatively rich wavenumber spectrum.

In Figure 32 we show numerical calculations of Eq. 13 for the expected profile of the matched filter processed signal for various values of signal to noise using the Gaussian response function (Eq. 6). The figure shows the rapid narrowing of the resolution function as S/N is increased at low S/N values changing to a much slower dependence at high S/N as would be expected from the logarithmic dependence given in Eq. 18. These profiles are the 'expected values' for the signature. Any given measurement with finite noise will appear more irregular. In general, use of matched filters whose S/N values are less than those of the actual signal leads to smooth looking output with a clearly defined but relatively broad profile. However, the optimum matched filter (for which the value of S/N in the filter is matched to that of the data) always provides the best localization of the source.

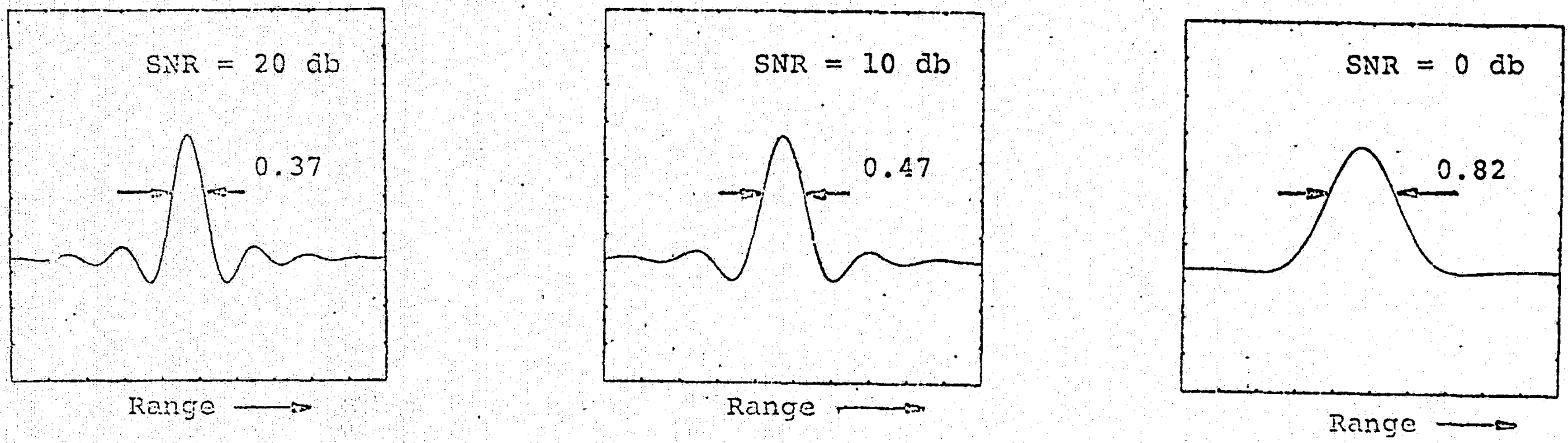

Figure 32. Matched filter reconstructions of the profile of a point target at different signal to noise ratios. The sensor is assumed to have a Gaussian response function in range. The 3 db resolution widths (relative to the width expected in the small signal limit) are indicated.

APPENDIX II

CLASSIFICATION AND DESCRIPTION OF WIND FIELD CHARACTERISTICS OF SEVERE LOCAL STORMS

I. INTRODUCTION AND SUMMARY

One could classify severe storms according to the overall size of the phenomena which produce severe effects into severe local storms (thunderstorms or tornados) and into severe extended storms (hurricanes or high pressure-gradient storms). However, in the following the notion of severe local storm is applied to dangerous and damaging phenomena occurring in all of these storms because the severe features of such storms are usually well localized in space and time. Actually, the notion of a severe local storm has a restrictive meaning for the meteorologist and weather forecaster: "...when lightning strikes practically continuously within and between the clouds of a hugh thunderstorm..." (ref.1) or, more definitively, a so-called "supercell thunderstorm" which, by definition, produces hailstones of the size of tennis balls in temperate latitudes (p. 159, ref. 2). Dangerous situations connected with the motion of air around and in storms are caused primarily by relatively sudden and large changes in the velocity and in the direction of local wind features. Such changes may be related to: (a) strong down-drafts and up-drafts around and in thunderstorms or in large gusts, (b) excessive wind shears from strong gusts in pressure-gradient storms, from tornados, and from cold outflows of thunderstorms, and (c) obstacles in the path of strong winds. In this Appendix, synopses are for the categories of storms and of features around and in storms which produce such phenomena. A measurement system must be designed to conform to the space-time velocity structure of these storms. An overall summary of these dimensions is given in the following section. This summary is based on a more in depth discussion that follows.

I.1 Overview of the Space-Time Velocity structure of severe local storms

210 Thunderstorms (air-mass, single-cell)

211 Depression, trough and orographic thunderstorms

life cycle: 1/2 - 3 hrs.

cell-size: length: 15 - 50 km

width: 5 - 15 km

height: up to 12,000 m from 400-500m above ground

approach speed: 15-60 km/hr (stationary at mountain crests)

severe gusts: 15-25 m/sec: cold-outflow, roll-cloud

gusts: 5-10 m/sec increasing up to 8-10,000 m

severe updrafts: 5-20 m/sec forward cloud portion

severe downdrafts: 10-40 m/sec backward lower cloud position

strongest shifts: near ground at front (up to 180°); throughout storm, might veer up to 90° immediately after storm

strongest winds: 20-40 m/sec at 300 to 500 m near hail area; can double at mountain crests.

212. Multi-cell and area thunderstorms

life cycle: 1-5 hrs.

cell-size: height: 50-150 km

width: 100-300 km

approach speed: 15-60 km/hr (stationary at
mountain crests)

severe gusts: 30-60 m/sec and largest in major cold.
outflows, particularly when supported
by down slopes; at front-base and
lower front of roll clouds.

severe updrafts: 10-25 m/sec in forward cloud portions

severe downdrafts: 15-50 m/sec in backward lower
cloud portions, enhanced by down
slopes.

strongest shifts: same as under 211.

strongest winds: 25-50 m/sec in cold outflows

213. Supercell thunderstorms

life cycle: 1-10 hrs.

cell size: length: 50-150 km
width: 20-50 hrs

approach speed: same as under 211

other features: same as under 211.

214. Thunderstorm squall lines (prefrontal)

life cycle: 1 -10 hrs

cell size: length: 20-60 km (in direction of motion)
width: 250-500 km (length of band)

approach speed: 15-60 km/hr

severe gusts: 20-30 m/sec at front of cold-air
outflows under leading edge (roll cloud)

severe updrafts and downdrafts: similar as or more intensive than 211.

shifts and strongest winds: similar as or more intensive than 211.

22. Tornadoes

typical structure: interconnect clouds and ground; electrical discharge.

path-length: 0.5-15 km (150 to 500 km on rare occasions)

path-width: 10-300 m (0.5 to 10 km on rare occasions)

approach speed: 15-30 km/hr (50 to 80 km/hr on rare occasions)

wind speed: 20-70 m/sec (100 to 200 m/sec on rare occasions)

updrafts: suction vortices 30 to 100 m/sec

persistance: 20 to 50 min in families

recurrence: 30 to 60 min intervals

23. Funnel Clouds (cold air)

no tornado potential

typical structure (connected to clouds, may not touch ground)

path-length: 1-4 km (up to 10 km on rare occasions) path-width: 1-5 m (up to 20 m on rare occasions)

approach speed: 15-50 km/hr

wind speeds: not really known; ≈ 2-10 m/sec

persistence: 3-10 min (15-20 mins on rare occasions)

24. Dust devils

typical structure (rising from the ground; no discharge)

path-length: 0-5 km (up to 10 km on rare occasions)

path-width: 10-100 m (up to 500 m on rare occasions)

heights: 30-200 m (up to 1000 m on rare occasions with disturbances to 2000 m)

approach speed: 0-20 km/hr (move with average wind if ≥ 5 km/hr)

wind speeds: not really known; ≈ 5-30 m/sec (up to 50-100 m/sec on very rare occasions)

updrafts: not really known; ≈ 10-50 m/sec (up to 100 m/sec on rare occasions)

persistence: 2 to 5 min (30 mins to 4 hrs on rare occasions)

25. Density current vortices

251. Powder snow avalanches

bulk-flow velocity: 30-100 m/sec

vortex-flow velocity: ~ 2 x bulk velocity (up to 200 m/sec)

vortex duration: 2-3 sec for each cell

vortex cell size: ~ 0.5-30 m (estimate)

252. Nuée ardente

bulk-flow velocity: 3-10 m/sec

vortex-flow: 70-100 m/sec

vortex-flow duration: not really known (~1-20 sec estimate)

vortex cell size: not really known (0.5-30 m estimate)

structure: many short (0.5-30 metres minimum) horizontal vortex cylinders.

253. Sand and dust storms (haboob)

bulk-flow velocity: 5-20 m/sec (and larger on occasion)

vortex-flow velocity: 20-100 m/sec (and larger on occasion)

vortex-flow duration: not really known (~5 to 60 min estimate for tornado-like structures)

vortex cell-size: 10-300 m (and larger on occasion)

254. Typical vortex structures in density currents

2541. Surge heads

2542. Rising tunnels

2543 Vortex pairs

2544 Vortices from clouds

3. Typical strong wind shifts and gusts

$$V_{gust} \simeq (1.44 \pm 0.11)\, V_{wind} \begin{cases} \text{horizontal} \\ \text{vertical: above} \sim 30 \text{ m} \end{cases}$$

persistance: (horizontal) 1/2-30 sec

(vertical) ~ 1/3 x (horizontal)

distance for increase to maximum velocity: 15-70 m

wind shears $1/10 - 3\ \text{sec}^{-1}$

directional drifts: 15-30° near ground

(up to 160° observed under roll-clouds)

31. Wavestreaming and rotor streaming

shifts: 45-160° particularly under rotor clouds

velocity of gusts: depends on average wind (see above under 3).

severe downdrafts: below and near front of roll clouds and near lee of obstructions

32. Turbulence in the lee of mountains

(qualitative features)

33. Circulation gust cells

wind shifts (northern hemisphere): veered with increase, backed with lull, 15-30° (up to 45° on rare occasions) cell size: 100-2000 m for small to medium size eddies

persistence: 5-50 sec

extension: up to 1000-2000 m

2. TYPICAL SEVERE LOCAL DENSITY STORMS

Under this heading, phenomena are combined which occur primarily in conjunction with instabilities caused by the mixing of air-masses with different temperatures, densities and moisture contents. Thus, thunderstorms and their associated features, including tornados and funnel clouds, are considered; but also dust-devils, water spouts, airborne avalanches of powder snow and of volcanic materials (nueés ardentes), and sand and dust storms (haboobs) belong here. Cold winds down large mountain slopes (katabatic winds), like cold foens, cold Santa Anas, or boras, cause similar effects as cold air outflows from large area thunderstorms and are included under vortex-generating density flows. Warm katabatic winds (warm foens or warm Santa Anas) are not incorporated here since their turbulent features (associated primarily with mixing of upper-level, high-velocity winds with ground-level air masses) are usually caused by topographic obstructions.

2.1. Thunderstorms (Air-Mass, Single-Cell)(2-7)

Air-mass thunderstorms (single cell variety) will be ignored. They grow among other large cumulus and cumulonimbus in very unstable airstreams (thermals) and are usually not severe.

2.1.1. Depression, Trough, and Orographic Thunderstorms(2-7)

Occurrence: Areas of depressions and troughs where usually strong tendencies for ascent of moist air masses exist. Ascent of warm and unstable moist air masses at mountains can lead to (orographic) thunderstorms. Outbreaks are widespread (especially in summer). One storm cell tends to build another on the back of the very cold air which cascades out of the parent storm and spreads around it. Groups of cell form, each new cell taking over where a previous cell dies out. The chains of cells can coalesce into area storms which may cover areas of 15 to 30 km across and can result in thunderstorm highs.

Typical Cell Structure: (See Figs. 2.1a and 2.1b.)

length: 15 - 50 km

width: 5 - 15 km

life cycle: ∿ 1/2 - 3 hrs

speed of approach: 15 - 60 km/hr; center often stationary near mountain crests.

severe gusts: 15 - 25 m/sec at the front of cold-air outflow and near the base in front of the cloud: roll cloud.

severe updrafts: severeness of gusts increases to 5-10 m/sec with altitudes up to 8 - 10,000 m. 5 - 20 m/sec in forward cloud portion.

severe downdraft: 10 - 40 m/sec in backward lower cloud portion (hail area).

strongest wind shifts: At and near ground at front of cold outflow veered by almost 180°. Wind veers throughout storm; sometimes up to 90° to direction of approach immediately after storm passage.

strongest winds: 20 - 40 m/sec flowing out from and near hail area at altitudes from 300 to 500 m. Wind velocities can double above mountain crests.

Special Features: Sudden outbreaks of large thunderstorm areas can result in thunderstorm highs due to replacement of warm air by cold air. These highs may set up pressure surges causing sharp and large directional wind changes (often backing up to 180°), as well as violent gusts from 2 to 15 m/sec many miles away. The location of these changes depends on the movement of the pressure surges (at and near ground level) from the thunderstorm high. Cold outflows may affect areas up to 100 km away from large thunderstorm areas (precipitation downdrafts), particularly if mountain terrain supports the descent of the cold masses.

For a model of hail-producing thunderstorm, see Figure 2.2.

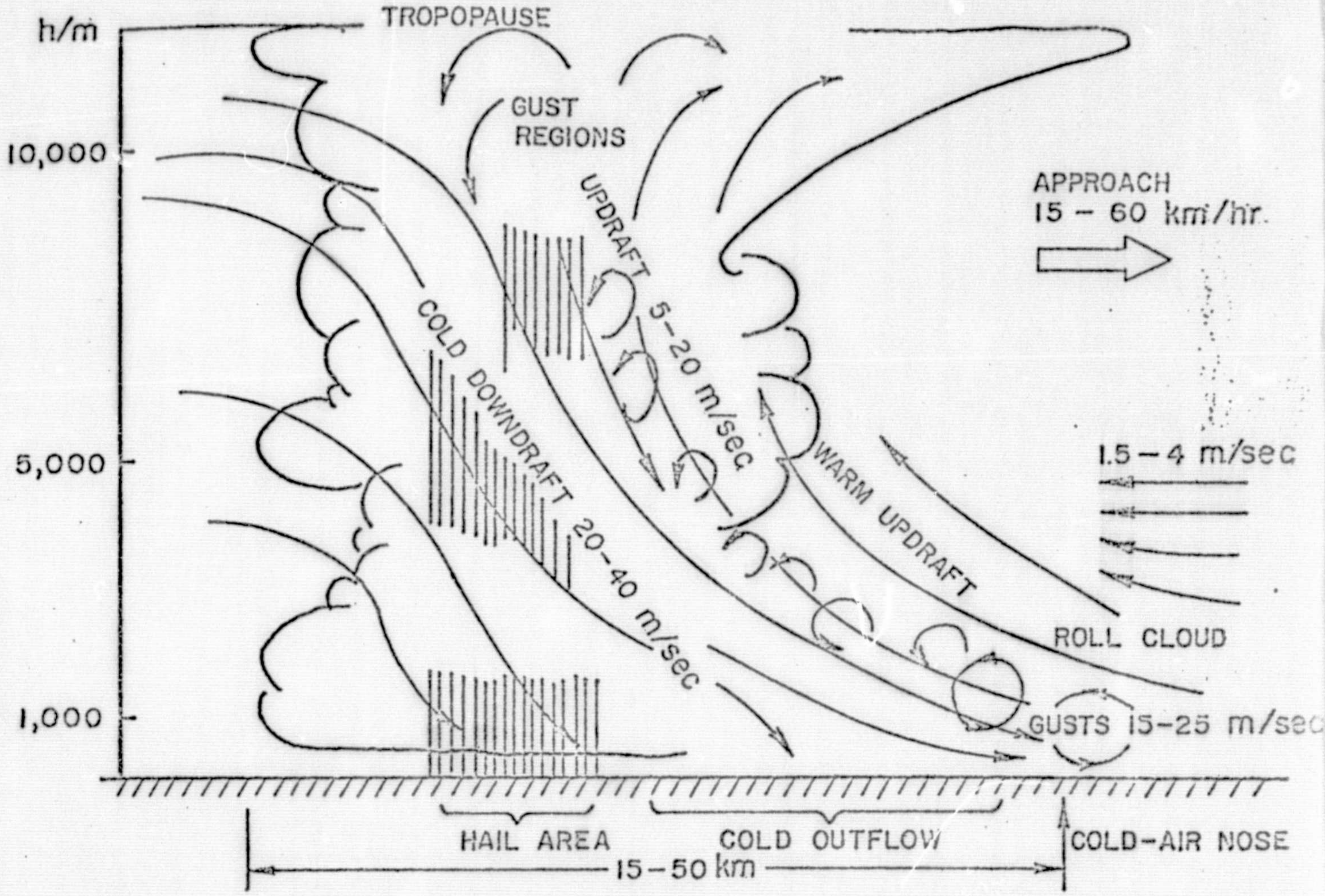

Figure 2.1a. Typical Thunderstorm Cell Moving from Left to Right (side view).

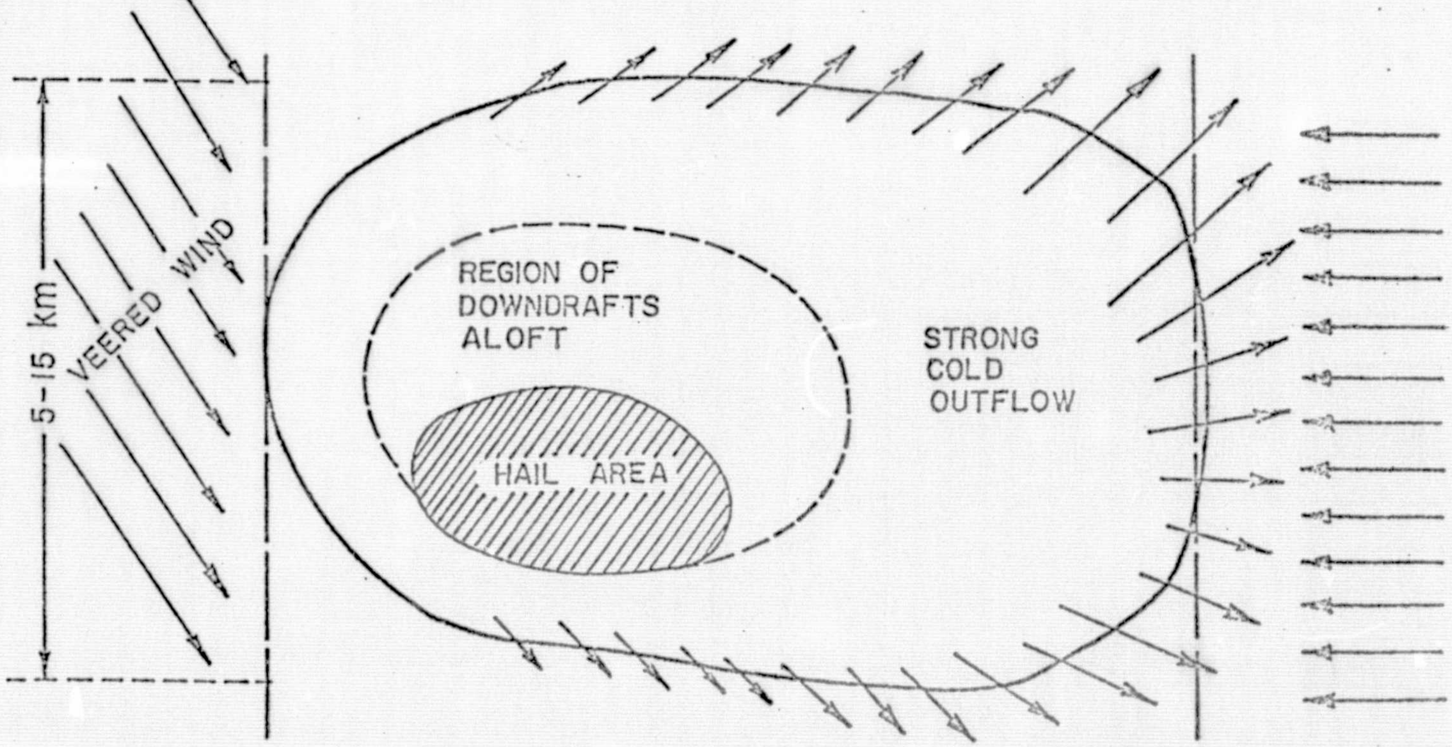

Figure 2.1b. Typical Thunderstorm Cell Moving from left to Right (top view near ground).

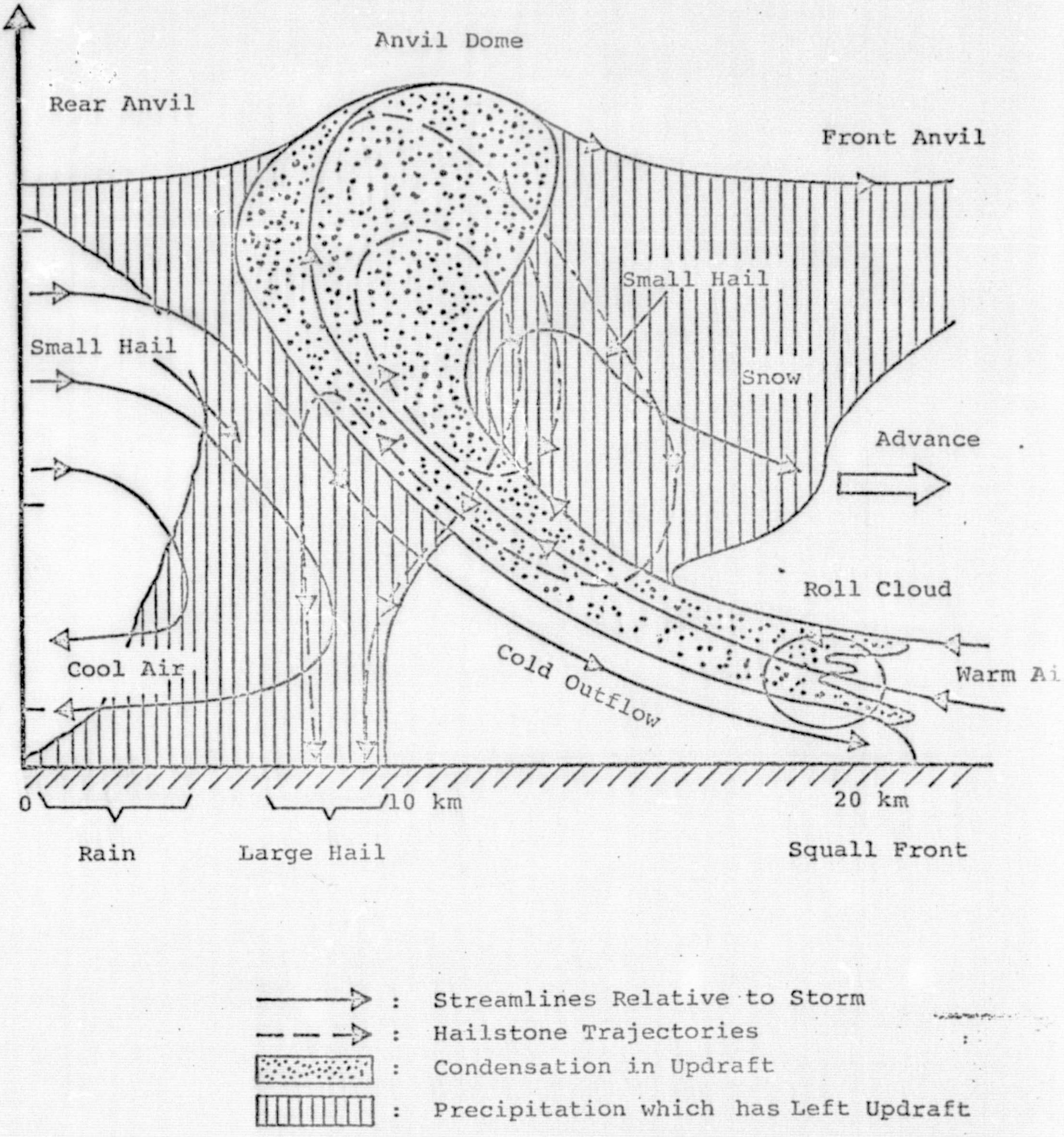

Figure 2.2. Typical Model of a Hail-Producing Thunderstorm.

2.1.2. Multi-Cell and Area Thunderstorms(2,4,6,7)

Occurrence: Tropical cyclones and reinforcement of remains of tropical cyclones; touchdowns of jet stream at troughs. Strong convective updrafts of large and unstable moist air masses at large mountain ranges can result in (orographic) area and multi-cell thunderstorms.

Typical Structure: May depend on terrain.

length: 50 - 150 km

width: 100 - 300 km

life cycle: 1 - 5 hrs

speed of approach: 15 - 60 km/hr; storm centers often stationary at mountain crests.

severe gusts: 30 - 60 m/sec and larger in major cold outflows, particularly when supported by down slopes of terrain. Also at front-base and front of clouds (roll clouds).

severe updrafts: 10 - 25 m/sec in forward cloud portions.

severe downdrafts: 15 - 50 m/sec in backward lower cloud portions and hail area; enhanced by down slopes of terrain (katabatic winds).

strongest wind shifts: At and near ground level at the front of individual cold outflows and at the rear of individual cells.

strongest winds: 25 - 50 m/sec in cold outflows.

Special Features: Usually many and strong hail areas with hail stones from 3/4" to 1" size; often tornados during and funnel clouds during and after passage of severe multi-cell and area storms. Development of thunderstorm-high enhanced and effects mentioned under 2.1.1 apply to a larger degree.

2.1.3. Supercell Thunderstorms (2,4,6,7)

Occurrence: Same as for multi-cell and area thunderstorms when all circumstances are such that several thunder cells combine to a single, giant cell.

Typical Structure: Depends on terrain and meteorological situation.

life cycle: ∿1 - 10 hr

length: ∿ 50 - 150 km

width: ∿ 25 - 50 km

speed of approach, severe gusts, and features are similar to those of multi-cell and large area thunderstorms.

Special Features: Large hail areas with hail stones larger than 1.5" and tornadoes. Durations of 6 to 12 hrs (within multicell areas or isolated giant single cell) with strong storm and hail periods from 1/4 to 3 hrs.

2.1.4. Thunderstorm (prefrontal) Squall Lines (2,4,5)

Occurrence: 80 to 500 km in advance of a cold front lifting particularly unstable warm and moist air mass or inversion. Cold outflows from developing line of thunder clouds reinforce cold air wedge far ahead of front by moving faster than upper level cloud portions. Resulting line of rising columns of warm air masses in front of thunderstorm line and propagation of thunderstorm after thunderstorm in squall line.

Typical Structure: Band of thunderstorm cells stretched perpendicular to direction of motion.

life cycle: 1 - 10 hr

length: 20 - 60 km in direction of motion

width: 250- 500 km (length of band)

speed of approach: 15 - 60 km/hr

severe gusts: 20 - 30 m/sec at front of cold air outflow under and at leading edge of cloud line (roll cloud)

Severe updrafts and downdrafts similar to or more intense than those for thunderstorm cells (2.1.1).

Strongest winds and wind shifts: similar to, or more intense than, those in and around storm cells of multi-cell thunderstorms (2.1.1 - 2.1.2), particularly in front, below, and just above the roll cloud near the lower leading edge of the squall-line clouds.

Special Features: Strong hail showers with strong down-drafts; tornadoes and funnel clouds are usual in strong line-squall thunderstorms.

2.2 Tornadoes(5-11)

In order to distinguish operationally tornadoes and often less dangerous cold air funnel clouds and cold air water spouts from usually harmless dust devils, etc., we define them as strong vortices which interconnect from clouds to the ground or which are connected to clouds without touchdown. Funnel clouds are included which form in warm air sectors in contact with cold air masses. For cold air funnel clouds, see 2.3 below.

Occurrence: Heavy multi-cell, area, and line squall thunderstorms (including supercell storms), particularly, if rotating thunderstorm cells develop. Twisting updrafts and downdrafts next to each other in thunderclouds, particularly at dry cold fronts and in regions of turbulent mixing of cold air with warm moist air at the cloud level in thunderstorm line-squalls. Require unstable temperature profile with unstable moisture profile at low altitudes.

Typical Structure (See Figure 2.3.):

path-length: 0.5 - 15 km (150 to 500 km observed on very rare occasions).

path-width: 10 - 300 m (0.5 to 10 km observed on very rare occasions with multiple touchdowns).

speed of approach: 15 - 30 km/hr (50 to 80 km/hr on rare occasions in fast-moving thunderstorms).

wind speeds: 20 - 70 m/sec (100 to 200 m/sec observed on rare occasions).

updrafts: In suction areas and suction vortices. Velocities not really known but may be estimated as 30 to 100 m/sec (debris carried aloft can reach altitudes of 8 to 10 km in and above parent cloud). Debris can be scattered as far as 10 to 20 km (50 km on rare occasions) by usually strong altitude winds of up to 200 km/hr at the top of parent clouds (8 to 10 km height).

Special Features: Usually condensation and electrical discharge in center funnel and secondary suction vortices. Often, rotating thunderstorms can lead to area damage similar to that of tornadoes and cyclones by producing several tracks

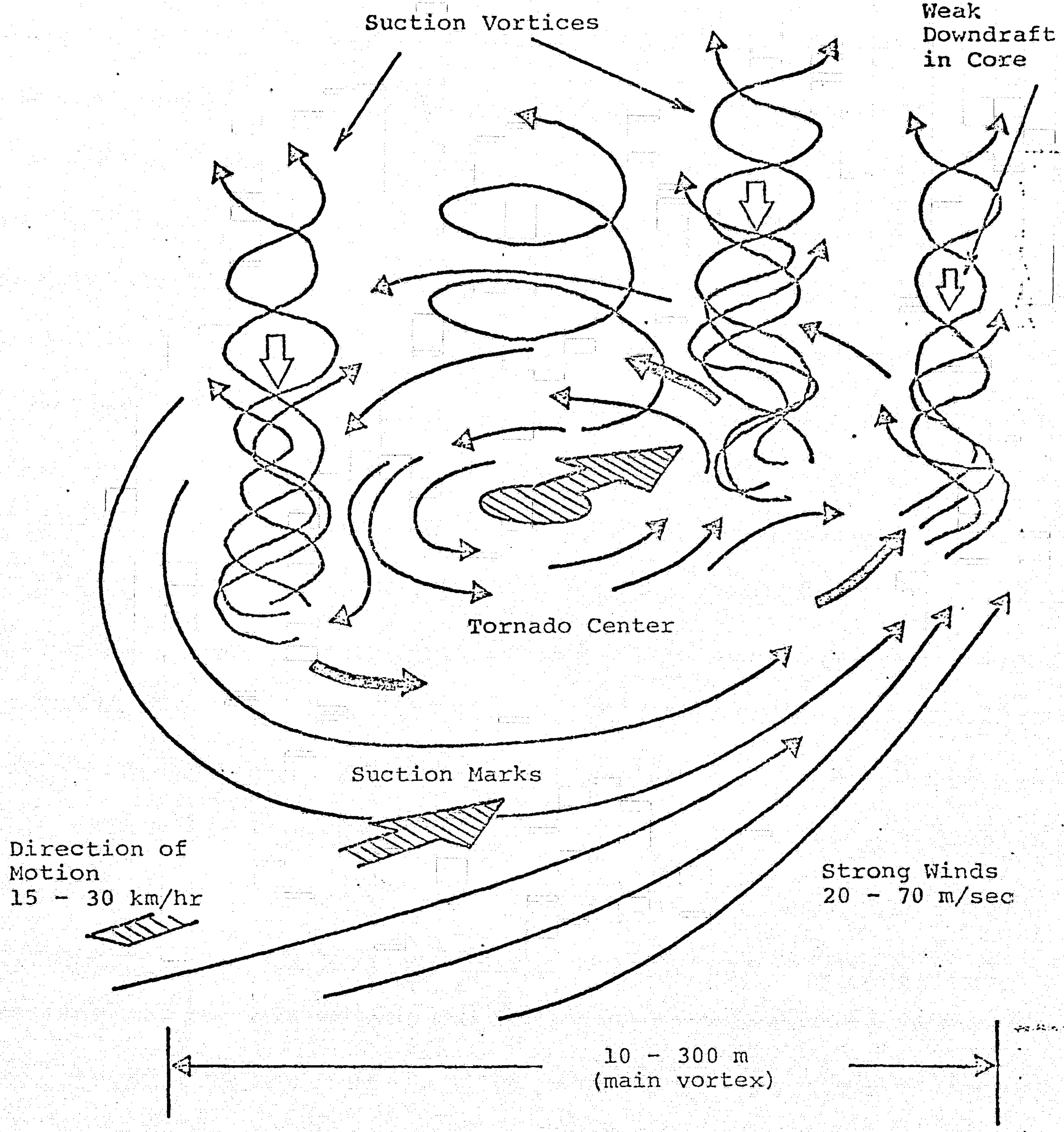

Figure 2.3. Tornado Cross-Section Near Ground.

of suction marks. Tornadoes often occur in families in intervals of about 30 to 60 min; the individual families can exist for 20 to 50 min with 3 to 8 tornadoes in a family. Over areas of water, tornadoes become tornadic water-spouts.

2.3. Funnel Clouds (Cold Air Funnel Clouds)(11)

Funnel clouds occur primarily in cold air masses (cold air funnel clouds) and warm moist air masses at line-squalls and cold fronts. The latter funnel clouds are typical precursors of tornadoes, and are therefore not included here (See 2.2 above.). Cold air funnel clouds have no tornado potential and are usually low damage-producing - if damage occurs at all. They are included here because of lack of study. (Laser velocimetry studies should be most helpful since radar signatures are usually absent).

Occurrence: Unstable moisture profiles below cold and dry air with stable temperature lapse rate. Cold air circulation of cold core low pressure centers near weak upper-level troughs. Near shore lines if on-shore wind supplies moisture below cold air masses.

Typical Structure: Usually, cold air funnel clouds descend from parent clouds and rarely touch the ground. Diameters are typically 10 to 20 m at the base of the parent cloud and taper to less than 3 m near the ground. If touchdown occurs, there is usually only very minor damage which is limited in area. Funnels do not necessarily extend vertically from the parent cloud.

path-length: 1 - 4 km (up to 10 km observed on rare occasions)

path-width: 1 - 5 m (up to 20 m observed on rare occasions)

speed of approach: 15 to 50 km/hr

wind speeds: not really known; may be estimated to 2 - 10 m/sec because of minor damage.

Special Features: The duration of cold air funnel clouds is limited from 30 sec to 10 min (up to 15 - 20 min observed on rare occasions). Over areas with water, cold air funnel clouds become cold air water spouts. Cloud associated with funnels reach altitudes from 4000 to 8000 m. The funnels extend usually only 60 to 250 m below the base of the parent cloud (funnels of more than 1 km length have been observed on rare occasions).

2.4 Dust Devils(8)

Although most dust devils are of small scale and of small intensity, some can reach considerable strengths so that they can turn over cars and cause significant structural damage.

Occurrence: Very unstable temperature lapse rates near the ground in hot and dry air (strong near-ground inversion).

Typical Structure: Hot-air, thermal vortices rotating clockwise or counter-clockwise with strong upward convection; dust devils originate from the ground upwards.

path length: 0 - 5 km (up to 10 km on rare occasions)

path width: 10 - 100 m (up to 500 m on rare occasions)

height: 30 - 200 m (very strong ones up to 1000 m with invisible disturbances up to 200 m).

speed of approach: 0 - 20 km/hr (most dust devils move with environmental wind if it is $\gtrsim$ 5 km/hr); stationary at hill ridges.

wind speeds: Not really known; may be estimated to 5 - 30 m/sec in view of possible damage (up to 50 - 100 m/sec on very rare occasions).

updrafts: Not really known; may be estimated at 10 - 50 m/sec (up to 100 m/sec on rare occasions) in view of possible damages.

Special Features: Most dust devils have life spans of 2 to 5 minutes; however, some may last for 30 min or more (up to 4 hrs on rare occasions). Dust devils do not show electrical discharges inside or at the base of the vortices. Usually, if discharge is observed, the phenomena is called a tornado. Often smaller updraft vortices seem to appear within the main vortex of dust devils.

2.5. Vortices Generated by Density Currents(8,18)

Strong vortices, like tornadoes, are often associated with gravity or density flows in the atmosphere which are generated by severe temperature differences. Usually, the necessary flows result from the cold outflows of large area thunderstorms and line squalls and from cold air (katabatic winds, chinooks, Santa Anas, boras), particularly when supported by steep down slopes in the terrain. Similar types of strong vortices are produced by density flows, for example, in airborne avalanches of powder-snow, avalanches of liquid and solid volcanic materials that evolve gases continuously (nuée ardente), and large sand and dust desert storms (haboob). Since these phenomena produce high velocity, vortex-like circulations similar to those observed in severe thunderstorms, they are briefly outlined here and their common features are described below.

2.5.1. Airborne Powder-Snow Avalanches (8,13)

Dense suspension of air surrounded snow particles moves like a heavy gas with very little internal friction. Surrounding warmer air and irregularities of terrain cause friction along outer surfaces. The result is considerable turbulence and increase in the speed of the central core of the cold, high-density flow, with spin-off of both, vertical and horizontal vortices.

bulk-flow velocity: 30 - 100 m/sec
vortex-flow velocity: 2 x bulk velocity (up to 200 m/sec)
vortex-flow duration: 2 - 3 sec for each cell
vortex cell size: 0.5 - 30 m (estimate)

2.5.2 Nuée ardente* (7,11)

Avalanche of heavy volcanic material ejected as a viscous, auto-explosive liquid that continuously evolves

---

* "Nuée ardente" from French: nuée - "storm", and ardent - "fiery, red," "burning"; thus "firey storms" (not to be confused with "fire storms": strong surface storms generated by the suction of large area fires).

gases. Emitted gases practically eliminate contact friction of the particles and cause avalanche to spread almost as freely as a true liquid. Irregularities in density and terrain result in considerable turbulence and spin-off of horizontal vortices.

bulk-flow velocity: 3 - 10 m/sec

vortex-flow velocity: 70 - 100 m/sec

vortex-flow duration: not really known (~ 1 - 20 sec, estimate)

vortex cell size: not really known (0.5 - 30 m, estimate)

front of avalanche cloud: many short (~ 0.5 - 30 m ?) horizontally-rotating vortex cylinders with axes of no two cylinders parallel.

2.5.3. Sand and Dust Storms (haboob)*[8]

Huge sand and dust storms are usually generated by cold air outflows of decaying thunderstorms during desert seasons of high convective instability, or by cold air, katabatic winds (chinooks, Santa Anas, or boras) resulting from large high pressure areas in northern or southern cold regions of the globe. They may stretch over widths of more than 150 km and can rise to the level of the cloud base (condensation base). A in the case of nueés ardentes and airborne powder snow avalanches, a dense suspension of air-surrounded sand and dust particles evolves which moves like a heavy gas with very little internal

---

* "Haboob" from Arabic: hebbe - "blown".

friction. Surrounding various air masses and air pockets as well as irregularities in the terrain cause friction areas with resulting build-up of intense vortices, particularly at the turbulent fronts of these systems. Often, "eddy tornadoes" form in the lee of local minor mountain systems.

bulk flow velocity: 5 - 20 m/sec (or larger, depending on the velocity of the cold air outflow).

vortex-flow velocity: 20-100 m/sec (or larger on rare occasions).

vortex-flow duration: not really known (~ 5 to 60 min. for tornado-like structures estimated).

vortex cell size: ~ 10 - 300 m (or larger on rare occasions for tornado-like structures).

2.5.4 Typical Vortex Structures in Density Currents(8)

Atmospheric vortices caused by density currents resulting from temperature differences are similar to those observed in true liquid systems at the interfaces of gravity flows. In the following, three structures are briefly described which are typical for such flows. They are intended to provide with a general and qualitative idea about how and where intense vortices can be formed in the atmosphere.

2.5.4.1. Surge Heads(8,14,15)

Heavy cold air flow into warmer air masses can produce surge heads which develop characteristic protruding

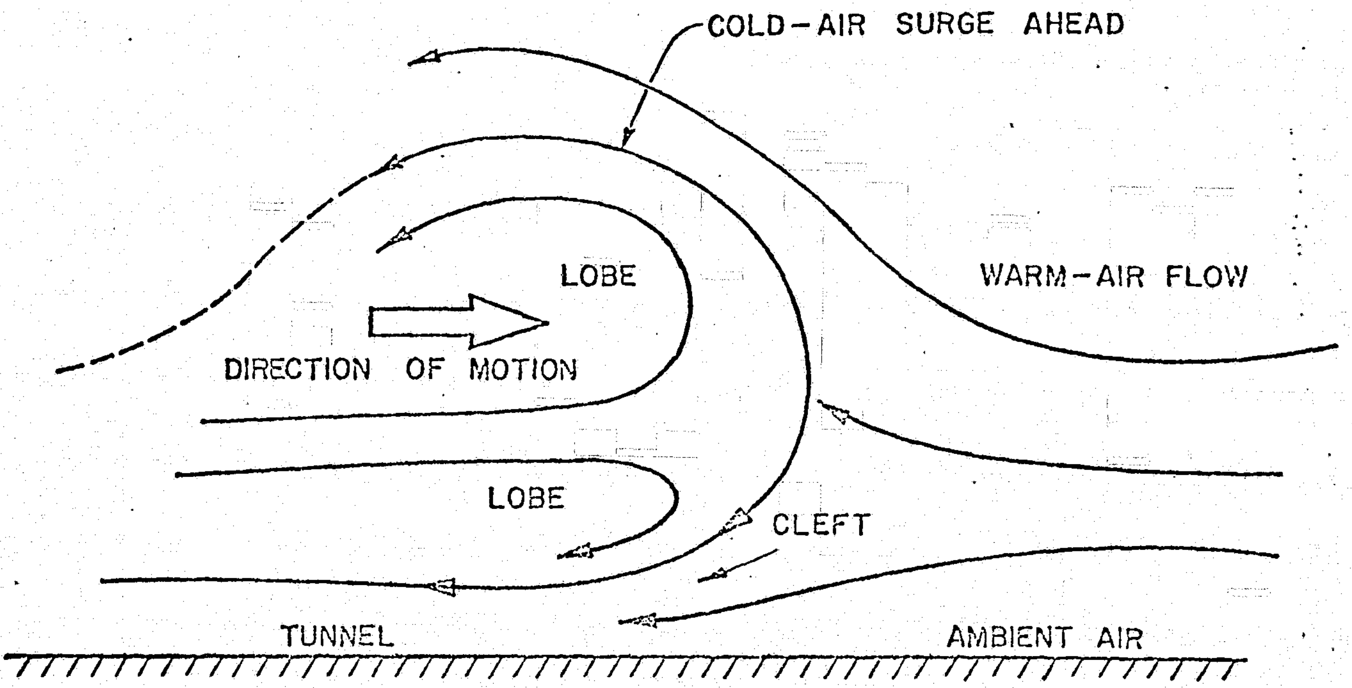

Figure 2.4a. Side View of Cold Air Surge Head Moving from Left to Right.

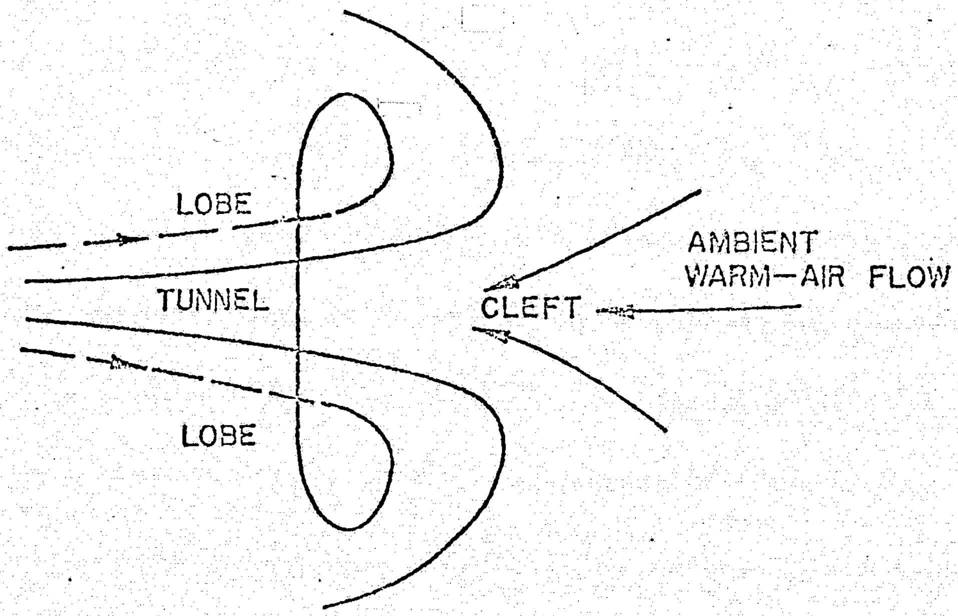

Figure 2.4b. Top View of Cold Air Surge Head Moving from Left to Right.

lobes separated by incisive undercutting clefts and warm air tunnels (see Figs. 2.4a and 2.4b) along the ground surface. Eddies with vertical axes often form within the clefts. The surge head may become a system of oppositely rotating longitudinal vortices which are practically identical to the internal structure of the nuée ardente. Similar atmospheric vortices can also be caused by sea breeze fronts, by dust walls in dust storms, and by the leading edges of steep cold fronts. The resulting phenomena may be strong dust devils, funnel clouds, and tornado-like structures, either occurring isolated or in rows along the front of the cold air masses. Tornado-like vortices can develop in the presence of as little as one percent density difference between the cold and warm air masses, corresponding to temperature differences of only 3°C. Temperature differences of more than 13°C (corresponding to density change of $\gtrsim$ 4%) have been observed at the front of large haboobs fed by cold air outflows from large thunderstorms.

2.5.4.2. Rising Tunnels(8,16-18)

Vertical vortices in density currents can occur when the warm air entrained in the tunnels of surge head rises (see Fig. 2.5). This rise can be caused by eddies in the wake of an obstruction in the path of the cold air outflow and can result in giant dust-devil type vortices. If the volume of engulfed warm air is large enough, the vortex

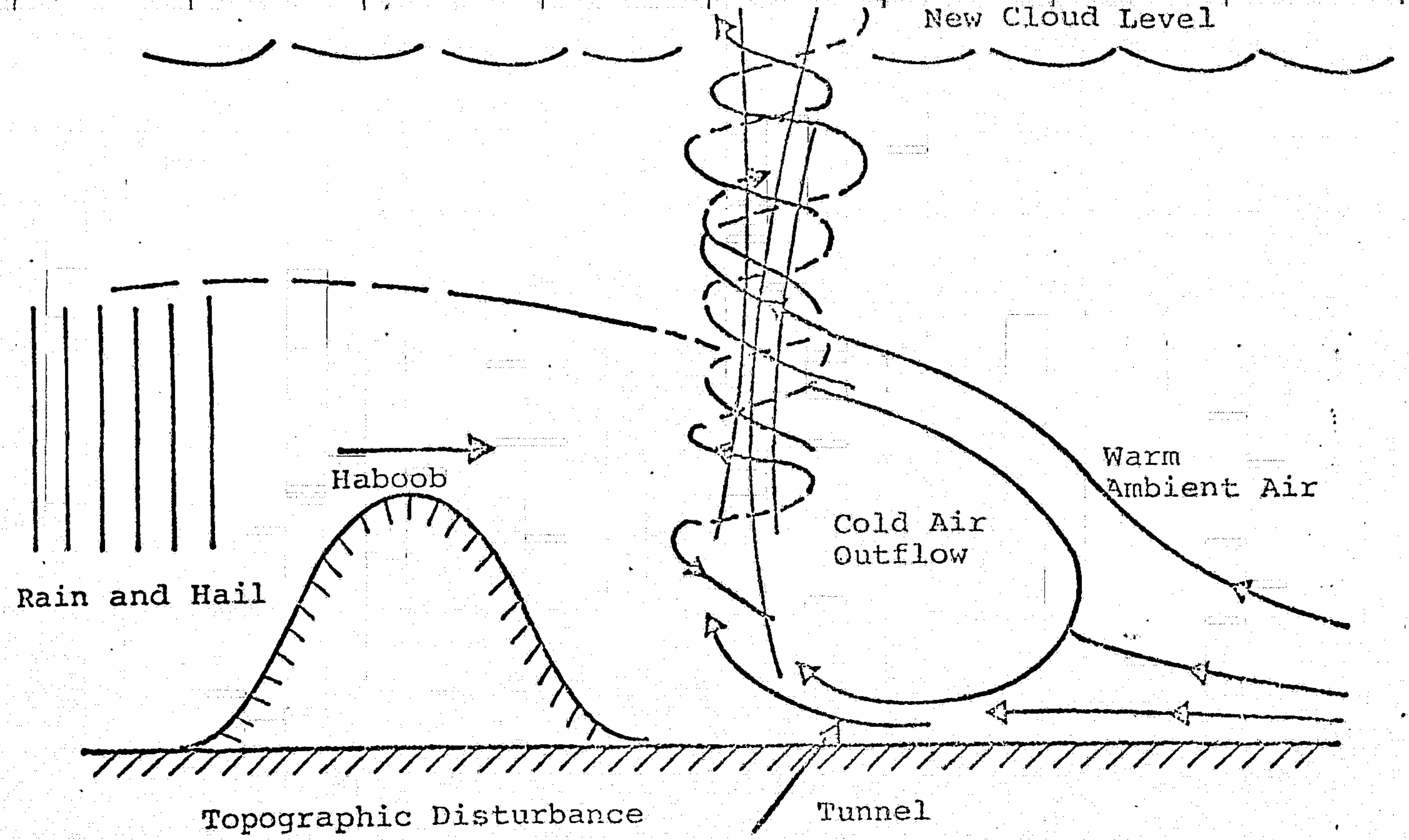

Figure 2.5. Flow (from left to right) of a Surge Head Over a Topographic Obstruction. (Eddies in the wake of the obstruction can cause warm air tunnels to rise like a giant dust devil.)

ORIGINAL PAGE IS
OF POOR QUALITY

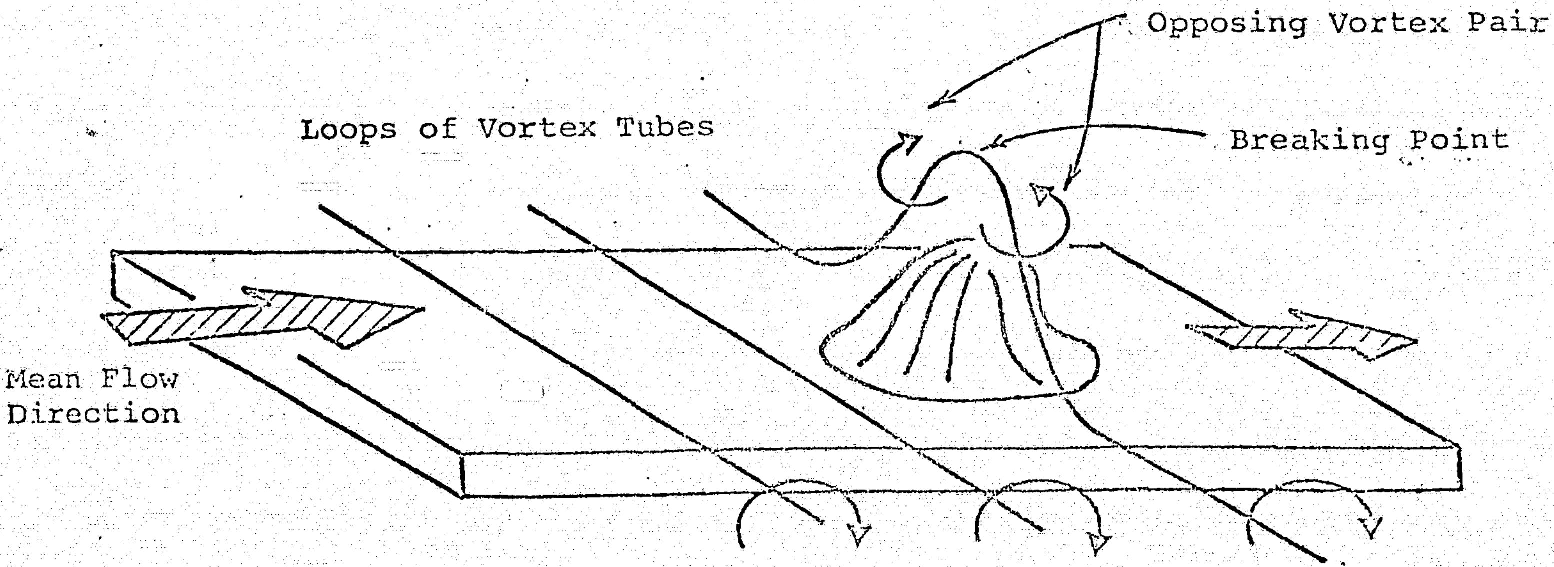

Figure 2.6. Vortex Pair Formed in a Density Current by Interaction with a Topographic Disturbance. (Vortex tubes may originate in the upper or lower circulation of the surge head shown in Figure 2.4a.)

can penetrate the top of the surge head. Then warm air pushed up by the leading edge of the cold air outflow may be added to the vortex so that it can reach the condensation base. Here, the vortex can gain further energy by condensation of moisture to new cloud elements. At this stage, the vortex has acquired the characteristics of a full-fledged tornado. Although it can occur everywhere, this mechanism is probably more likely to operate in the presence of topographic disturbances. Tunnels may rise by buoyancy. The turbulence inherent in the surge head can impart easily a circulation pattern to the acending convection current and, once stretched, the vortices can intensify considerably.

2.5.4.3. Vortex Pairs (8,19)

Vertically rising vortex pairs can be formed when horizontal vortex tubes are lifted out of the local boundary layer by a topographic disturbance (see Fig. 2.6). The horizontal vortex tubes may originate either in the upper or in the lower lobe-circulation of the surge head associated with a cold air outflow as shown in Fig. 2.4a.

2.5.4.4. Vortices from Clouds (7,9)

Vertical vortices reaching down from clouds can be formed by similar mechanisms as those described above if strong rotating downdrafts (vertical downward surge heads?)

engulf warm updrafts with the same axis and sense of rotation$^{(9)}$ (see Fig. 2.7). This situation may appear in rotating thunderstorms and when strong vertical cold-air outflows from huge thunderstorms and line-squall thunderstorms are accelerated by hail, snow and rain. Usually, tornadoes are the result at the base of these regions where cold downdrafts and warm updrafts mix in a swirling motion.

NOTE: Valuable criteria have been quoted in ref. 20 for given buoyant forces with access to large scale vorticities to develop into concentrated vorticities; namely, for

$U_\infty/U_B < 0.15$: buoyancy dominant - no significant vortex generation,

$U_\infty/U_b > 0.9$: no concentration of vorticity by vertical motions - whole flow swirls,

$0.15 < U_\infty/U_B$ 0.9: possible generation of concentrated vorticity.

Here, U_∞ = tangential component of horizontal velocity of environmental air and U_B = characteristic vertical speed of buoyant air mass.

Considerable more observations are required of the vortices associated with frontal boundaries of density flows if a reasonably confident understanding of their true nature and dynamics is to be achieved. Typical questions are: Do they occur in front of or behind the surge heads? Is their

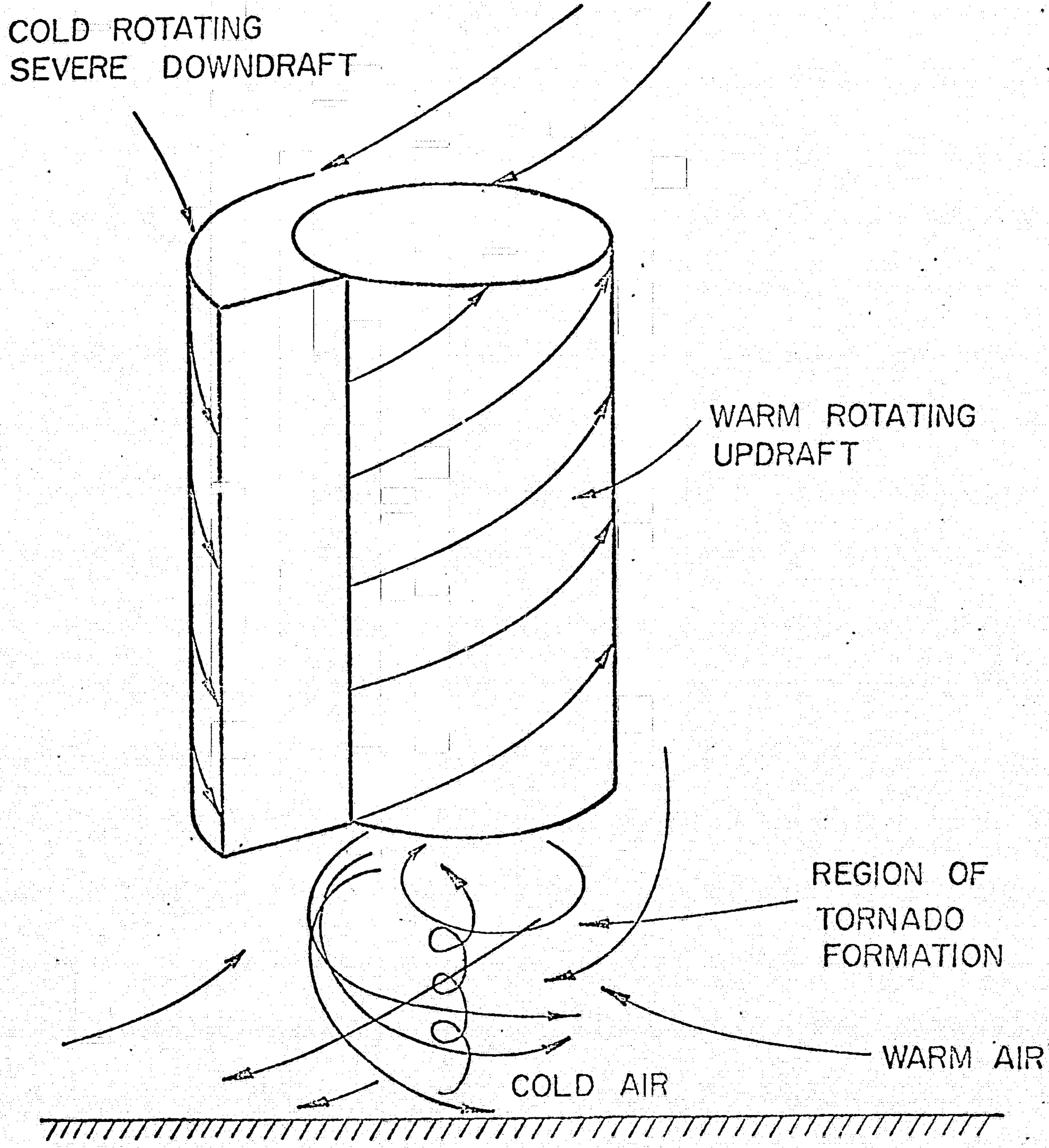

Figure 2.7. Possible Mechanism for Tornado Formation by Co-Axially Rotating Warm Updrafts and Cold Downdrafts.

rotation cyclonic or anticyclonic? Do they have dynamic connections with the cloud base and/or the air near the ground? Are they favored downwind of significant topographic disturbances? Are twin-funnels very common? Are smaller subsidiary vortices often associated with large dust devils?

3. TYPICAL STRONG WIND SHIFTS AND GUSTS ALOFT AND NEAR THE GROUND

Large local changes in the direction and the speed of winds aloft and near the ground occur primarily by two mechanisms: (a) high velocity, veered (turned clockwise) winds brought down by prevailing vortex loops or vortices in the lee of topographic disturbances and (b) vortices and turbulence generated by wind shears and by topographic obstructions in the main stream of strong gradient, warm katabatic, jet stream, and hurricane winds. All other disturbances associated with the mixing phenomena occurring between warm and cold air masses and pockets fall under disturbances in density flows (see above). Gusts are related to turbulence in air flows, and we consider here moderate to extreme turbulence which is usually associated with wind speeds of 10 m/sec (20 kts) and larger.

Typical gust factors are shown in Table 2 as functions of wind speed and average time periods used for obtaining data. From Table 2, it is apparent that, for average time periods between 1/2 and 30 sec, the typical gust velocities are given by

$$U_{gust} \simeq (1.44 \pm 0.11)\, U_{wind}.$$

These values apply for the horizontal wind component in gusts.

Mean Wind Speed m/sec	Time Period; sec				
	1/2	5	10	20	30
10	--	1.50	1.40	1.35	1.30
15	--	1.47	1.43	1.37	1.33
20	1.63	1.48	1.42	1.35	1.32
25	1.64	│	│	1.36	│
30	1.60	│	│	1.35	1.31
35	1.59	1.49	│	│	│
40	--	1.48	1.43	1.36	1.33
Average	1.61	1.48	1.42	1.36	1.32

TABLE 2. Gust Factors Averaged Over Short Time Periods(21)

The vertical velocity component follows the same relation for altitudes $\gtrsim$ 30 m. Decreases of the gust factor with increasing altitude are not considered since they apply only for ground friction eddies in stable air streams. High speed horizontal gusts have typical durations of 1/2 to 30 sec; the corresponding vertical durations are ~ 1/3-times the horizontal periods. Typical distances over which the average wind speeds increase to peak gust velocities are between 15 and 70 m and correspond to wind shears between 1/10 and 3 $\sec^{-1}$. Table 2 can be used to estimate typical peak velocities in gusts for given wind speeds. Thus, for Santa Ana winds of 30 - 35 m/sec, down-draft gusts in valleys of up to 40 m/sec are possible and have been observed.(4) Typical directional changes of winds in gusts are 15° to 30° near the ground(2). But changes of more than 160° have been observed under roll clouds caused by the rotor flow in the wake of dense-barrier flow(2).

3.1. Typical Wave Streaming and Rotor Streaming(2)

Wave streaming and rotor streaming are vortex-shedding phenomena and occur usually in the lee of large topographic disturbances (see Figs. 2.1a and 3.1b). In the case of rotor streaming, counter-flow develops at the lee side of the obstruction near the ground, and the flow is more turbulent than that below the rotor

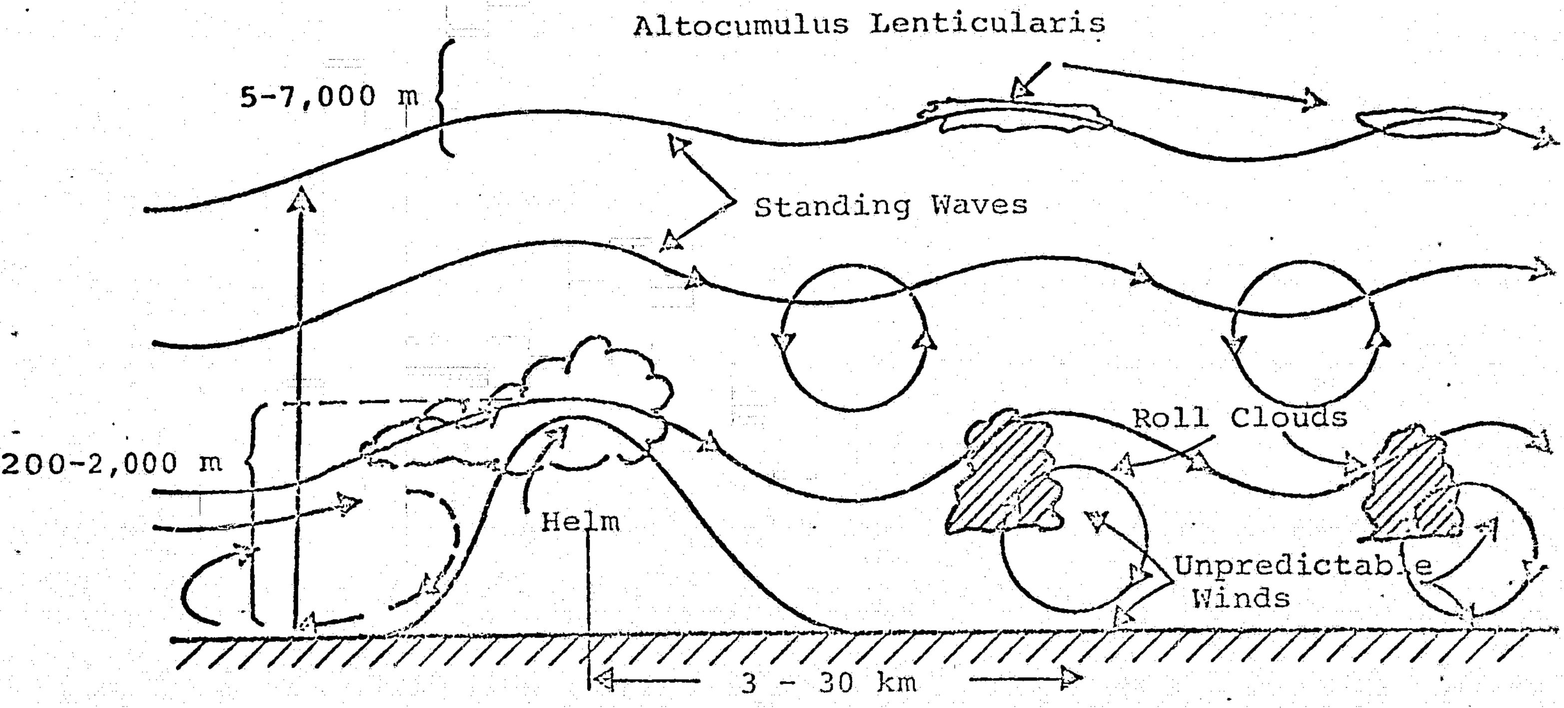

Figure 3.1a. Typical Wave Streaming in the Lee of a Large Topographic Disturbance.

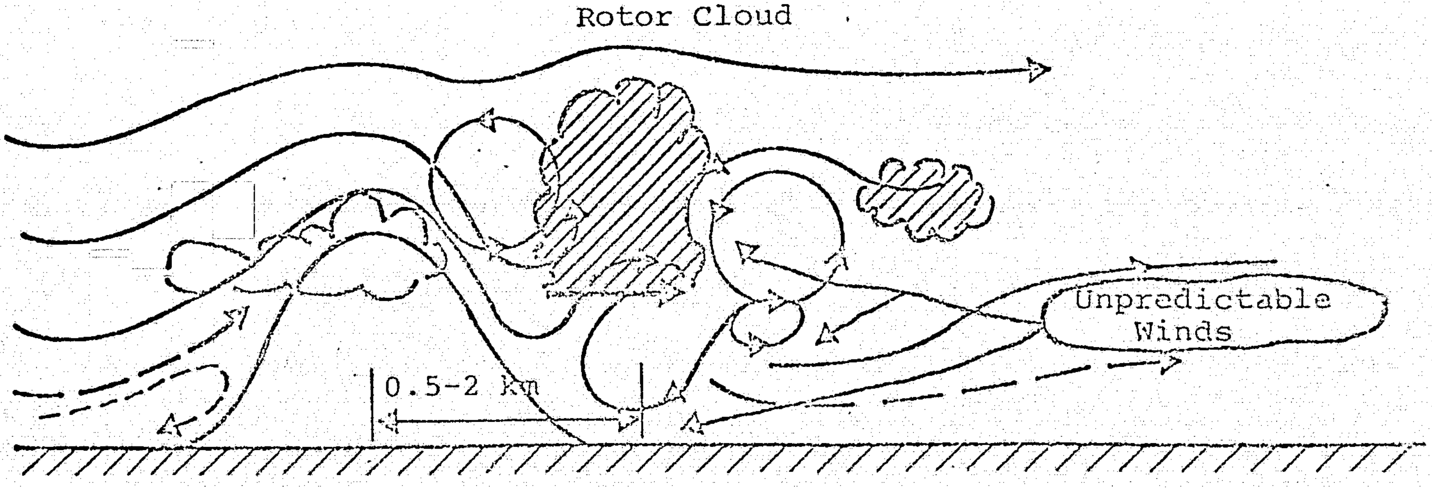

Figure 3.1b. Typical Rotor Streaming in the Lee of a Large Topographical Disturbance (vortex shedding).

clouds in wavestreaming.

wind shifts: from 25° to 160°, particularly under rotor clouds.

velocities in gusts: depend on the average wind velocities (See Table 2.). Note: momentary calms can occur below rotor clouds and roll clouds, as well as in the near lee of mountains with subsequent wind shifts of 90° to 135° to the direction of the previous gust.

Typical Features: Severe downdrafts can occur momentarily and periodically below and near the front of roll-clouds with velocities on the order of (and up to 2-times) that at the mountain ridge. Directional shifts near and at the ground are usually large in the near lee of the obstruction and under the rotor and roll clouds. Wind shifts of 90° to 135° have been observed at the ground between observation stations which were 800 m apart; for example, at an airport in the lee of a mountain range.(2)

3.2. Turbulence in the Lee of Mountains

Moderate Turbulence: Found for winds of 12 to 25 m/sec at the ridge of mountains at distances of up to 250 to 500 km leeward, from the ground up to the tropopause and as much as 3000 m above the tropopause.

Severe Turbulence: Found for winds of $\gtrsim$ 25 m/sec at the ridge of mountains at distances of up to 80 to 250 km leeward and from the ground up to the tropopause.

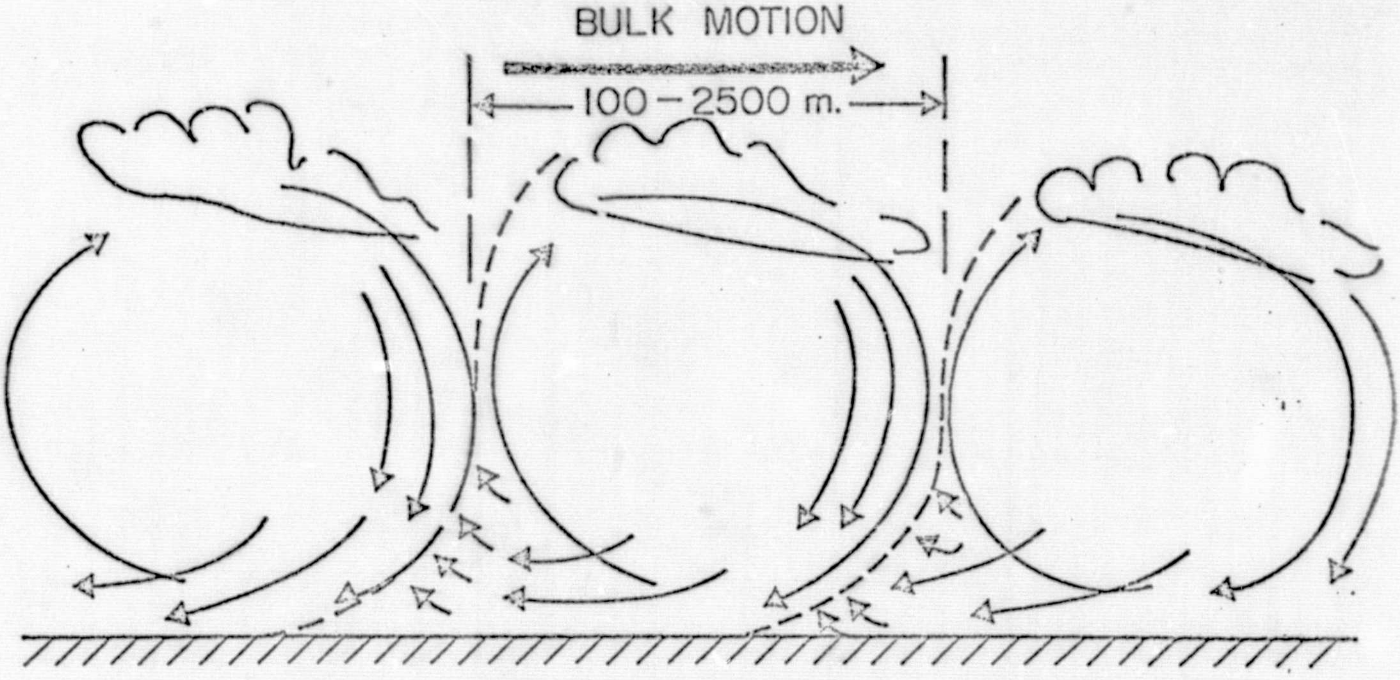

Figure 3.2a. Typical Circulation in Medium Gust Cells as reviewed in a coordinate system moving with the circulation cells

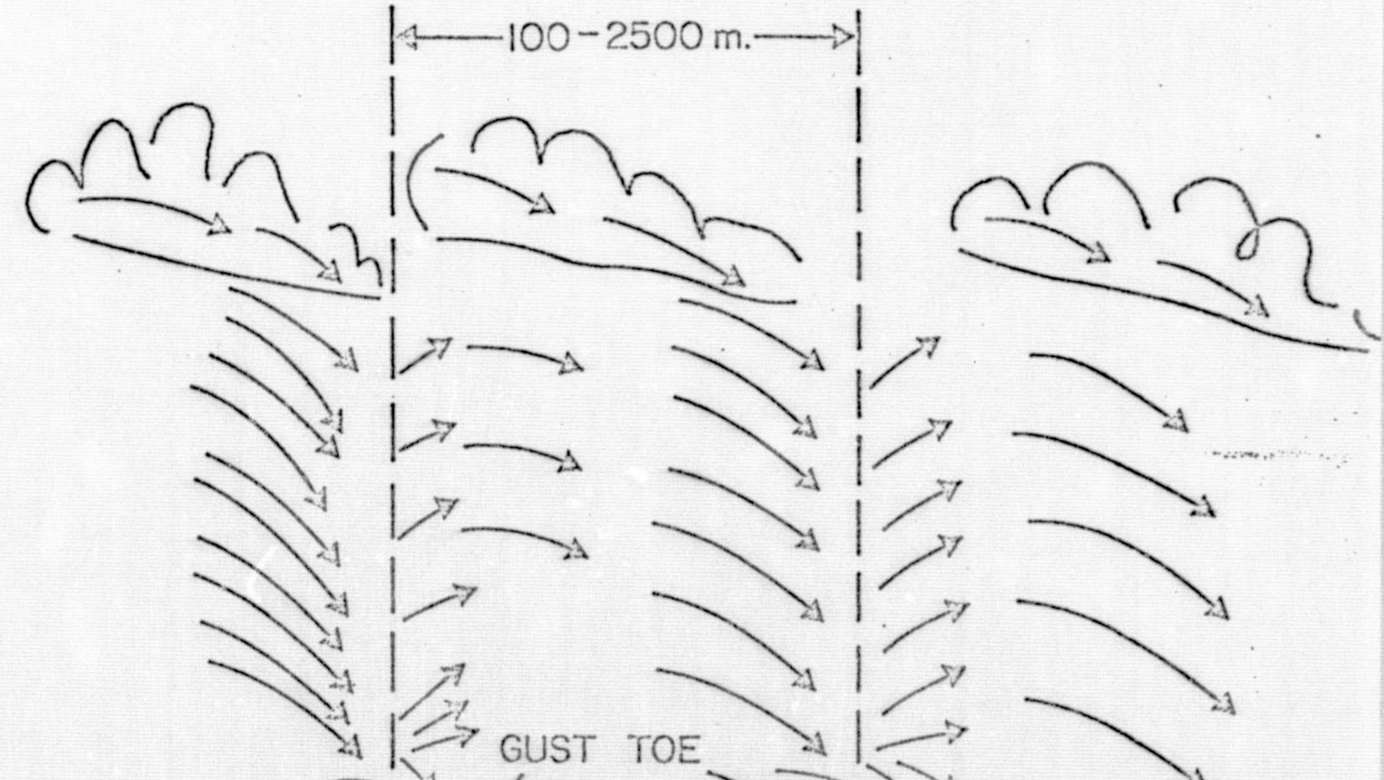

Figure 3.2b. Typical Section through Medium Gust Cells (horizontal motions near Cell Boundaries).

Extreme Turbulence: Found for winds of ≥ 25 m/sec at the ridge of mountains at low levels in the lee and in and near rotor clouds. Sometimes severe turbulence is found within a layer between the height of the jet-stream core, 2000 m below the core and about 80 to 250 km towards the cyclonic (cold) side of the jet core.

3.3. Circulation Gust Cells(2)

Circulation gust cells are caused by frictional flow near and at the ground. Usually, higher speed wind is brought to the surface more or less periodically from aloft (see Figs. 3.2a and 3.2b). Usually high-speed gusts are brought down behind the leading edge of the gust fronts.

wind shifts:	In the northern hemisphere, clockwise (veered) with increasing speeds, counter-clockwise (backed) with decreasing wind speeds; typically 15° to 30°, but up to 45° observed on some occasions.
wind speeds:	See Table 2 for gust velocities as a function of wind velocity.
average size:	100 - 2000 m for small to medium size eddies of strong gusts.

Special Features: For medium size gust cells, the whole wind field is rather variable in both speed and direction. If the upward convection in gust cells extends to large altitudes, major gusts with twice the average wind speed can occur near and at the ground in large eddies over

~ 30 min average recurrence intervals. The typical life times of gust cells are not well known, but may be from 5 to 50 sec. The turbulence usually associated with gusts can extend to altitudes of 1000 - 2000 m.

REFERENCES

1. S. Kurtz, Meteorologist (ret.), NWS-San Diego, private communication.

2. Watts, Wind and Sailing Boats, Quadrangle Books, Yacht Racing Magazine, Chicago (1970).

3. P. Davies-Jones and J. H. Henderson, "Characteristics of Thunderstorm Updraft Soundings," Eighth Conference on Severe Local Storms, Denver, Colo., American Meteor. Soc., p. 1-5 (1973).

4. H. Walker, Wind and Strategy, W. W. Norton & Co., Inc., New York (1973).

5. G. Guerny and J. A. Skiera, Pilot's Handbook of Weather, Aero Publishers, Inc., Fallbrook, Ca. (1964).

6. Several articles in Eighth Conference on Severe Local Storms, Denver, Colo., Amer. Meteor. Soc. (1973).

7. R. G. Barry and R. J. Chorley, Atmosphere, Weather and Climate, Hall, Rinehart and Winston, Inc., New York (1970).

8. S. B. Idso, "Tornado or Dust Devil: The Enigma of Desert Whirlwinds," American Scientist 62, 530-541 (1974).

9. T. T. Fujita, "Proposed Mechanism of Tornado Formation in Rotating Thunderstorms," Eighth Conference on Severe Local Storms, Denver, Colo., Amer. Meteor. Soc., p. 191-196 (1973).

10. T. T. Fujita and A. D. Pearson, "Results of FPP Classification of 1971 and 1972 Tornadoes," Eighth Conference on Severe Local Storms, Denver, Colo., American Meteor. Soc., p. 142-145.

11. J. R. Cooley and M. E. Soderberg, "Cold Air Funnel Clouds," Eighth Conference on Severe Local Storms, Denver, Colo., American Meteor. Soc., p. 173-179.

12. F. H. Finch, "On the Mechanics of Nuées Ardantes," J. Geol. 43, 545-550 (1935).

13. C. Fraser, The Avalanche Enigma, pp. 301, Murray Publ., London (1966).

14. J. E. Simpson, "A Comparison between Laboratory and Atmospheric Density Currents," Quart. J. Roy Meteorol. Soc. 95, 758-765 (1969).

15. J. E. Simpson, "Effects of the Lower Boundary on the Head of a Gravity Current," J. Fluid. Mech. 53, 759-768 (1972).

16. J.R.L. Allen, "Mixing of Turbidity Current Heads and Its Geological Implications," J. Sed. Petrology 41, 97-113 (1971).

17. T. J. Lawson, "Haboob Structure at Khartoum," Weather 26, 105-112 (1971).

18. T. Maxworthy, "A Vorticity Source for Large-Scale Dust Devils and Other Comments on Naturally Occurring Columnar Vortices," J. Atmos. Sci. 30, 1717-1722 (1973).

19. B. R. Morton, "Geophysical Vortices," Prog. in Aero Sci. 7, 145-194 (1966); The Physics of Fire Whirls," Fluid Dynamics Lab. Paper 19, Monash Univ., Clayton, Vict., Canada, pp. 34, August 1969.

20. S. R. Hanna and F. A. Gifford, "Meteorological Effects of Energy Dissipation at Large Power Parks," Bull. Amer. Meteor. Soc. 56, 1069-1076 (1975).

21. C. L. Bretschneider, "Overwater Wind and Wind Forces," Handbook of Ocean and Underwater Engineering, eds. J. J. Myers, C. H. Holm and R. F. McAllister, pp 12-1 ÷ 12-14, McGraw-Hill Book Comp., New York (1969).

20. Abstract

scanned for velocity (and possibly turbulence), and is intended for diagnostics of the lower altitude region below the storm and in the out-flow region.

The essential conclusion of the study is that aircraft flight velocities are high enough and severe storm lifetimes are long enough that it is possible for a single airborne Doppler system, operating at a range of less than about 20 km, to view the storm area from two or more substantially different aspects before the storm characteristics change appreciably. This permits resolution of the spatial distribution of the velocity vector by a single coaxial system operating in a fly-by mode.

In addition, it is concluded that when either or both peak power rather than mean power and/or peak data handling rate rather than mean rate are limiting factors, the optimum signal-to-noise as well as optimum velocity resolution are to be obtained by using pulse lengths comparable to the overall dimensions of the viewed region and, as well, by operating in a continuous azimuthal scan mode. Range resolution is to be recovered in this mode by post-flight image reconstruction analysis.

Unclassified

SECURITY CLASSIFICATION OF THIS PAGE (When Data Entered)

REPORT DOCUMENTATION PAGE

READ INSTRUCTIONS BEFORE COMPLETING FORM

1. REPORT NUMBER

2. GOVT ACCESSION NO.

3. RECIPIENT'S CATALOG NUMBER

4. TITLE (and Subtitle)
Conceptual Design of An Airborne Laser Doppler Velocimeter System for Studying Wind Fields Associated with Severe Local Storms

5. TYPE OF REPORT & PERIOD COVERED
Technical

6. PERFORMING ORG. REPORT NUMBER
PD-B-76-118

7. AUTHOR(s)
J. Alex Thomson, Alan R. Davies
and Klaus G. P. Sulzmann

8. CONTRACT OR GRANT NUMBER(s)
NAS8-31724

9. PERFORMING ORGANIZATION NAME AND ADDRESS
Physical Dynamics, Inc.
P. O. Box 1069
Berkeley, CA 94701

10. PROGRAM ELEMENT, PROJECT, TASK AREA & WORK UNIT NUMBERS

11. CONTROLLING OFFICE NAME AND ADDRESS
Natl. Aeronautics and Space Administration, Marshall Space Flight Center,
Ala. 38512

12. REPORT DATE
May 1976

13. NUMBER OF PAGES

14. MONITORING AGENCY NAME & ADDRESS (if different from Controlling Office)

15. SECURITY CLASS. (of this report)
Unclassified

15a. DECLASSIFICATION/DOWNGRADING SCHEDULE

16. DISTRIBUTION STATEMENT (of this Report)

17. DISTRIBUTION STATEMENT (of the abstract entered in Block 20, if different from Report)

18. SUPPLEMENTARY NOTES

19. KEY WORDS (Continue on reverse side if necessary and identify by block number)
laser Doppler Velocimeter, Severe Storms, Wind Measurement

20. ABSTRACT (Continue on reverse side if necessary and identify by block number)

The concept of using an airborne laser Doppler velocimeter is evaluated for diagnostics of the wind field associated with an isolated severe thunderstorm.

Two scanning configurations have been identified, one a long-range (out to 10-20 km) roughly horizontal plane mode intended to allow probing of the velocity field around the storm at the higher altitudes (4-10 km). The other is a shorter range (out to 1-3 km) mode in which a vertical or horizontal plane is

DD FORM 1 JAN 73 1473 EDITION OF 1 NOV 65 IS OBSOLETE

Unclassified